The Transition Metal Dichalcogenides

Discussion and Interpretation of the Observed Optical, Electrical and Structural Properties

By J. A. Wilson and A. D. Yoffe
Cavendish Laboratory, Cambridge

Abstract

The transition metal dichalcogenides are about 60 in number. Two-thirds of these assume layer structures. Crystals of such materials can be cleaved down to less than 1000 Å and are then transparent in the region of direct band-to-band transitions. The transmission spectra of the family have been correlated group by group with the wide range of electrical and structural data available to yield useful working band models that are in accord with a molecular orbital approach. Several special topics have arisen ; these include exciton screening, d-band formation, and the metal/insulator transition ; also magnetism and superconductivity in such compounds. High pressure work seems to offer the possibility for testing the recent theory of excitonic insulators.

CONTENTS

§ 1. Introduction

The work has centred on the layered transition metal dichalcogenides of groups IV, V, VI and VII, but the non-layered compounds of group VIII are incorporated into this discussion for purposes of comparison and contrast (see table 1).

Periodic Table

IA	IIA	IIIB	IVB	VB	VIB	VIIB	VIII^a_B	VIII^b_B	VIII^c_B	IB	IIB	IIIA	IVA	VA	VIA	VIIA	O
Li^3	Be^4											B^5	C^6	N^7	O^8	F^9	Ne^{10}
$2s$	$2s^2$											$2s^22p$	$2s^22p^2$	$2s^22p^3$	$2s^22p^4$	$2s^22p^5$	$2s^22p^6$
Na^{11}	Mg^{12}											Al^{13}	Si^{14}	P^{15}	S^{16}	Cl^{17}	Ar^{18}
$3s$	$3s^2$											$3s^23p$	$3s^23p^2$	$3s^23p^3$	$3s^23p^4$	$3s^23p^5$	$3s^23p^6$
K^{19}	Ca^{20}	Sc^{21}	Ti^{22}	V^{23}	Cr^{24}	Mn^{25}	Fe^{26}	Co^{27}	Ni^{28}	Cu^{29}	Zn^{30}	Ga^{31}	Ge^{32}	As^{33}	Se^{34}	Br^{35}	Kr^{36}
$4s$	$4s^2$	$3d$ $4s^2$	$3d^2$ $4s^2$	$3d^3$ $4s^2$	$3d^5$ $4s$	$3d^5$ $4s^2$	$3d^6$ $4s^2$	$3d^7$ $4s^2$	$3d^8$ $4s^2$	$3d^{10}$ $4s$	$3d^{10}$ $4s^2$	$4s^24p$	$4s^24p^2$	$4s^24p^3$	$4s^24p^4$	$4s^24p^5$	$4s^24p^6$
Rb^{37}	Sr^{38}	Y^{39}	Zr^{40}	Nb^{41}	Mo^{42}	Tc^{43}	Ru^{44}	Rh^{45}	Pd^{46}	Ag^{47}	Cd^{48}	In^{49}	Sn^{50}	Sb^{51}	Te^{52}	I^{53}	Xe^{54}
$5s$	$5s^2$	$4d$ $5s^2$	$4d^2$ $5s^2$	$4d^4$ $5s$	$4d^5$ $5s$	$4d^6$ $5s$	$4d^7$ $5s$	$4d^8$ $5s$	$4d^{10}$ –	$4d^{10}$ $5s$	$4d^{10}$ $5s^2$	$5s^25p$	$5s^25p^2$	$5s^25p^3$	$5s^25p^4$	$5s^25p^5$	$5s^25p^6$
Cs^{55}	Ba^{56}	La^{57}	Hf^{72} $4f^{14}$	Ta^{73}	W^{74}	Re^{75}	Os^{76}	Ir^{77}	Pt^{78}	Au^{79}	Hg^{80}	Tl^{81}	Pb^{82}	Bi^{83}	Po^{84}	At^{85}	Rn^{86}
$6s$	$6s^2$	$5d$ $6s^2$	$5d^2$ $6s^2$	$5d^3$ $6s^2$	$5d^4$ $6s^2$	$5d^5$ $6s^2$	$5d^6$ $6s^2$	$5d^9$ –	$5d^9$ $6s$	$5d^{10}$ $6s$	$5d^{10}$ $6s^2$	$6s^26p$	$6s^26p^2$	$6s^26p^3$	$6s^26p^4$	$6s^26p^5$	$6s^26p^6$
Fr^{87}	Ra^{88}	Ac^{89}															
$7s$	$7s^2$	$6d$ $7s^2$															

Ce^{58}	Pr^{59}	Nd^{60}	Pm^{61}	Sm^{62}	Eu^{63}	Gd^{64}	Tb^{65}	Dy^{66}	Ho^{67}	Er^{68}	Tm^{69}	Yb^{70}	Lu^{71}
$4f^2$ $6s^2$	$4f^3$ $6s^2$	$4f^4$ $6s^2$	$4f^5$ $6s^2$	$4f^6$ $6s^2$	$4f^7$ $6s^2$	$4f^7$ $5d$ $6s^2$	$4f^8$ $5d$ $6s^2$	$4f^{10}$ $6s^2$	$4f^{11}$ $6s^2$	$4f^{12}$ $6s^2$	$4f^{13}$ $6s^2$	$4f^{14}$ $6s^2$	$4f^{14}$ $5d$ $6s^2$
Th^{90} – $6d^2$ $7s^2$	Pa^{91} $5f^2$ $6d$ $7s^2$	U^{92} $5f^3$ $6d$ $7s^2$	Np^{93} $5f^4$ $7s^2$	Pu^{94} $5f^6$ $7s^2$	Am^{95} $5f^7$ $7s^2$	Cm^{96} $5f^7$ $6d$ $7s^2$	Bk^{97}	Cf^{98}	Es^{99}	Fm^{100}	Md^{101}		Lw^{103}

Table 1. Structure types and electrical character of the transition metal dichalcogenides

M \ X_2		$-S_2$	$-Se_2$	$-Te_2$	Electrical character
IV	Ti	L octa	L octa	L octa	Diamagnetic semiconductors.
d^2	Zr	L octa	L octa	L octa	$\rho \gtrsim 1$ ohm-cm, $E_g \sim 0{\cdot}2$–$2{\cdot}0$ ev.
	Hf	L octa	L octa	(L octa)	Ti, as with all first series metals, yields non-stoichiometric products.
V	V	(L octa)	L octa	L distd. octa	Undistorted compounds are narrow band metals, $\rho \sim 10^{-4}$ ohm-cm. Pauli paramagnetic → band antiferromagnetic. Superconducting. Free-carrier absorption in *I.R.*
d^3	Nb	L trig pr	L trig pr	L distd. octa	
	Ta	L {trig pr / (dist) octa}	L {trig pr / (dist) octa}	L distd. octa	Others diamagnetic semi-metals. Octa TaS_2/Se_2 perhaps semiconducting.
VI	Cr	—	–	—	(i) The undistorted compounds are diamagnetic semiconductors. $\rho \gtrsim 1$ ohm-cm. $E_g^{opt} \gtrsim 1{\cdot}5$ ev, $E_g^{th} \sim 0{\cdot}15$ ev.
d^4	Mo	L trig pr	L trig pr	L {trig pr / distd. octa}	(ii) The distorted octahedral structures are semi-metals. $\rho \sim 10^{-3}$ ohm-cm. Diamagnetic, low Seebeck coefficients.
	W	L trig pr	L trig pr	L distd. octa	
VII	Mn	Pyrites			(i) Mn compounds quasi-ionic antiferromagnetic semiconductors.
d^5	Tc	L dist octa	L dist octa	L distd.	(ii) TcS_2 possibly also a pyrite form.
	Re	L dist octa	L dist octa	L distd.	(iii) ReS_2 and $ReSe_2$ are small gap semiconductors, diamagnetic, and with no free-carrier absorption.
VIII a	Fe	Pyrite / Marcasite Pyrites			'Non-magnetic' semiconductors
d^6	Ru				
	Os				
VIII b	Co	Pyrite	{Pyrite / Marcasite}	{Marcasite / L octa}	Pyrite, marcasite and layer types metallic.
d^7	Rh	(Pyrite)	{$IrSe_2$ / Pyrite}	{Pyrite / L octa}	CoS_2 ferromagnetic. β-$RhSe_2$ and $RhTe_2$ superconductors.
	Ir	$IrSe_2$	$IrSe_2$	L octa	$IrSe_2$ types semiconducting.
VIII c	Ni	Pyrites		L octa	(i) Tellurides, metallic Pauli paramagnetic. $\rho \sim 10^{-5}$ ohm-cm. $PdTe_2$ superconducting.
d^8	Pd	Layer type showing X–X links		L octa	(ii) PdS_2/Se_2, PtS_2/Se_2 } semiconducting. $E_g \sim 0{\cdot}4$ ev. $\rho \sim 1$ ohm-cm. Diamagnetic, large Seebeck coefficients.
	Pt	L octa	L octa	L octa	

L octa : layer structure—octahedral coordination. L trig pr : layer structure—trigonal prism coordination.
L distd. : layer structure showing distorted coordination. High pressure forms given in table 15(*a*) p. 304.

The TX_2 layer materials form a structurally and chemically well-defined family. Electrically, however, they cover a wide spectrum of properties, from an insulator like HfS_2, through semiconductors like MoS_2 and semi-metals like WTe_2 and TcS_2, to true metals like NbS_2 and VSe_2. Several of the materials such as $TaTe_2$, WTe_2 and $ReSe_2$ show structural distortions that throw their properties out of line as compared with their undistorted analogues. 'Domains' have been observed in $NbTe_2$ and $TaTe_2$ reminiscent of the deformation twinning observed in VO_2 below 68°C. 1T–TaS_2 and 1T–$TaSe_2$ present a greater problem as their structure appears undistorted when examined by x-rays. Accordingly they should be metals, like VSe_2, but in fact they behave optically and magnetically as semiconductors. Electron microscope diffraction patterns do, however, indicate some type of superlattice. All the Nb and Ta materials, whether distorted or not, are superconducting, and the truly metallic ones also show band antiferromagnetism below about 150°K.

In order to illuminate the origin of these unusual properties more fully, an investigation has been made of the optical properties. Detailed transmission spectra were obtained in the range 0·5–5 ev from cleaved crystal specimens. Collectively, these allow band models to be set up for the whole range of compounds. The structural, optical and electrical properties are well accommodated. The diversity of properties arises through the existence of non-bonding d bands and the degree to which they are filled. In these dichalcogenides the d bands are quite wide (~ 1 ev) and lead to room temperature mobilities $\sim 100\ cm^2/v\text{-}sec$. Contrast is made between these materials and the layer dihalides, for which there is a progressive delocalization of the d electrons from say MnI_2 through FeI_2 and NiI_2 to TiI_2. It seems possible that this latter material may undergo a semiconductor to metal transition of the Mott type on cooling. The binary layer compounds are in fact ideal for investigating the course of d-band formation since the metal atoms lie in well-defined hexagonal sheets.

The basic atomic structure of loosely coupled X–M–X atom sheet sandwiches makes such materials extremely anisotropic, both mechanically and electrically. The conductivity perpendicular to the planes is down by a factor of at least 10^2 on that in the planes for MoS_2, etc., and there is some evidence that the carriers move by hopping rather than a band mechanism in the former direction. Thermal conductivity likewise is low perpendicular to the layers. In layer structures, moreover, the charge carriers and phonons seem to couple in a unique fashion.

In order to view these materials in the wider context of layer materials in general, the behaviour of the *non*-transition metal layer compounds has also been considered. Preliminary band schemes for several such compounds, e.g. GaS, Bi_2Te_3 and $SnSe_2$, are available and a good deal of data has been amassed on the first two. The families of GaS, CdI_2 and BiI_3 show excitonic absorption which makes for useful comparison with the excitons of the MoS_2 (group VI) family. These exciton states are interesting in their own right. For MoS_2, etc. they are of rather small radius

and are remarkably stable to pressure, temperature and crystal composition. Only very high concentrations of Ta or Re (~ 1 at. %) will lead, in say WSe_2, to a screening out of the excitonic binding interaction.

The non-layered half of the TX_2 dichalcogenide family (prototype FeS_2) is equally if not more varied in property from one member to the next than that of the layered compounds. Indeed, it is the progressive filling, within a given structure type, of the narrow non-bonding d bands, coupled with the increasing metal–metal atom orbital overlap between the 3d and 4d or 5d members, which gives the family as a whole a most interesting diversity in unity.

Fig. 1

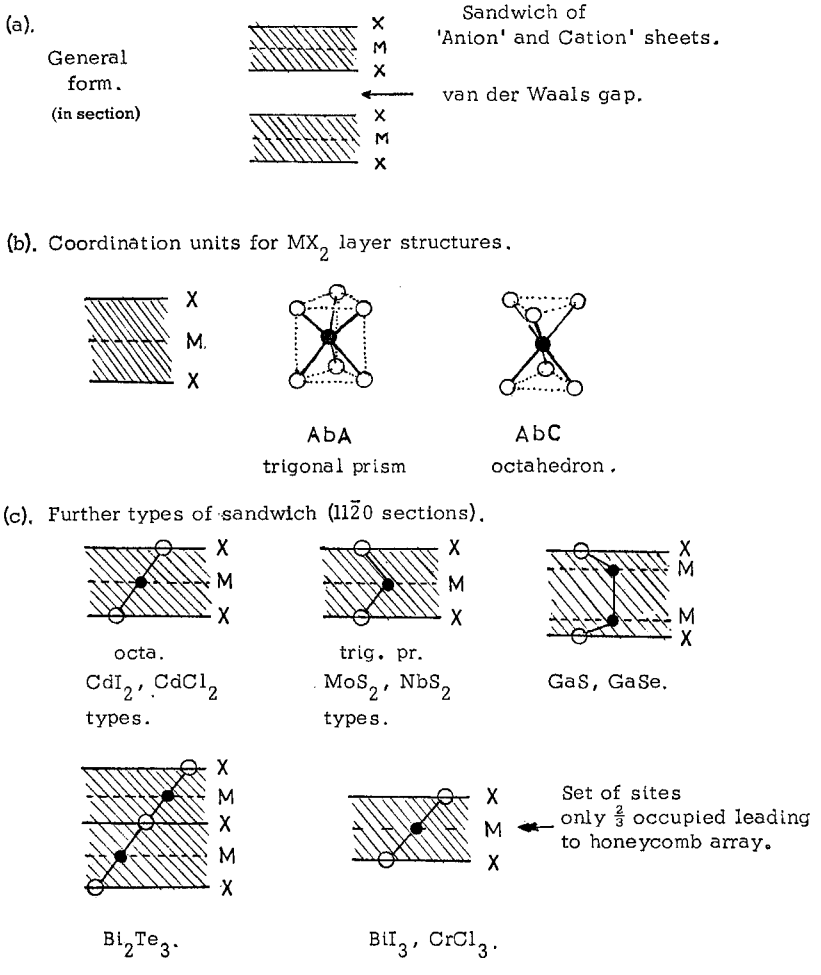

Basic form of layer compounds.

§ 2. The Structures of the TX_2 Dichalcogenides and Related Materials

The structures of the TX_2 dichalcogenides (see table 1) fall into two distinct classes—layered and otherwise. The layered materials arise from the stacking of hexagonally packed planes (not close packed) in the sequence shown in fig. 1 (*a*). 6 : 3 coordination results, that around the metal atoms being either trigonal prismatic (e.g. MoS_2, NbS_2) or octahedral (e.g. HfS_2, PtS_2). The coordination around the non-metal is quite lopsided, and this leads to the marked cleavage properties perpendicular to the hexagonal/trigonal symmetry axis (*z*). Several stacking polytypes exist. The commonest stacking of NbS_2 is one never adopted by the MoS_2 group VI family. Figure 2 contrasts the structures of the simplest polytypes, both in three dimensions and plan, whilst fig. 3 gives $11\bar{2}0$ sections for most polytypes so far reported in groups V and VI (Jellinek 1963, Haraldsen 1966, Zvyagin and Soboleva 1967). Several of the TX_2 materials occur with layer structures that are distorted in some way. The group VIII

Fig. 2

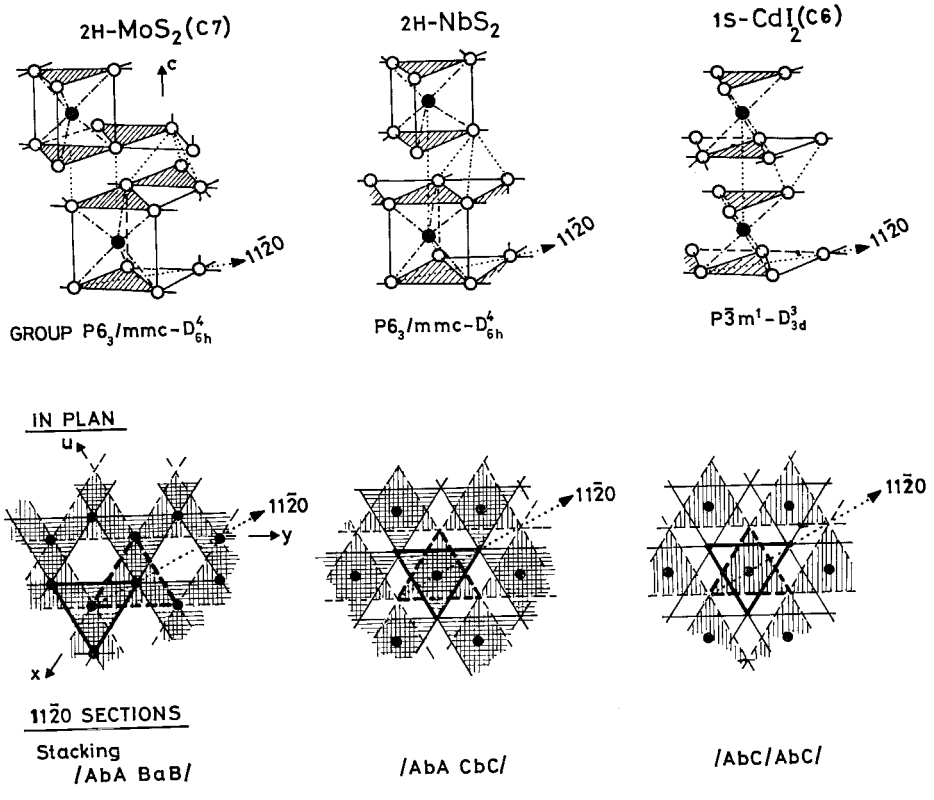

The structures of the 2H–MoS_2, 2H–NbS_2 and CdI_2 layer polytypes.

Fig. 3

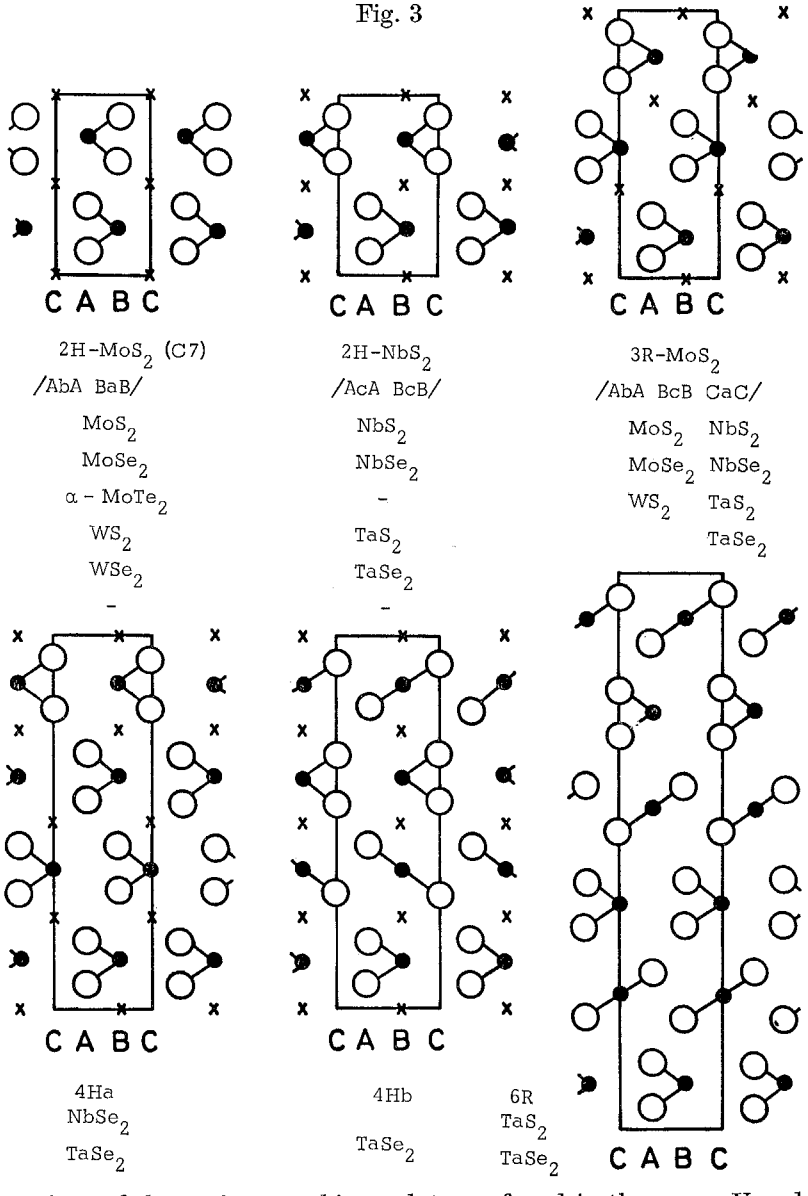

$11\bar{2}0$ sections of the various stacking polytypes found in the group V and VI TX_2 layer dichalcogenides. (c/a somewhat reduced. $C-C=\sqrt{3}a$.)]

layer compounds, and particularly the metallic tellurides, show considerable flattening of the TX_2 sandwich and a contraction of the van der Waals gap. Further, in the layer structures of $NbTe_2$, $TaTe_2$, β-$MoTe_2$, WTe_2, TcS_2, $TcSe_2$, ReS_2, $ReSe_2$ and $ReTe_2$ the metal atoms are actually displaced from the centre of the coordination units. Short metal–metal distances result with chains of metal atoms running through the structure. The

Fig. 4

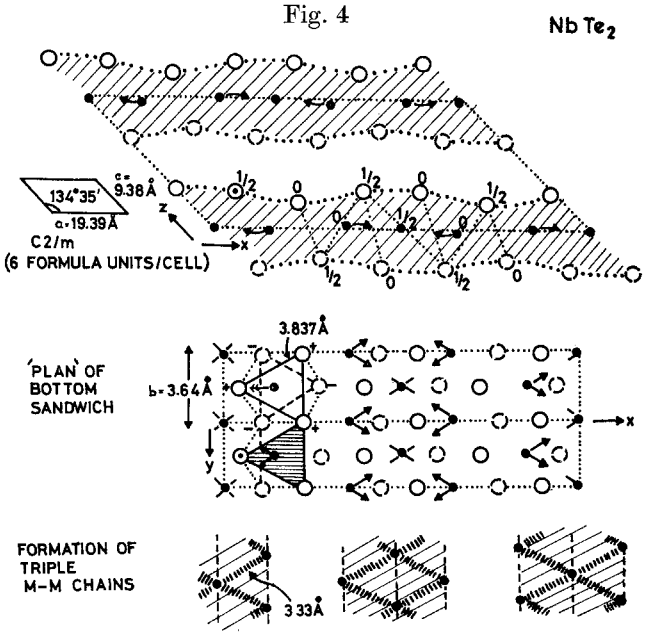

Distorted octahedral layer structure of $NbTe_2$ (and $TaTe_2$). [After Brown 1966 ; note : $a/3\sqrt{3}=3{\cdot}73$ Å as against 3·64 Å for b.]

Fig. 5

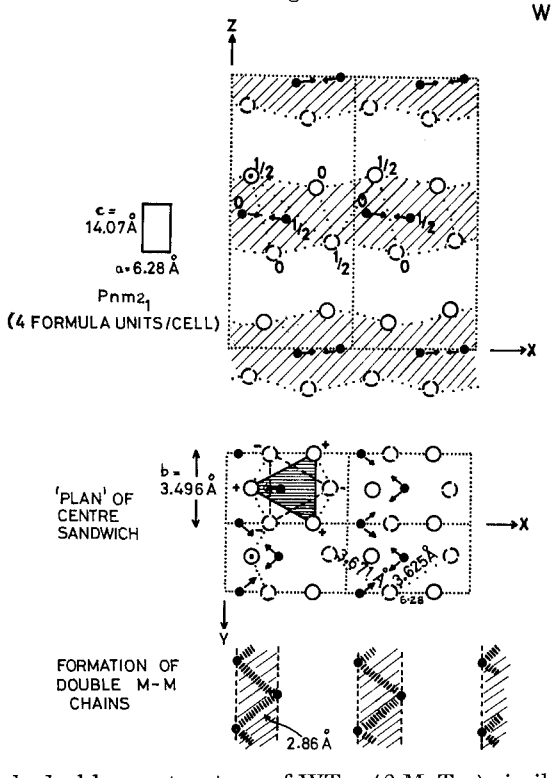

Distorted octahedral layer structure of WTe_2 (β-$MoTe_2$) similar. [After Brown 1966 ; note : $a/\sqrt{3}=3{\cdot}627$ Å as against 3·496 Å for b.]

Fig. 6

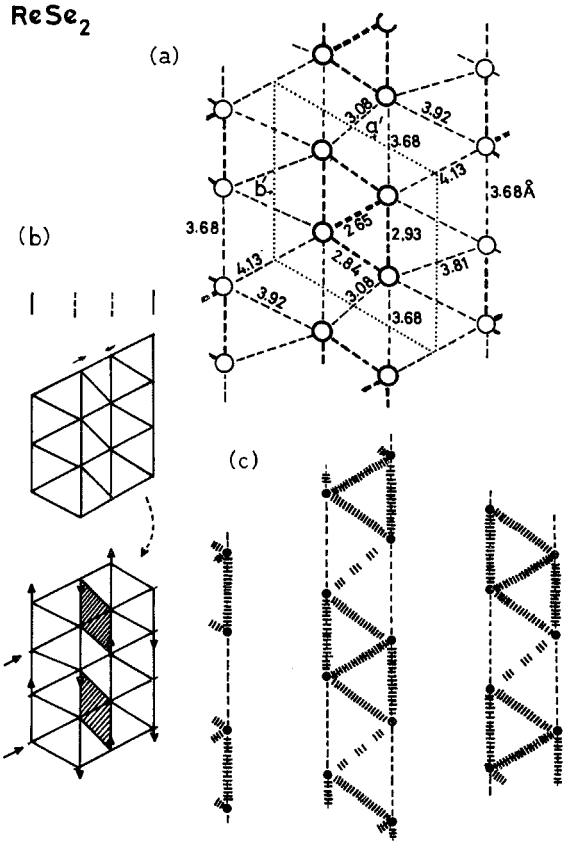

Distorted octahedral layer structure of $ReSe_2$. [After Alcock and Kjekshus 1965.] (*a*) Single distorted plane of rhenium atoms, (*b*) progressive distortion from CdI_2, (*c*) emphasizing cluster formation in chains.

chalcogenide sheets buckle somewhat to accommodate these shifts. Figures 4, 5 and 6 give interpretations of the reported structures for $NbTe_2$ ($TaTe_2$ same), WTe_2, (β-$MoTe_2$ similar) and $ReSe_2$ (to which ReS_2, TcS_2 and $TcSe_2$ seem similar). Such refined structural data as exist in the whole range of TX_2 layer dichalcogenides is collected into tables 2 and 3.

The non-layered TX_2 dichalcogenides occur exclusively in groups VII and beyond, and are of four types—pyrites, marcasite, $IrSe_2$ and PdS_2. Figure 8 illustrates the manner in which marcasite is related to CdI_2, whilst fig. 9 shows how pyrites is related to marcasite. The empty van der Waals gap is eliminated from these structures, and in fact they all show strong X–X pairing, particularly the sulphides. The cubic pyrite structure is the

Table 2. Structure parameters for the 'undistorted' TX_2 layer dichalcogenides (see also fig. 92 and table 18)

	a	c/s	c/a	Coordinate unit angles XMX||c	XMX$_{\perp c}$	Coordinate unit sandwich X–M ht.	Gap ht.	v.d.W. layer X–X	Inter-layer M–M	zMX sandwich angle (ρ)	v.d.W. length ratio (χ)	zOX gap angle (δ)	Reference
(*a*) Trigonal prism structures (2H polytype)													
NbS_2	3·31	5·94	1·796	79° 00′	84° 10′	2·47	3·14	2·80	3·39	5·94	50° 30′	0·92	53° 47′	Jellinek *et al.* (1960)
d^3 TaS_2	3·31$_5$	6·05	1·825											Jellinek (1962)
$NbSe_2$	3·45	6·27	1·821	80° 10′	82° 50′	2·60	3·36	2·91	3·52	6·27	49° 55′	0·88	53° 52′	Brown and Beerntsen (1965)
$TaSe_2$	3·436	6·348	1·847	80° 20′	82° 46′	2·59	3·35	3·00	3·59	6·35	49° 50′	0·90	52° 55′	Bjerkelund and Kjekshus (1967)
MoS_2	3·1604	6·147	1·945	82° 30′	81° 30′	2·41	3·19	2·96	3·47	6·41	48° 45′	0·91	50° 57′	Wildervanck and Jellinek (1964)
WS_2	3·154	6·181	1·960											Wildervanck and Jellinek (1964)
d^4 $MoSe_2$	3·288	6·460	1·962			2·49 ? →3·23		3·22	3·75					James and Lavik (1963)
WSe_2	3·286	6·488	1·976											Hicks (1964)
α-$MoTe_2$	3·517	6·981	1·984	83° 30′	80° 24′	2·73	3·63	3·35	3·92		48° 15′	0·89	50° 29′	Puotinen and Newnham (1961)
		(ideal | 1·816)								(ideal 49° 7′)		(ideal 54° 45′)	
(*b*) Octahedral coordination														
TiS_2	3·4048	5·6904	1·670		94° 26′	2·32	2·64	3·05	3·62	5·69	55° 20′	0·98	52° 11′	Bernard and Jeannin (1962)
ZrS_2	3·662	5·813	1·590											(*a*) McTaggart and Wadsley (1958)
HfS_2	3·635	5·837	1·606											(*b*) Greenaway and Nitsche (1965)
$TiSe_2$	3·535	6·004	1·698											(*b*) Greenaway and Nitsche (1965)
d^2 $ZrSe_2$	3·770	6·138	1·628											(*b*) Greenaway and Nitsche (1965)
$HfSe_2$	3·748	6·159	1·643											(*b*) Greenaway and Nitsche (1965)
$TiTe_2$	3·766	6·491	1·724											(*b*) Greenaway and Nitsche (1965)
$ZrTe_2$	3·950	6·630	1·678											(*b*) Greenaway and Nitsche (1965)
VSe_2	3·35	6·10	1·82											Røst and Gjertsen (1964)
d^3 VTe_2	3·6	6·45	1·8											Grønvold *et al.* (1958)
TaS_2	3·346	5·860	1·751											Jellinek (1962)
$TaSe_2$	3·477	6·272	1·804											Bjerkelund and Kjekshus (1967)
$CoTe_2$	3·86	5·30	1·38											Haraldsen *et al.* (1956)
d^7 $RhTe_2$	3·92	5·41	1·38											Geller (1955)
$IrTe_2$	3·929	5·395	1·373											Hockings and White (1960)
$NiTe_2$	3·8542	5·2604	1·368		95° 52′	2·596	2·734	2·526	3·41	5·260	58° 13′	0·78	60° 26′	Furuseth *et al.* (1965)
$PdTe_2$	4·0365	5·1262	1·270		99° 06′	2·652	2·533	2·593	3·49	5·126	61° 29′	0·79	60° 54′	Furuseth *et al.* (1965)
d^8 PtS_2	3·5432	5·0388	1·422		98° 26′	2·34	2·289	2·750	3·43	5·039	60° 42′	0·93	56° 06′	Furuseth *et al.* (1965)
$PtSe_2$	3·7278	5·0813	1·363		95° 44′	2·513	2·592	2·489	3·29	5·081	58° 57′	0·82	59° 57′	Furuseth *et al.* (1965)
$PtTe_2$	4·0259	5·2209	1·297		97° 34′	2·676	2·653	2·568	3·46	5·221	60° 18′	0·79	61° 05′	Furuseth *et al.* (1965)
		(ideal | 1·633)								(ideal 54° 45′)		(ideal 54° 45′)	

Table 3. Further structure parameters for the polytypic and distorted layer dichalcogenides of groups V, VI and VII

		a	c	c/a	Interbond ∠'s $\parallel c$	Interbond ∠'s $\perp c$	Bonding X–M	Sandwich ht.	Gap ht.	v.d.W. X–X	Interlayer M–M	Reference
Gr VI	2H–MoS_2	3·160	2×6·147	2×1·945	82° 30′	81° 30′	2·41	3·19	2·96	3·47	6·41	Swanson *et al.* (1955)
	3R–MoS_2	3·164	3×6·130	3×1·936	81·8°	82·1°	2·41	$3{\cdot}15_5$	2·98	3·50		Takeuchi and Nowacki (1964)
												Wildervanck and Jellinek (1964)
	2H–$MoSe_2$	3·288	2×6·460	2×1·962	80° 49′		2·49	3·23	3·22	3·75		James and Lavik (1963)
	3R–$MoSe_2$	3·292	3×6·464	2×1·965								Towle *et al.* (1966)
	2H–WS_2	3·154	2×6·181	2×1·960								Swanson *et al.* (1958)
	3R–WS_2	3·162	3×6·167	3×1·950								Wildervanck and Jellinek (1964)
	2H–α$MoTe_2$	3·517	2×6·983	2×1·984	83·5°	80·4°	2·73	3·63	3·35	3·92		Puotinen and Newnham (1963)
	β$MoTe_2$	3·66(av)	2×6·913	1·89			For a taken average Te–Te in layers. For c taken c . sin β. c/a values very large for octahedral coordinate.					Brown (1966)
	WTe_2	3·65(av)	2×7·036	1·93								Brown (1966)
Gr V	2H–NbS_2	3·31	2×5·945	2×1·796	79° 00′	84° 10′	2·47				5·945	Jellinek *et al.* (1960)
	3R–NbS_2	3·33	3×5·967	3×1·783								Jellinek *et al.* (1960)
	2H–$NbSe_2$	3·449	2×6·27	2×1·821	80° 10′	82° 50′	2·60	3·36	2·91	3·52	6·27	Brown and Beerntsen (1965)
	3R–$NbSe_2$	3·45	3×6·29	3×1·824			2·59	3·32	2·97	3·54	6·29	Brown and Beerntsen (1965)
	4H–$NbSe_2$	3·44	4×6·31	4×1·835			2·60	3·38	2·93	3·55	6·31	Brown and Beerntsen (1965)
	2H–TaS_2	3·315	2×6·05	2×1·826								Jellinek (1962)
	3R–TaS_2	3·32	3×5·937	3×1·797								Jellinek (1962)
	2H–$TaSe_2$	3·434	2×6·348	2×1·849	80° 20′	82° 46′	2·59	3·35	3·00	3·59	6·35	Brown and Beerntsen (1965)
	3R–$TaSe_2$	3·435	3×6·392	3×1·861								Bjerkelund and Kjekshus (1967)
	4H–$TaSe_2$	3·46	4×6·29	4×1·82								Brown and Beerntsen (1965)
	1T–TaS_2	3·346	5·860	1·751			Note a slightly larger than for trigonal prism forms. c/a large for an octahedral structure.					Jellinek (1962)
	1T–$TaSe_2$	3·477	6·272	1·804								Bjerkelund and Kjekshus (1967)
	$NbTe_2$	3·75	6·677	1·78			For a taken av. Te–Te in layers. For c taken c . sin β.					Brown (1966)
	$TaTe_2$	3·74	6·720	1·80								Brown (1966)
Gr VII	ReS_2											
	$ReSe_2$	3·30	6·343	1·92			c taken as separation of metal sheets. a taken as $\frac{1}{2}b$ (triclinic cell).					Alcock and Kjekshus (1965)

Fig. 7

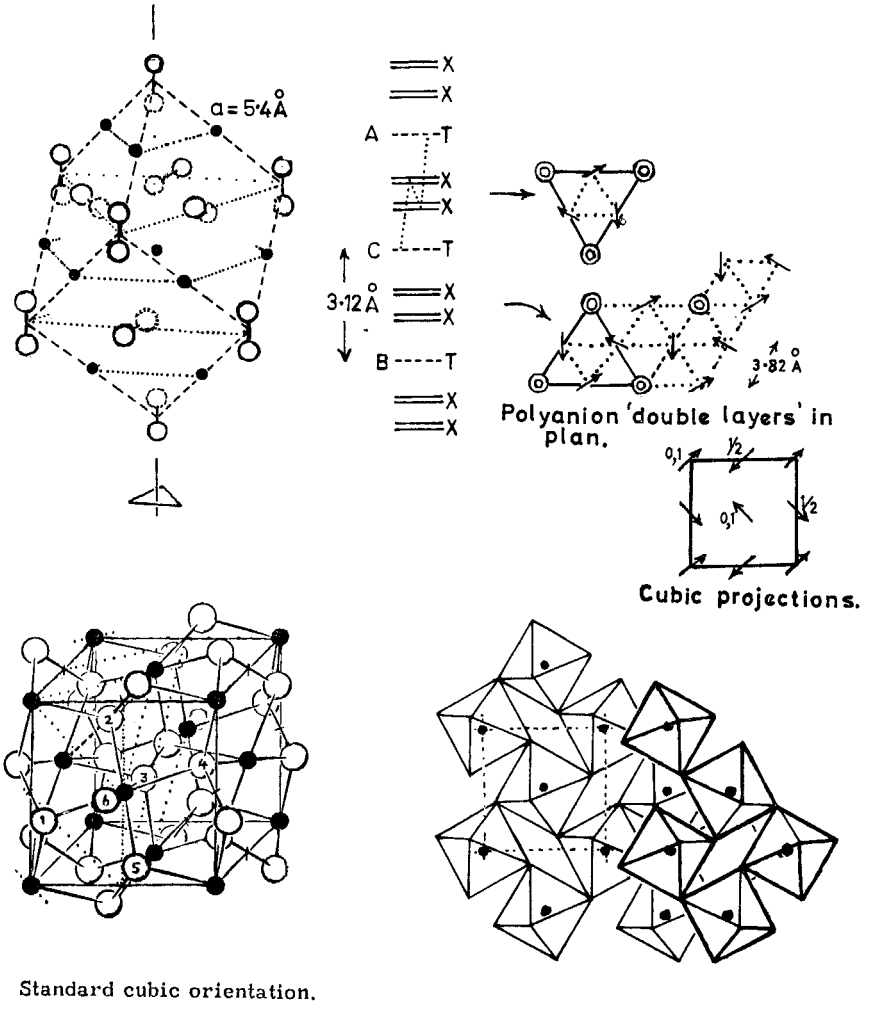

The pyrites structure (C2). [After Hulliger.]

densest and the other three structures are intermediary between the pyrite and CdI_2 structures, e.g.

(*a*)	NiS_2	PdS_2	PtS_2
	(pyrites)	(special)	(CdI_2)
(*b*)	RhS_2	α-$RhSe_2$	β-$RhTe_2$
	(pyrites)	($IrSe_2$)	(CdI_2)
(*c*)	h.p. $CoTe_2$	l.t. $CoTe_2$	h.t. $CoTe_2$
	(pyrites)	(marcasite)	(CdI_2)
Vol/formula unit			
	62·8	64·8	68·5 Å^3

Fig. 8

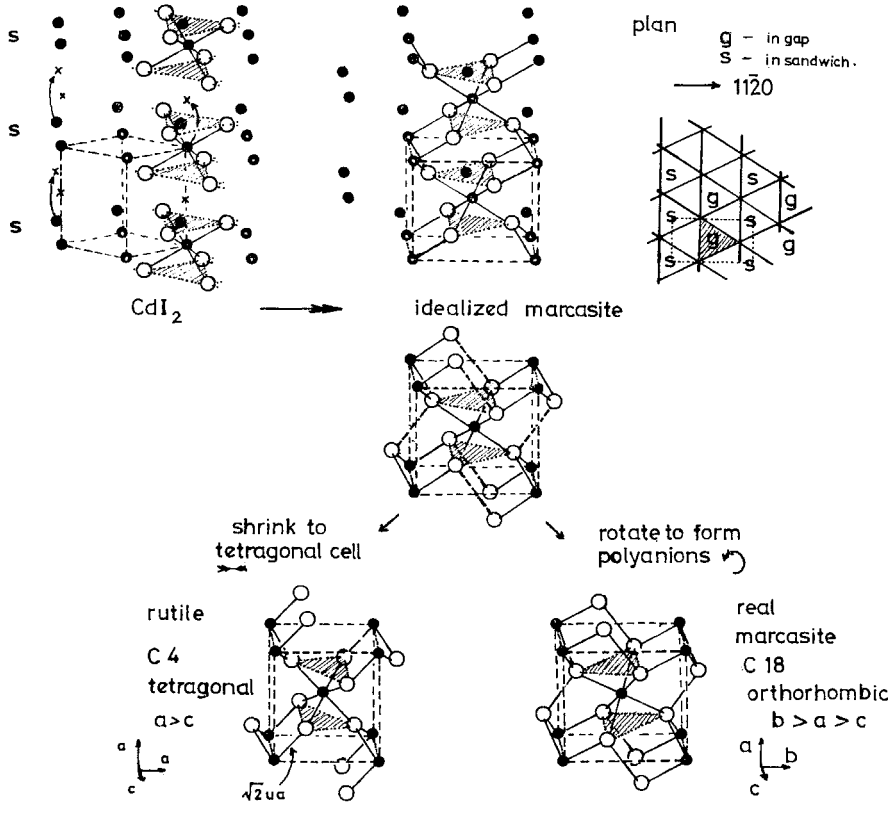

Relation of the marcasite (C18) and rutile (C4) structures to CdI_2 (C6). [After Hulliger and Mooser 1965.] Further details of marcasite structure in fig. 9 ; of rutile structure in fig. 73.

Fig. 9

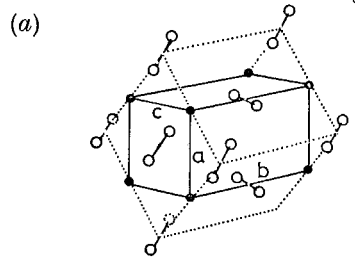

Orthorhombic marcasite structure inscribed in pyrite forming unit.

To reach cubic pyrite—
(1) expand c, contract a.
(2) swing face-centring X–X pairs ‖ to body diagonals.

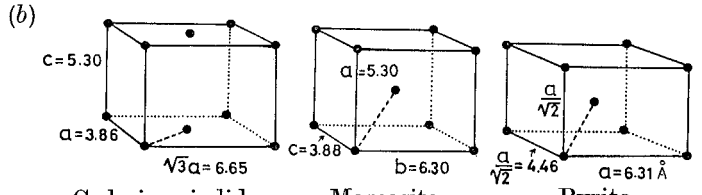

	Cadmium iodide.	Marcasite.	Pyrite.
c/a eff	1·38	1·364	1·000
	(c small—ideal $c/a=1·633$)		
Vol/2 f.u.	137	129·6	125·6 Å^3
	1·09 :	1·03 :	1·00

(a) Relation of the marcasite to the pyrite structure, (b) comparison of the three forms of $CoTe_2$.

Figures 10 and 11 show the unusual intermediate structure types of $IrSe_2$ and PdS_2.

Fig. 10

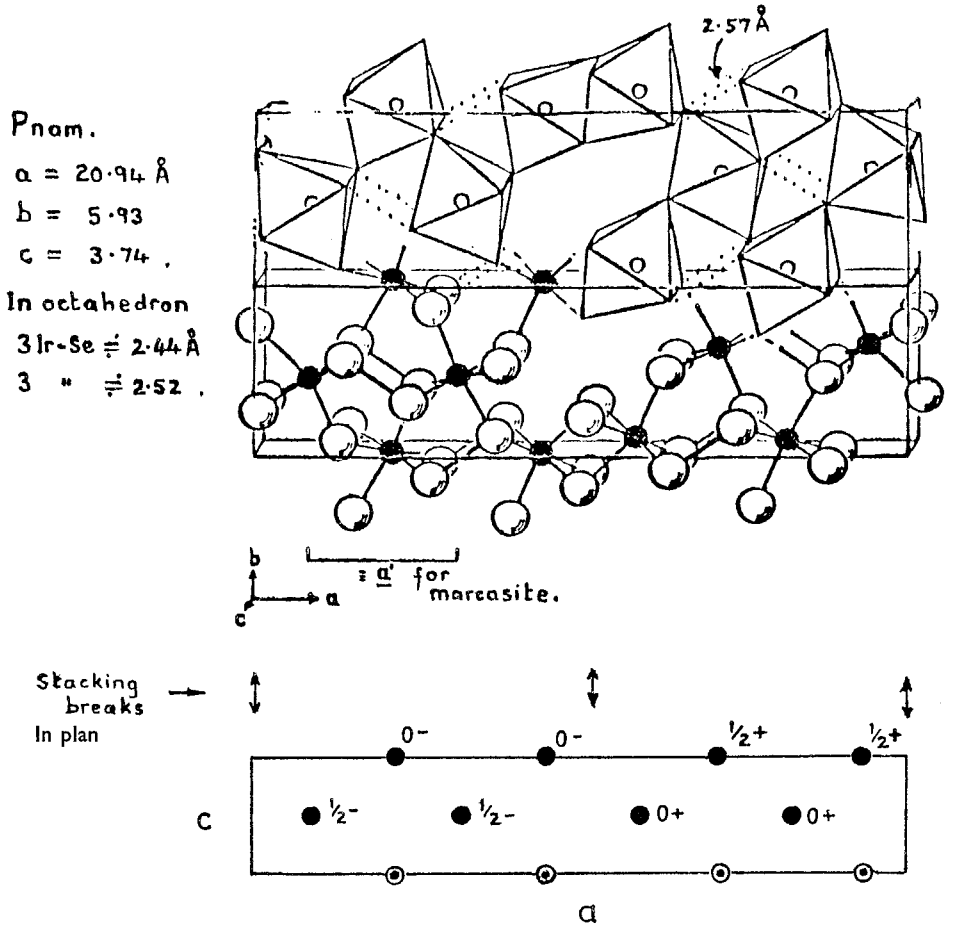

$IrSe_2$ structure (orthorhombic). [After Hulliger and Mooser 1965.]

Table 4 provides a collection of lattice parameters for the non-layered compounds to complement tables 2 and 3. Despite their greater density, the metal–metal distance in these non-layered compounds is increased. Figure 12 plots by groups the volume per formula unit, whilst fig. 13 likewise plots the nearest M–M distance for all the TX_2 materials. Table 5 gives the smallest X–X distance in the various compounds. Note how in the pyrite α-$RhTe_2$ the Te–Te pairing is much weakened relative to say $RuTe_2$, although X–X interaction still persists in $PdTe_2$ relative to say α-$MoTe_2$.

Table 4. Some structure parameters for the non-layered TX_2 dichalcogenides—including shortest metal–metal distance

(*a*) Pyrites. Cubic, structure C2. Group T_h^6 (Pa3). Four formula units/cell. Structure parameter u yields X–X and T–X distances via $\sqrt{3}a.(1-2u)$ and $a(3u^2-2u+\frac{1}{2})^{1/2}$ respectively. Least metal–metal distance $=\frac{1}{2}\sqrt{(2a^2)}$

	MnS_2	$MnSe_2$	$MnTe_2$	TcS_2			ReS_2		
a	6·109	6·430	6·951 Å	?			5·57		
M–M	4·319	4·560	4·915				—		
	FeS_2	$FeSe_2$	$FeTe_2$	RuS_2	$RuSe_2$	$RuTe_2$	OsS_2	$OsSe_2$	$OsTe_2$
a	5·405	5·783*M	6·292*M	5·59	5·921	6·360	5·6075	5·933	6·369 Å
M–M	3·822	4·089	4·499	3·953	4·187	4·497	3·965	4·195	4·503
	CoS_2	$CoSe_2$	$CoTe_2$	RhS_2	β-$RhSe_2$	α-$RhTe_2$			
a	5·535	5·849M	6·310*M,C	5·73	6·092 $IrSe_2$	6·441C			
M–M	3·914	4·136	4·462	4·051	4·307	4·554			
	NiS_2	$NiSe_2$	$NiTe_2$						
a	5·685	5·960	6·374*C Å						
M–M	4·019	4·214	4·507						
	CuS_2	$CuSe_2$	$CuTe_2$						
a	5·790*	6·123*M	6·600*C? Å						
M–M	4·093	4·330	4·667						
	ZnS_2	$ZnSe_2$	$ZnTe_2$	CdS_2	$CdSe_2$	$CdTe_2$		$MgTe_2$	
a	5·954*	6·290*	*C Å	6·309*	6·615*	*C Å		7·025*Å	
M–M	4·210	4·447							

Alternative forms. M : marcasite. C : cadmium iodide. * : high pressure form.

(*b*) Marcasites. Orthorhombic, C18. Group D_{2h}^{12} (Pnnm). Two formula units/cell. Structure parameters x and y yield :

X–X (1) $=[4x^2a^2+(1-2y)^2b^2]^{1/2}$, M–X (4) $=[x^2a^2+y^2b^2]^{1/2}$,
M–X (2) $=[(\frac{1}{2}-x)^2a^2+(\frac{1}{2}-y)^2b^2+\frac{1}{4}c^2]^{1/2}$

FeS_2			$FeSe_2$			$FeTe_2$			$CoTe_2$			
a	*b*	*c*	*a*	*b*	*c*	*a*	*b*	*c*	*a*	*b*	*c*	
4·436	5·414	3·381	4·791	5·715	3·575	5·340	6·260	3·849	5·301	6·298	3·882	Å

FeS_2M : Fe–S 2·23 and 2·25 Å, S–S = 2·21 Å.

(*c*) $IrSe_2$. Orthorhombic. Group D_{2h}^{16} (Pnam). Eight formula units/cell

	a	*b*	*c*
$RhSe_2$	20·91	5·951	3·709 Å
IrS_2	19·78	5·624	3·565
$IrSe_2$	20·94	5·93	3·74

Least M–M ≡ c

$IrSe_2$: Ir–Se 3 at *ca.* 2·44, 3 at *ca.* 2·52 ; Se–Se short 2·57, long 3·27 Å.

(*d*) PdS_2. Orthorhombic. Group D_{2h}^{15} (Pbca). Four formula units/cell

	a	*b*	*c*	Pd–X	X–X^{least}	Pd–Pd^{least}
PdS_2	5·460	5·541	7·531	2·30	2·13	3·89 Å
$PdSe_2$	5·741	5·866	7·691	2·44	2·36	4·11

Fig. 11

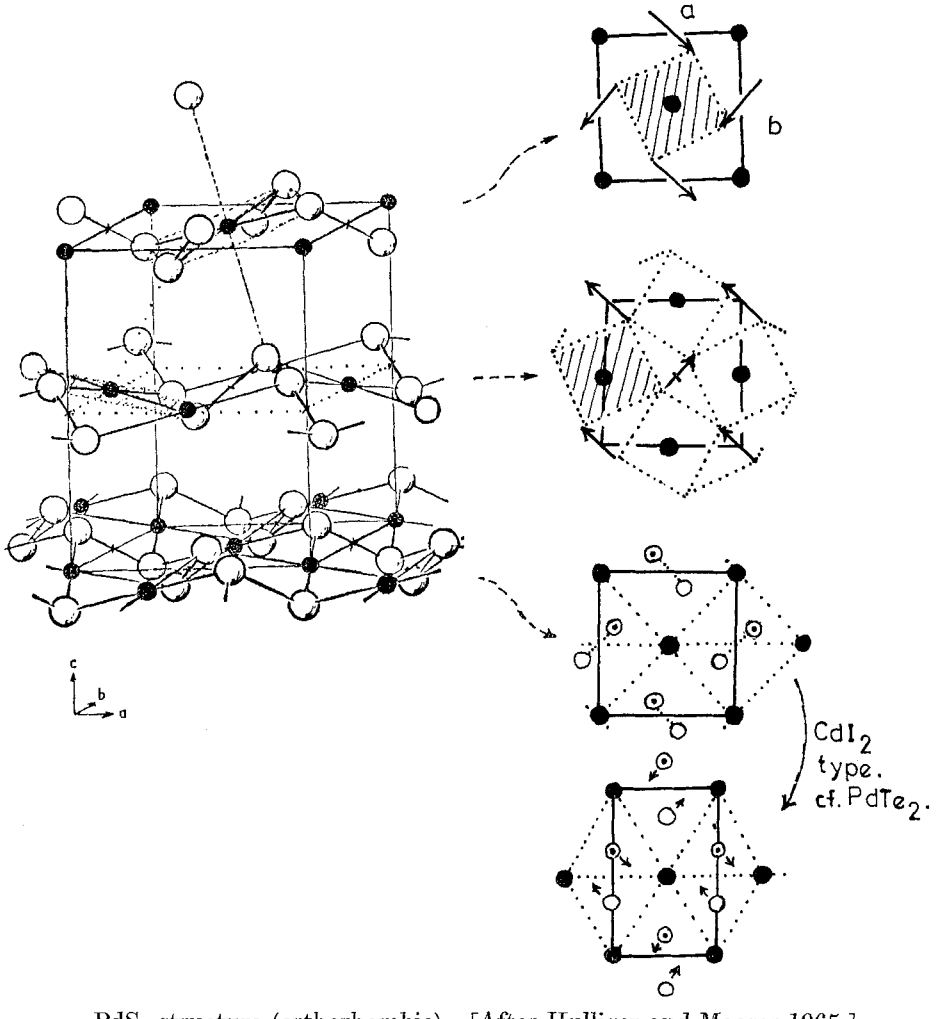

PdS_2 structure (orthorhombic). [After Hulliger and Mooser 1965.]

Short X–X distances are also found in the rutile structure, adopted by many of the TO_2 dioxides. As was shown in fig. 8, the rutile structure (C4) is closely related to that of marcasite (C18). Some of the dioxides also undergo distortion with metal–metal pairing $\|c$ below a certain temperature (e.g. VO_2, 68°C). Table 6 shows all the structures of the TO_2 dioxides; the more ionic dioxides ZrO_2 and HfO_2 adopt the higher coordination 8 : 4 fluorite structure. The marcasite structure also can suffer metal–metal bonding $\|c$, either as alternating contractions (as in the arsenopyrites like RhP_2), or as a general contraction (in compounds like RuP_2—isoelectronic with MoS_2)—see Hulliger (1965). Again isoelectronic with MoS_2 is $ZrCl_2$.

Table 5. Least X–X atom distances in the TX_2 dichalcogenides

(*a*) S–S distances

MnS_2	FeS_2		CoS_2	NiS_2
	M	P		
2·084	2·210	2·136	2·10	2·06 Å
MoS_2	TcS_2	RuS_2	RhS_2	PdS_2
Through sandwich	v.d.W.			Through sandwich	v.d.W.
3·19	3·47	2·41		2·13	(3·92)
HfS_2	ReS_2	OsS_2	IrS_2	PtS_2
				Through sandwich	v.d.W.
~3·6		2·43		3·06	3·43

(*b*) Se–Se distances

$MnSe_2$	$FeSe_2$		$CoSe_2$	$NiSe_2$
	M	P	M P	
2·38	2·50		2·53	2·394
$TcSe_2$	$RuSe_2$		$RhSe_2$	$PdSe_2$
			P I	Through sandwich	v.d.W.
	2·46		2·50	2·36	(3·75)
$ReSe_2$	$OsSe_2$		$IrSe_2$	$PtSe_2$
				Through sandwich	v.d.W.
v.d.W. ~3·3	2·47		2·57 (and 3·27)	3·374	3·29

(*c*) Te–Te distances

$MnTe_2$	$FeTe_2$		$CoTe_2$			$NiTe_2$
						Through sandwich	v.d.W.
	M	P	M	C	P		
2·745	2·616		2·924			3·48	3·41
α-$MoTe_2$	$TcTe_2$	$RuTe_2$		$RhTe_2$		$PdTe_2$
Through sandwich	v.d.W.			P	C	Through sandwich	v.d.W.
3·63	3·92	2·64		3·087		3·44	3·49
	$ReTe_2$	$OsTe_2$		$IrTe_2$		$PtTe_2$
						Through sandwich	v.d.W.
		2·64				3·53	3·46

Fig. 12

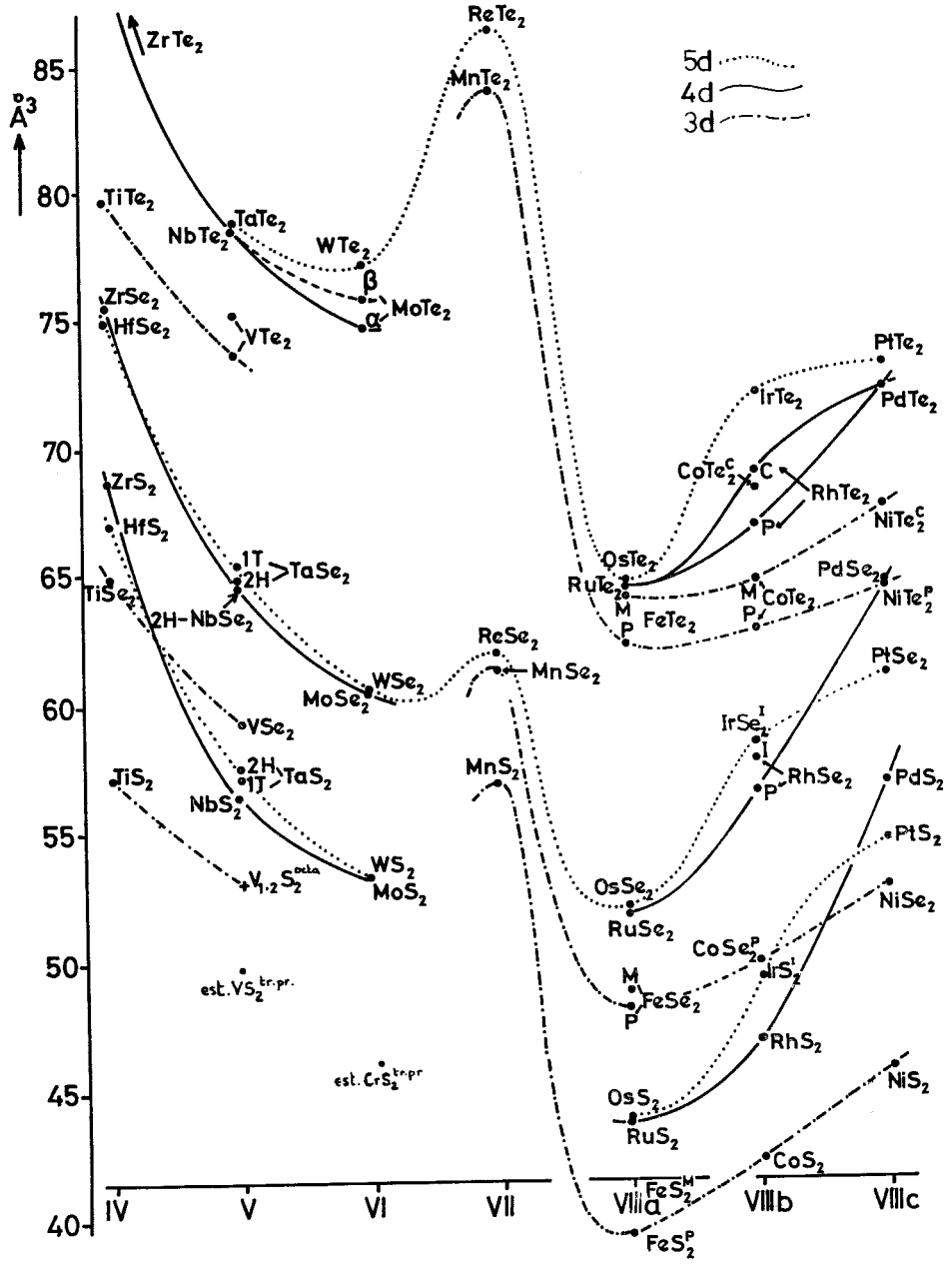

Plot by group number of the volume per formula unit for the TX_2 dichalcogenides.

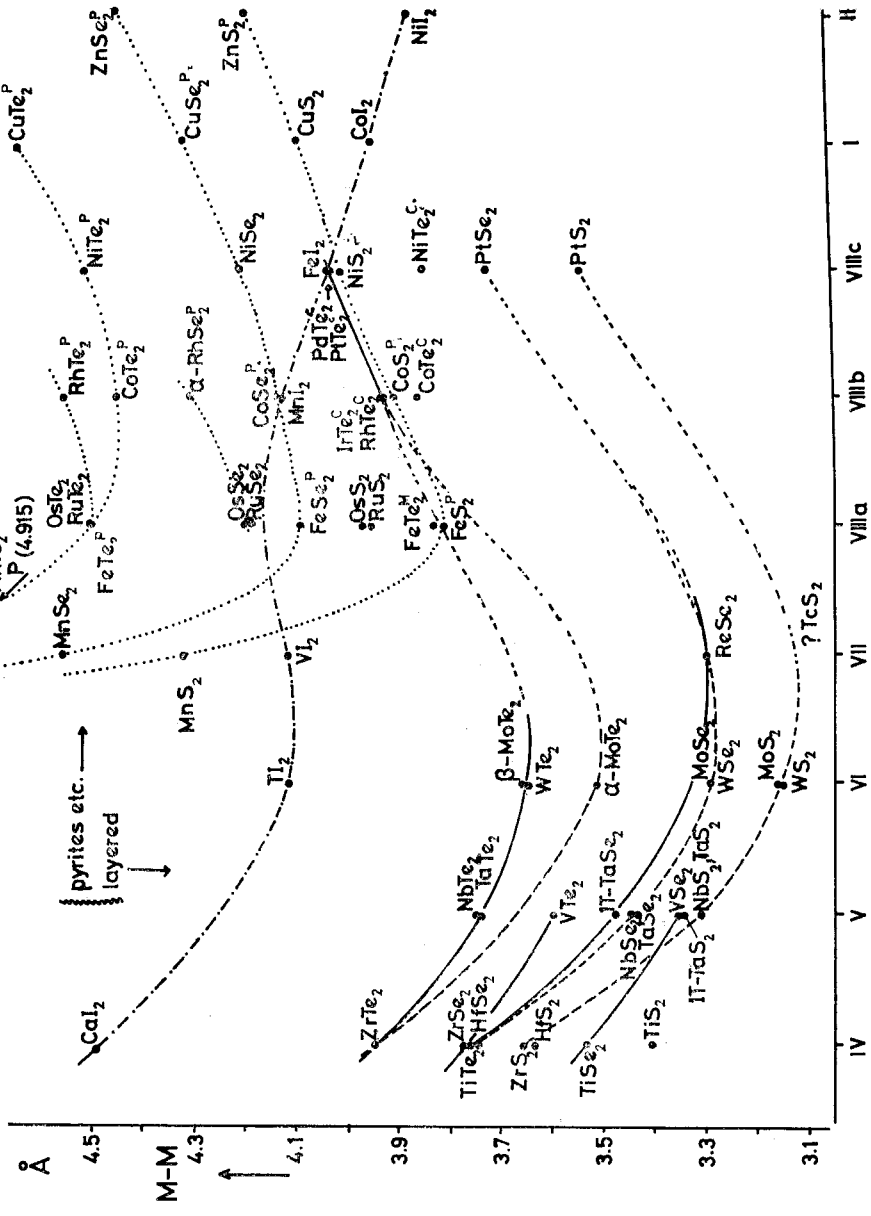

Plot by group number of the shortest metal–metal distance in the TX_2 dichalcogenides. (Halides in isoelectronic position.)

Fig. 13

This layer compound is rather unstable; the anhydrous dihalides of the first period (3d) are more manageable; all crystallize in CdI_2 or related forms. Figure 14 is a plot for the full range of MX_2 layer compounds of c/a against the distance between X–X cores (obtained using Waber's core radii, and lattice parameters from Slater (1965), pp. 103 and 308 ff respectively)).

This plot is discussed later, but is seen to group the compounds by metal valency (viz. 2, 4, 5, 6). The origins of structural development through the transition metal dichalcogenides are discussed towards the end of the review in § 9.2.

Fig. 14

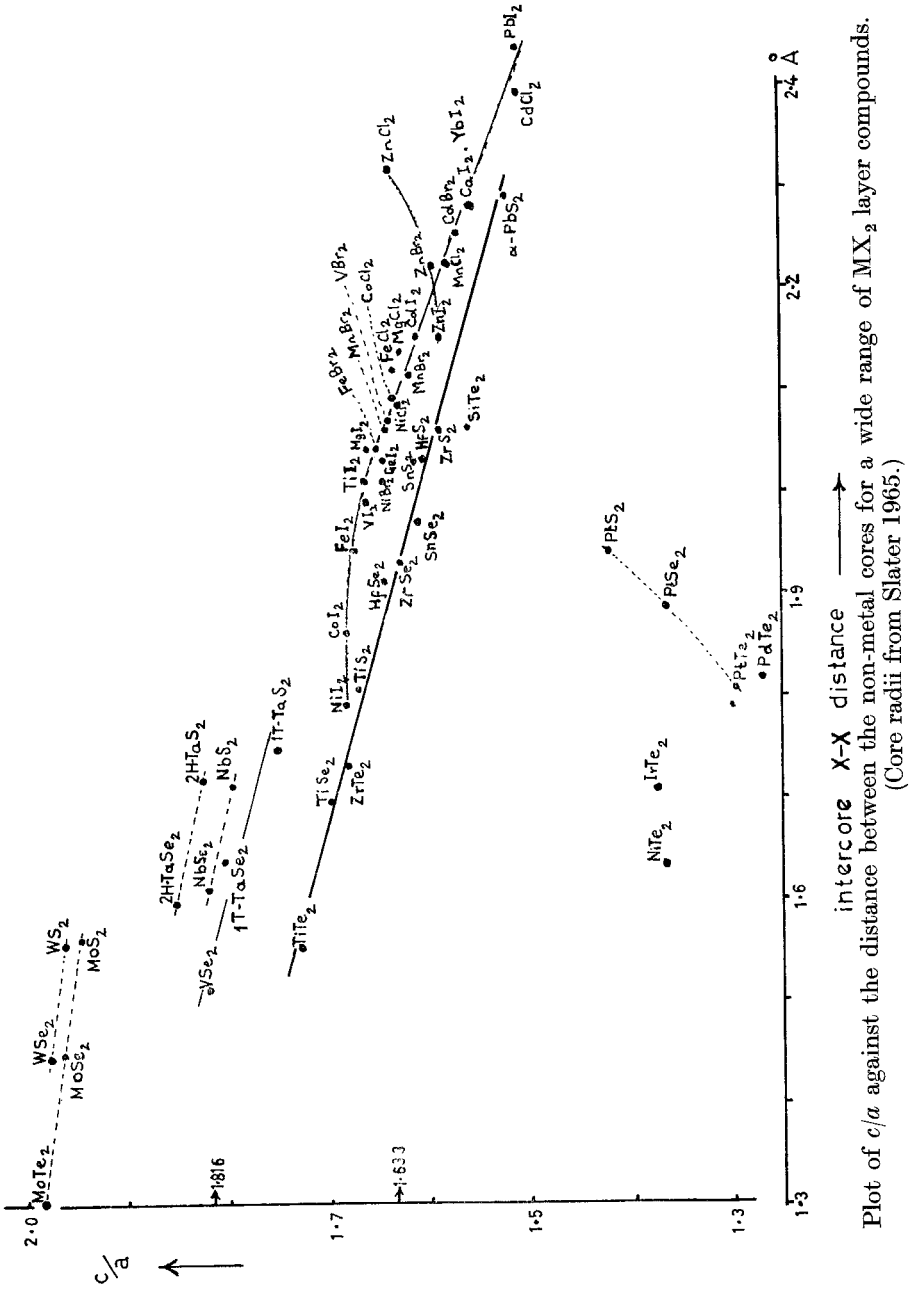

Plot of c/a against the distance between the non-metal cores for a wide range of MX_2 layer compounds. (Core radii from Slater 1965.)

Table 6. TO_2 dioxide structure types

	Ti	V	Cr	Mn	Fe	Co	Ni
3d	C4 *et al.*	C4*	C4	C4 *et al.*	—	—	—
	Zr	**Nb**	**Mo**	**Tc**	**Ru**	**Rh**	**Pd**
4d	C4, C1	C4*	C4*	C4*	C4	C4	—
	Hf	**Ta**	**W**	**Re**	**Os**	**Ir**	**Pt**
5d	C1	C4	C4*	C4* *et al.*	C4	C4	C4

See Sleight *et al.* 1969.

* Distorted by metal–metal bonding.

Obviously the extremely anisotropic character of the layer compounds, built in at the atomic level, dominates all the properties of such materials, both mechanical and electrical. The expansion coefficient is about a factor of 10 greater perpendicular to the layers than parallel (Brixner 1963); conversely the velocity of sound in this latter direction is twice that parallel to *c* (Guseinov and Rasulov 1966). The thermal conductivity is also up by almost a factor of 10 parallel to the layers. Under applied pressure this factor falls rapidly as the structure stiffens mechanically (Guseinov and Rasulov 1966). Electrical conduction in the two directions is even more different, at least for MoS_2, where a difference factor of 10^3 seems likely. Another result of the weak van der Waals binding is that the inter-sandwich gap will open up to accept alkali metal ions from ammonia solution. ('Intercalation', c.f. graphite, see p. 285). These intercalates will later be compared to the 'tungsten bronzes'. One problem, particularly with the 3d dichalcogenides, is poor stoichiometry. The TX_2 structures can readily be transformed (fig. 15) into TX structures like NiAs or NbS by filling the vacant sites of the van der Waals region with metal atoms (Jellinek 1963). Often a continuous solid solution exists (e.g. Ni/Te—Barstad *et al.* 1966), or superlattices may condense out (e.g. Ti/S). Moreover, at a given temperature the equilibrium products may lie far from

Fig. 15

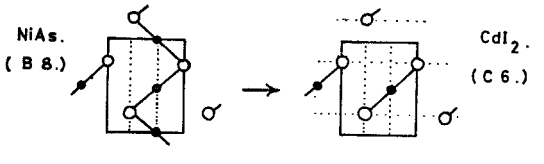

Relation of the TX_2 layer structures to TX structures.

Table 7. Stacking polytypes of the group VI materials—experimental results

Method of determination		Synthetic material: Powder synthesized, Normal pressure	Synthetic material: Powder synthesized, High pressure	Synthetic material: Low temperature transport 650 to 800°C, Load microcrystal	Synthetic material: Low temperature transport 650 to 800°C, Transport crystal	Synthetic material: High temperature transport 800 to 1050°C, Load microcrystal	Synthetic material: High temperature transport 800 to 1050°C, Transport crystal	Natural crystals	
MoS_2	x-ray	2H sharp	—	—	3R/2H diffuse	—	3R (950°C) sharp	2H sharp	3R sharp
	Kikuchi	—	—	—	3R (750°C)	—	—	2H	3R
Optical positions of A and B pair cm^{-1}				14750	14850			14·7 14860	14750
				15950	16000			16·3 16360	15930
	300°K	—	—	1200	1150	—	—	1·6 1500	1180
				15400	15430			15420	15270
				16610	16630			17040	16450
	77°K	—	—	1210	1200	—	—	1620	1180
				Note slightly higher than for natural 3R				↑ reflc.	
$MoSe_2$	x-ray	—	3R/(2H) sharp	2H sharp	2H/(3R) diffuse	—	2H sharp		
	Kikuchi	—	—	—	3R	—	—		
					Brixner 650°C 780°C				
Optical positions of A and B pair cm^{-1}			12300		12300 12330 12250		12320		
			14050		14100 14150 14380		14410		
	300°K	—	1750	—	1800 1820 2130	—	2090 (900°C)		
			12850		12850 12930 12770		12850		
			14600		14700 14730 14920		15040		
	77°K	—	1750	—	1850 1800 2150	—	2190		

WS_2	x-ray	2H sharp	3R sharp	—	—	—	3R (900°c) sharp	Composition, +6% Mo ? 2H
	Kikuchi	3R like	—	—	3R	—	—	—
Optical positions of A and B′ pair cm^{-1}		15650 18650	15600 18950		15650 18950			15·08 17·80
	300°K	3000	3350	—	3300	—	—	2·72
		↑ refln.	16190 19530		16220 19530			15·51 18·25
	77°K		3340	—	3310	—	—	2·74
WSe_2	x-ray	—	—	—	2H/3R diffuse	2H sharp	2H sharp	
	Kikuchi	—	—	—	3R	—	—	
Optical positions of A and B pair and A′ cm^{-1}					13150 17850 16850			
	300°K	—	—	—	3700	—	—	
					13720	13850	13760	
					18150 17450	18040 17680	18150 17560	
	77°K	—	—	—	3730	3830	3800	

α-$MoTe_2$, all tests give 2H. β form obtained above about 920°c.

Optical positions of A and B, 300°K $\left.\begin{matrix}8410\\11150\end{matrix}\right\}$ 2740, 77°K $\left.\begin{matrix}8980\\11710\end{matrix}\right\}$ 2730 cm^{-1}.

simple stoichiometry, e.g. a 2 to 1 S/Ti powder mixture yields $TiS_{1\cdot94}$ at 800° and $TiS_{1\cdot92}$ at 1000°C (Bernard and Jeannin 1962). This non-stoichiometric tendency is least marked for the third period (5d) materials, and for the compounds of group VI. Cleavage of non-stoichiometrics like 'VS_2' or '$CoTe_2$' is noticeably more difficult than for say MoS_2. The cleavage properties of the stoichiometric materials are indeed quite remarkable. The crystals are not friable and may be pulled apart on sello-tape. Through repeated cleaving it is easy to obtain specimens 200 μ square and only 500 Å thick. For such a thickness even when the absorption coefficient rises to $5 \times 10^5\,cm^{-1}$ the crystal will still transmit 2% of the incident light.

§ 3. TX_2 Layer Compounds—the Crystals

Only MoS_2 occurs naturally in appreciable quantities. The other crystals are best obtained by chemical vapour transport (Schafer 1964). The TX_2 dichalcogenides do not in general melt until above 1000°C, and then only with decomposition. This same technique has been used to obtain anhydrous TX_2 dihalides, and also layer materials like CdI_2 and SnS_2 which could otherwise be grown from solution and the melt respectively. The most convenient carrier gas is iodine, though bromine and chlorine are sometimes required. The carrier concentration was kept low to avoid contamination ($\sim 1\,mg/cm^3$), though Kershaw *et al.* (1967), Hicks (1964) and Conroy and Park (1968) all report remarkably little take up (e.g. iodine in HfS_2 $\sim 10^{15}$ atoms/cm^3). With our two-zone furnaces the crystals were typically only 1 to 2 mm across, but this was found quite adequate for our purposes. (Larger crystals up to a centimetre in diameter have been grown in other laboratories.) The group V crystals were particularly easy to obtain. For α-$MoTe_2$ crystals with thicknesses of 1 mm were repeatedly obtained, based on clearly marked growth spirals. Crystals of the rhenium compounds grew to very large areas but maintained thicknesses ~ 2000 Å or less. Most of the crystals are quite stable though the groups V and IV compounds tarnish slowly. Additional experimental data concerning crystal growth, etc. is reported elsewhere (Wilson 1969 a).

Naturally occurring MoS_2 has been found in the 3R (Graeser 1964) as well as with the common 2H sandwich stacking (see fig. 3). Our transport crystals of MoS_2 in fact were always of the 3R form. The two types belong to different space groups and their spectra show remarkably different magnitudes of spin–orbit splitting for the pair of excitons situated on the absorption edge (see p. 243). The same has now been found for the $MoSe_2$ and WS_2 polytypic forms. Table 7 gives the conditions under which the various specimens were obtained and the means by which they were identified. The polytypes are easily distinguishable by (*a*) the spin–orbit splitting, (*b*) by x-ray powder analysis (see fig. 18), and (*c*) in some cases by the form of the Kikuchi banding seen on electron microscope diffraction patterns (e.g. MoS_2, fig. 16). This latter method is sometimes misleading; thus, although 2H–MoS_2 gives an hexagonal 6-planar star, and 3R–MoS_2 a

Fig. 16

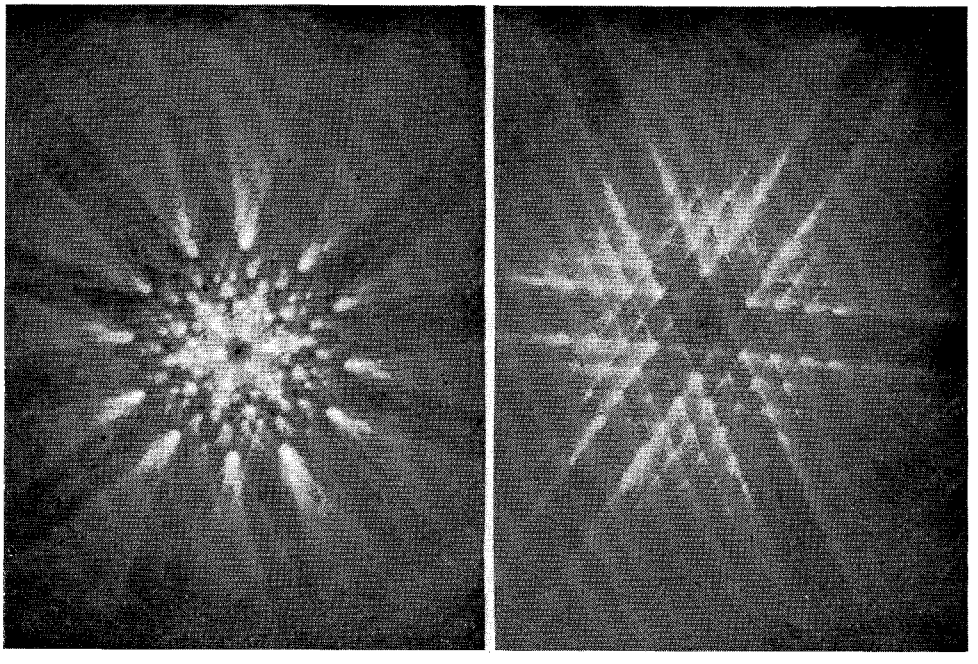

(*a*) (*b*)

Kikuchi bands in (*a*) 2H and (*b*) 3R–MoS_2. (Uyeda 1968—200 kv, $t \sim 1{\cdot}2\,\mu$.)

trigonal 3-planar star, HfS_2 gives an hexagonal type pattern, whilst 2H–$MoSe_2$ gives the trigonal pattern like 3R–$MoSe_2$. Though many of our transport crystals were of the 3R type it seems that the 2H form is the stable one to 1000°C. The group VI 3R forms have been synthesized in *powder* form only at high pressure and temperature (Towle *et al.* 1966, Silverman 1967). Such synthesis of the 3R form from the *elements* is much easier than conversion through of the 2H powdered *compound*. 3R–WSe_2 seems very difficult to obtain in pure form, whilst $MoTe_2$ always occurs in the β form at high temperatures and pressures (Revolinsky and Beerntsen 1966). Several transport crystals were obtained for which both 2H and 3R lines appeared in the x-ray pattern. These stacking mixtures gave exciton peaks intermediate between the extreme positions of 2H and 3R, and at least at 77°K there was no indication of any division of the B peak (see p. 246).

The group V stacking polytypes are also known to show an interesting difference of degree, namely their superconducting transition temperatures. Figure 17 gives the x-ray powder lines expected from six polytypes of $TaSe_2$. Some experimental results are shown in fig. 18. It is seen that the line intensities are not consistent: this is due most likely to the impossibility of powdering such flexible crystals. In fig. 19 is given a selection of electron

Fig. 17

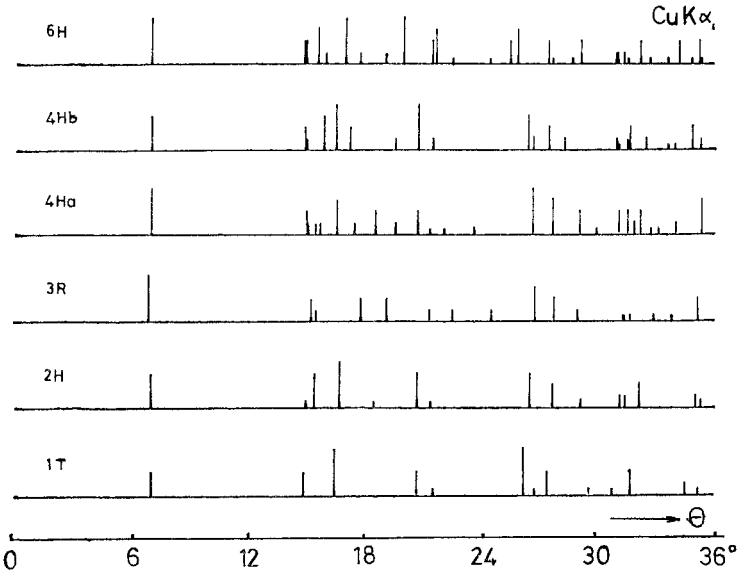

X-ray powder pattern lines for the polytypes of $TaSe_2$. (Constructed from Bjerkelund and Kjekshus 1967.)

microscope diffraction patterns. It is seen that the majority match the structures discussed earlier. However, the 1T–TaS_2 pattern is at variance with its x-ray pattern, unlike VSe_2 and $TaTe_2$. Both electron and x-ray patterns are simple for VSe_2 (like HfS_2); *both* are complex for $TaTe_2$ (like WTe_2). This problem is returned to on p. 297. Bright-field electron micrographs are given in fig. 20. The fluid dislocations and hexagonal networks found in the regular materials have been discussed by Amelinckx (1964). Ribboning is observed in the distorted structures like $ReSe_2$. As seen the 1T–TaS_2 picture appears simpler. The most complex pictures are obtained with $TaTe_2$ and particularly $NbTe_2$. 'Domains' are found throughout the crystal and this can result in complex compounded diffraction patterns. It is just possible that these domains invalidate the structure determined by Brown 1966. Kjekshus' Oslo group certainly failed to confirm Brown's result (Selte *et al.* 1966). Many of these points are returned to in detail in § 8.

Mixed crystals of the types $(W/Ta)Se_2$ and $(W/Mo)Se_2$ have been prepared and the micrographs show no indication of segregation. Brixner found smooth parameter and property changes right through these systems (Brixner 1963). The group VI materials, however, will substitute surprisingly little group VII metal (e.g. $(Mo/Re)Se_2 \lesssim 2\%$Re–Hicks 1964). Similarly 1T–TaS_2 does not seem to incorporate Hf readily, at least when using the vapour transport process. Such mixed crystals can be satisfactorily analysed to 2% by electron-probe x-ray microanalysis. The composition varies from crystal to crystal, depending on its position of growth in the reaction tube.

Fig. 18

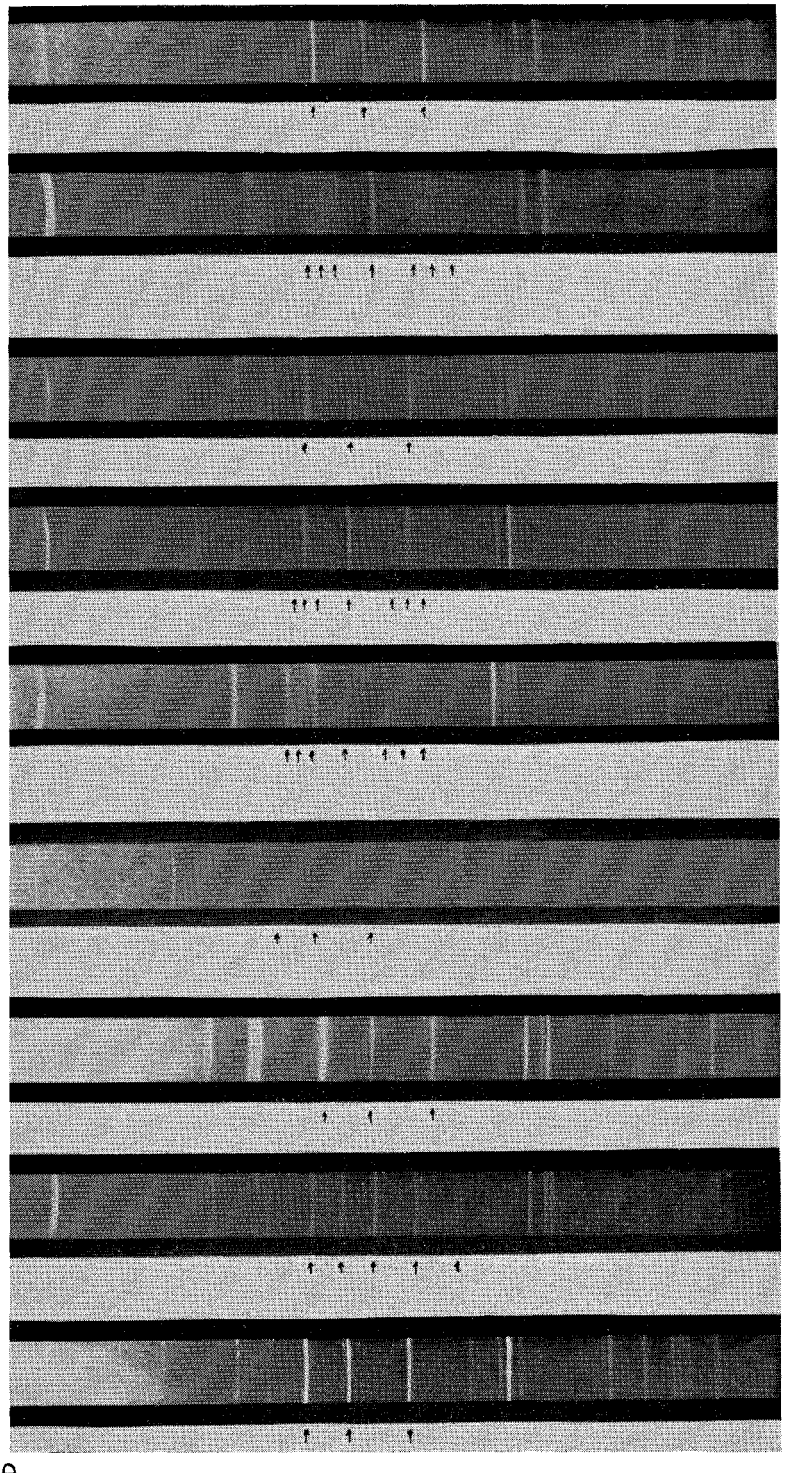

MoS_2
(*a*) Natural powdered—2H

(*b*) Transport crystal (750°C)—3R+2H

$MoSe_2$
(*a*) High temp. transport crystal (900°C)—2H

(*b*) Transport crystal (750°C)—2H with trace of 3R

(*c*) Towle's H.Pr. product—3R+2H

α-$MoTe_2$
(*a*) Transport crystal (750°C)—2H

WS_2
(*a*) Powder synthesis—2H

(*b*) Silverman's H.Pr. product—3R

WSe_2
(*a*) Transport crystal (950°C)—2H

X-ray powder photographs (Cu Kα, $\lambda = 1{\cdot}54$ Å).

Fig. 18 (*continued*)

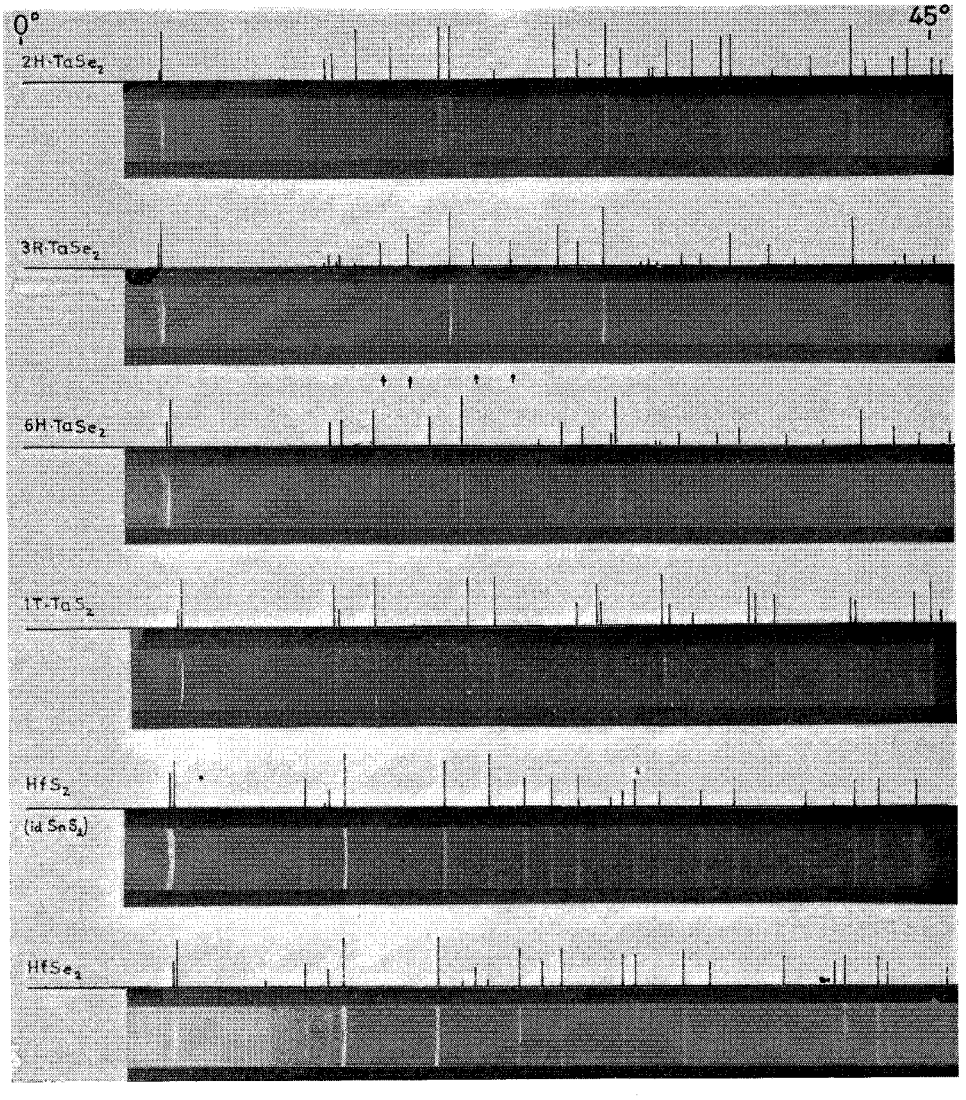

X-ray powder photographs (Cu Kα, $\lambda = 1{\cdot}54$ Å).

Fig. 19

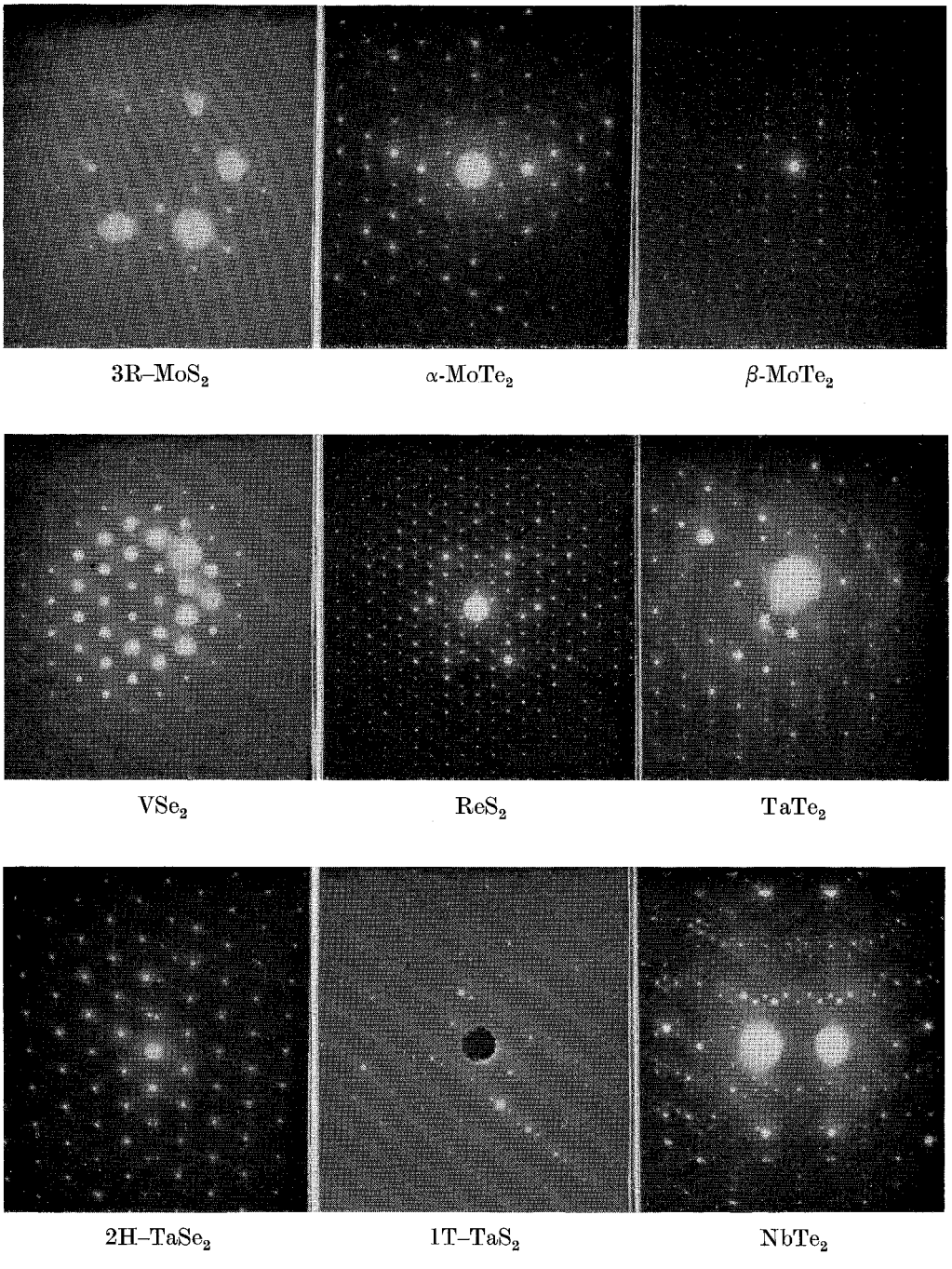

Electron microscope diffraction patterns.

Fig. 20

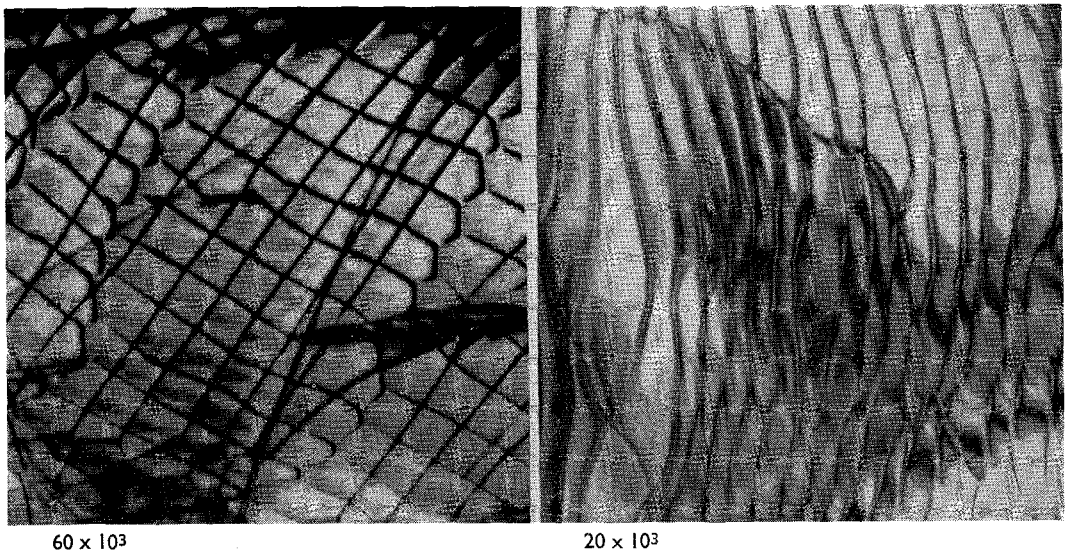

60 x 10³ 20 x 10³

α-$MoTe_2$ $NbSe_2$

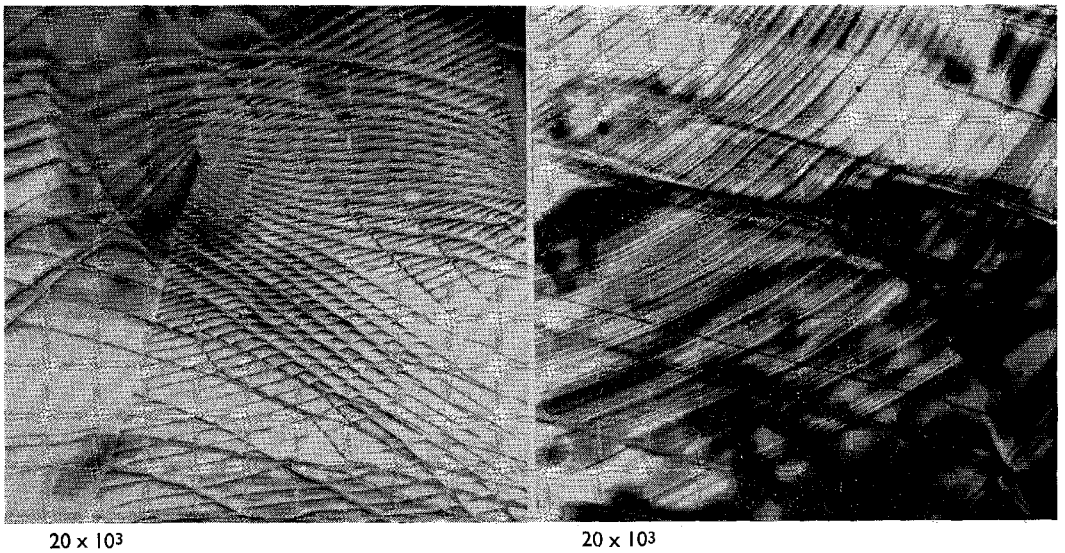

20 x 10³ 20 x 10³

1T–TaS_2 $ReSe_2$

Bright-field dislocation arrays.

Fig. 21

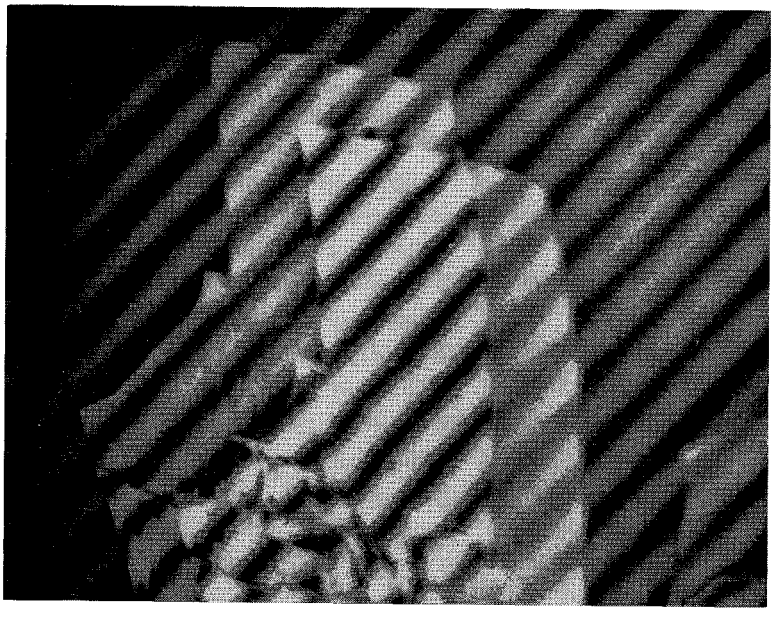

(*a*)

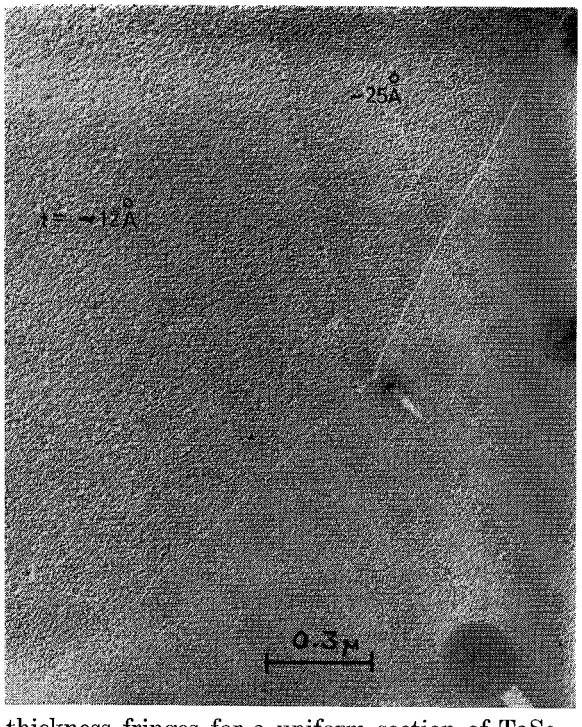

(*b*)

(*a*) Nomarski thickness fringes for a uniform section of $TaSe_2$. (The crystal is about 1 mm wide and the fringe shift of 21% corresponds to $t = 630$ Å.) (*b*) Electron micrograph of a cleaved specimen of MoS_2 only one and two unit cells thick, measured by the carbon shadowing technique. (By Frindt 1966.)

§ 4. Transmission Spectra for the Layer-type Transition Metal Dichalcogenides

The crystal specimens used for the optical transmission work are obtained by repeated cleaving on sellotape. The very thin cleaved sections can be transferred from the tape to a glass or quartz substrate using trichloroethylene as solvent. Details of this and other experimental techniques are given elsewhere (Wilson, J. A., 1969). Specimens only 500 Å thick can readily be mounted, and may then be used for electrical (Wieting 1968, see p. 271) as well as optical measurements. Crystal thicknesses have been measured using the Nomarski polarizing technique. As seen in fig. 21 (*a*) quite large areas $\sim 200\,\mu$ square cleave at the same thickness. Most of the layer dichalcogenides are strongly coloured in transmission, and the colour changes rapidly with thickness in a characteristic way from material to material. The crystals are highly reflecting also, and even in the high transmission range about 20% reflection occurs, since the refractive index is still $\sim 2{\cdot}7$.

The micro-optical work was carried out on a split-beam spectrophotometer over the range $\frac{1}{2}$ to $5\frac{1}{2}$ ev ($2\,\mu$ to 2200 Å), at both room and liquid air temperatures. Experimental details are again given in the above reference, together with an assessment of spectral quality; the peak positions are also detailed there.

In drawing the following spectra all materials have constantly been referred back to MoS_2, for which a proper analysis of the absorption and reflection measurements has been made in deriving absorption coefficient values (Evans and Young 1965). The spectra as presented below are with the y axis varying approximately as log α (see fig. 22 *a*).

The spectra have been divided into the following groupings, the full significance of which will become apparent later:

A. Regular group VI
   MoS_2, $MoSe_2$, α-$MoTe_2$, WS_2, WSe_2.
B. Distorted group VI
   β-$MoTe_2$, WTe_2.
C. Regular group V
   NbS_2, $NbSe_2$, $TaSe_2$, VSe_2.
D. Distorted group V
   $NbTe_2$, $TaTe_2$, 1T–TaS_2.
E. Group VII
   TcS_2, $TcSe_2$, ReS_2, $ReSe_2$.
F. Group IV
   ZrS_2, $ZrSe_2$, HfS_2, $HfSe_2$, $TiSe_2$.

Several other large families of layer compounds exist in addition to the above dichalcogenides. Among transition metal compounds there are many layer dihalides and trihalides (e.g. $FeCl_2$, $CrBr_3$); also the divalent hydroxides (e.g. $Mn(OH)_2$). Among non-transition metal compounds layer structures are found in the dihalides of groups IIA, IIB and IVA

Fig. 22

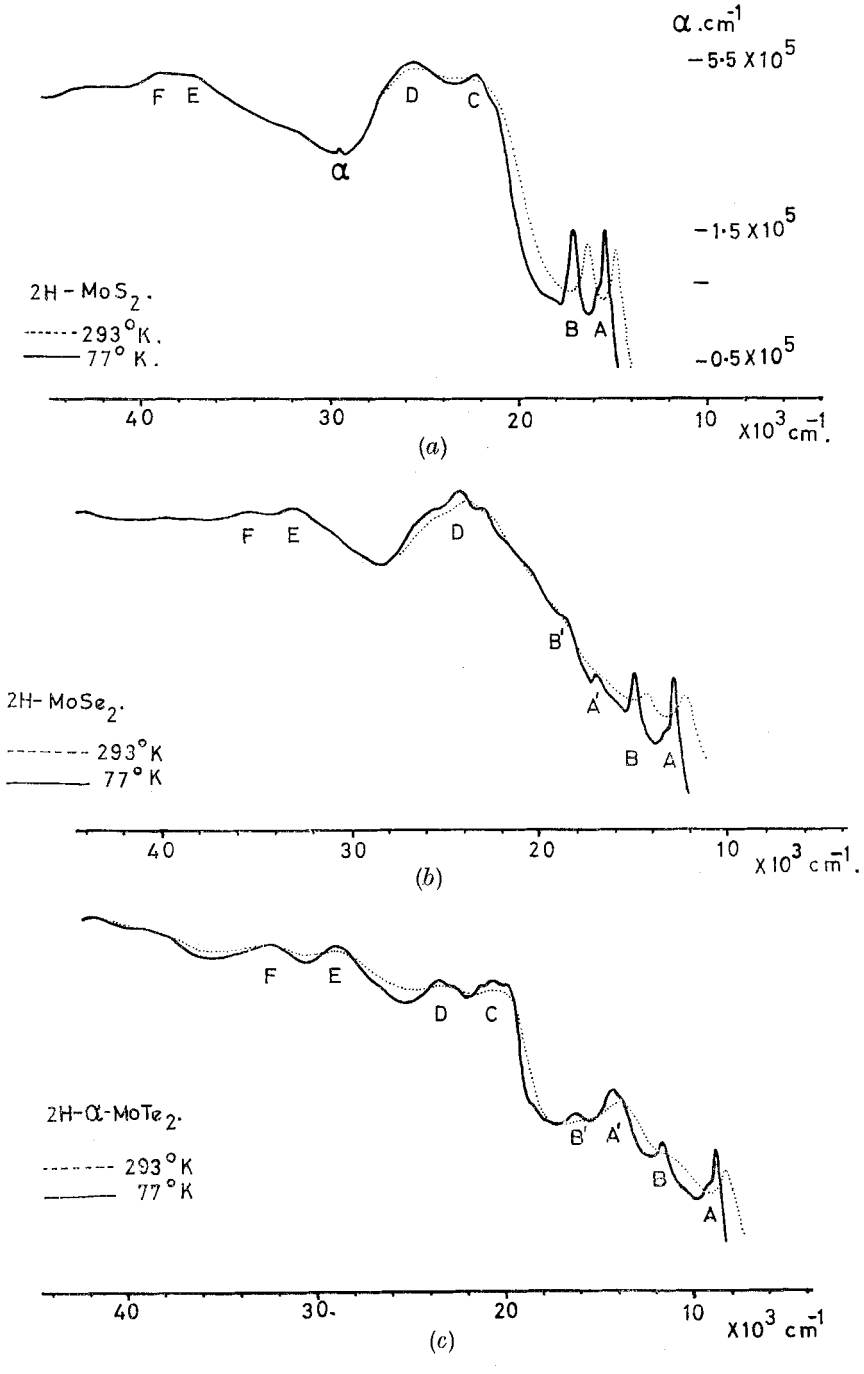

Transmission spectra for the transition metal dichalcogenides.

Fig. 22 (*continued*)

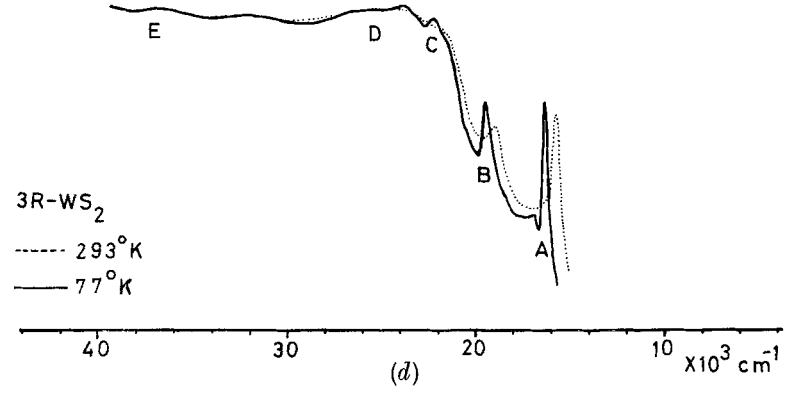

(*d*)

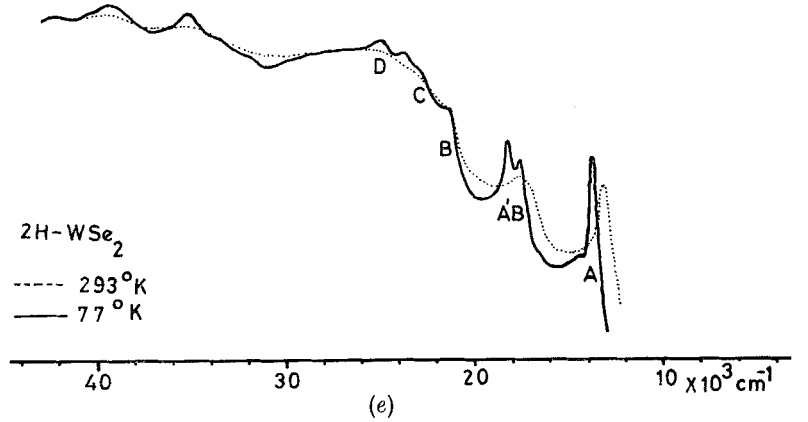

(*e*)

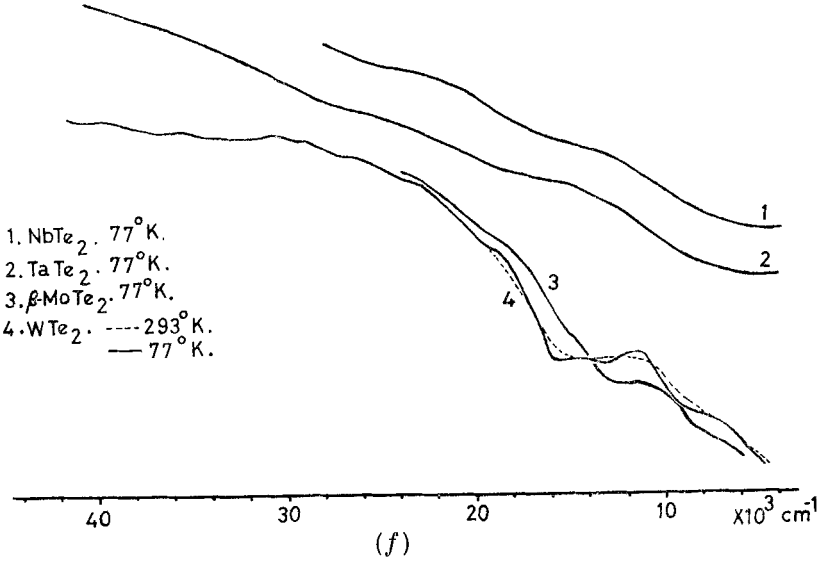

(*f*)

Fig. 22 (*continued*)

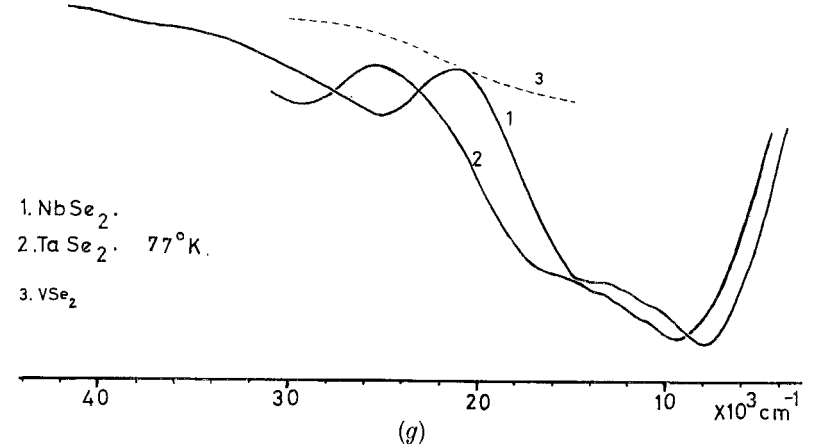

(*g*)

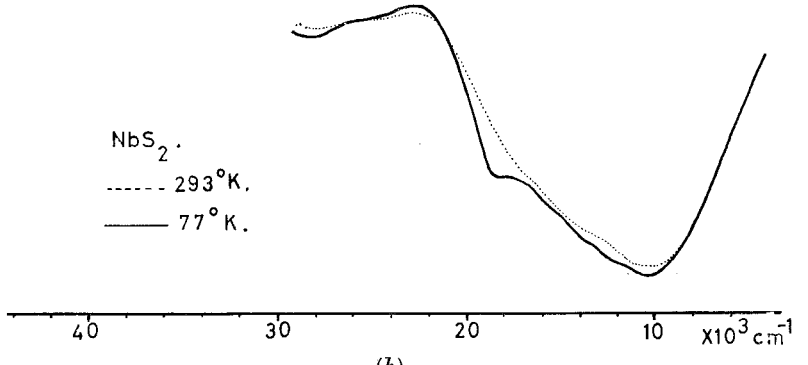

(*h*)

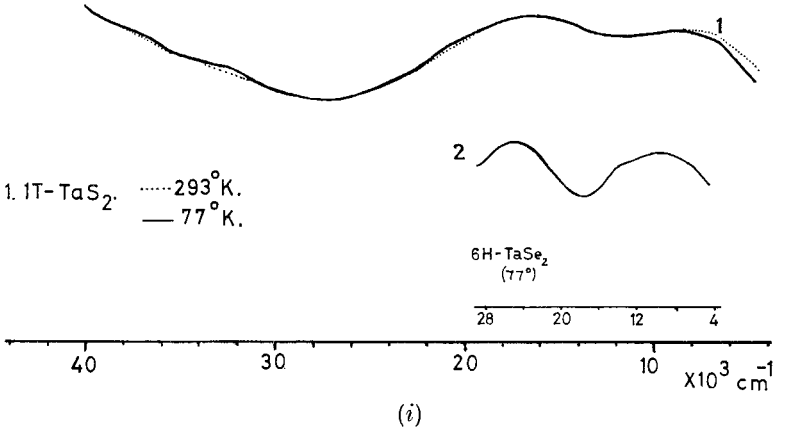

(*i*)

Fig. 22 (*continued*)

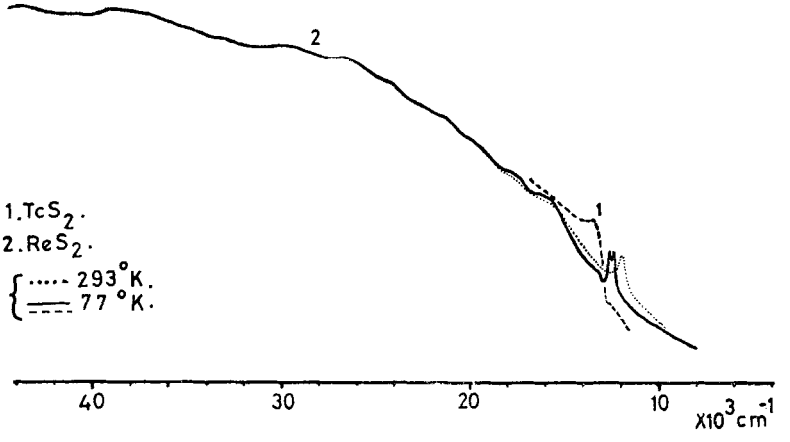

(*j*)

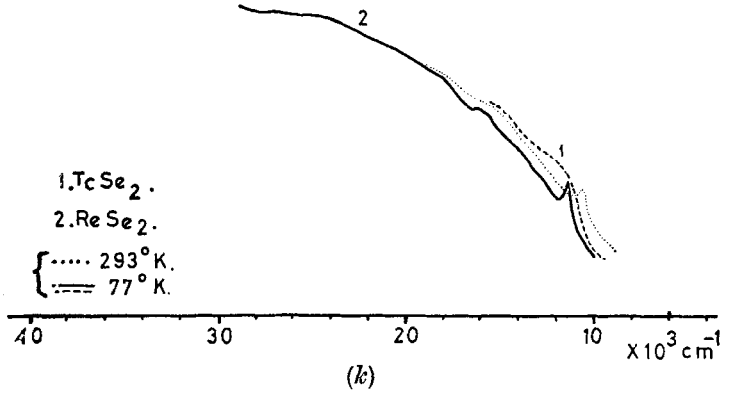

(*k*)

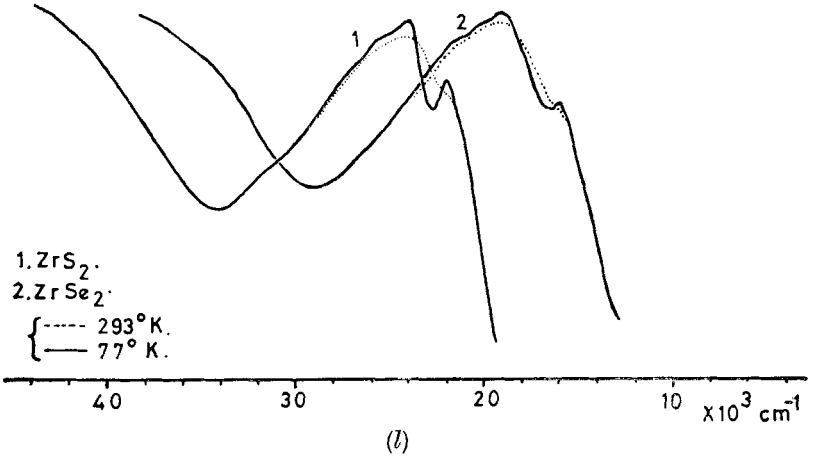

(*l*)

Fig. 22 (*continued*)

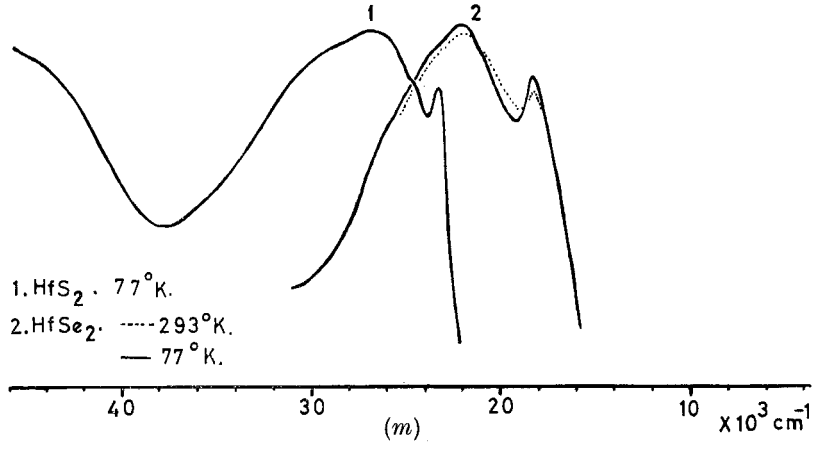

(*m*)

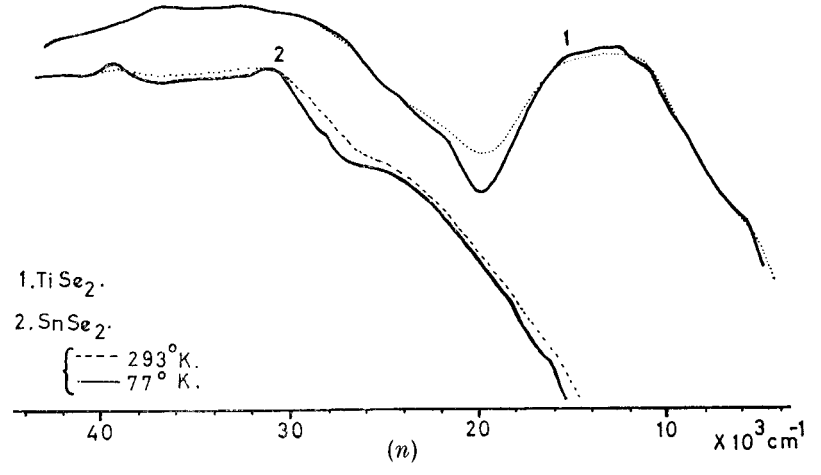

(*n*)

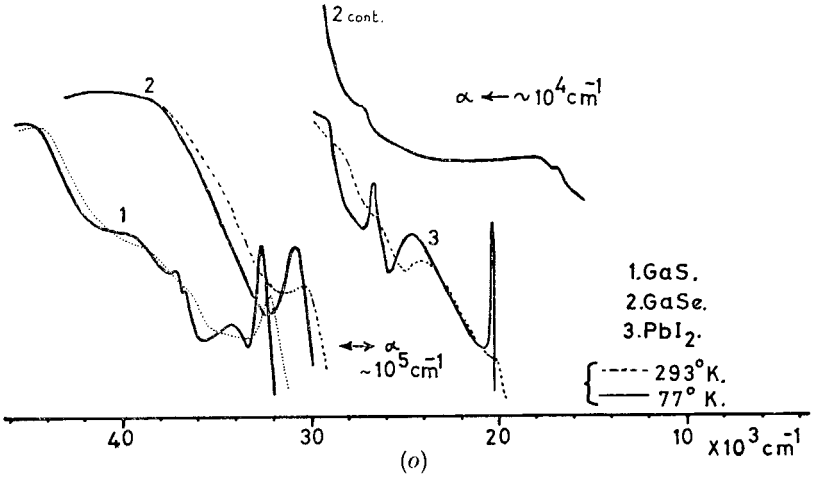

(*o*)

Fig. 22 (*continued*)

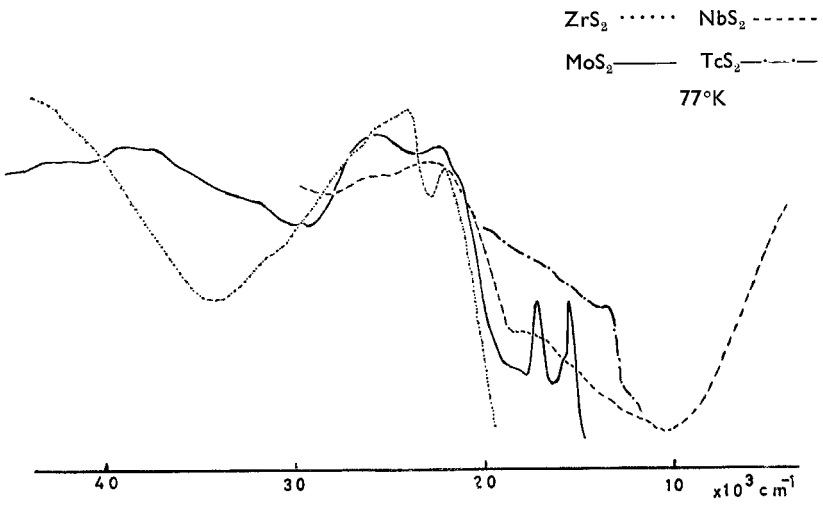

(*p*)

(e.g. CaI_2, CdI_2, PbI_2), the tri-iodides of group VA (e.g. BiI_3), some dichalcogenides of group IVA (e.g. SnS_2), and also the more unusual GaS and Bi_2Te_3 families. The transition metal halides are dealt with in detail in § 9.3. Energy gaps are given below for some of the non-transition metal layer compounds. Several points of contact have been made between these latter materials and the layer-type transition metal dichalcogenides, viz.

(*a*) Excitons—GaS, PbI_2, BiI_3, CdI_2—with MoS_2 (see §§ 6.1.2. and 7.2.2).

(*b*) Defects and polytypism—GaS, PbI_2—with MoS_2 (see §§ 6.1.2 and7.2.2).

(*c*) Indirect edge—GaS, CdI_2, SnS_2—with MoS_2, ZrS_2 (see § 6.1).

(*d*) Banding/bonding—SnS_2 versus ZrS_2, GaS versus MoS_2 (see § 5.2).

(*e*) Anisotropic electrical data related to band structure—Bi_2Te_3 (see § 7.2).

Period 3	Period 4	Period 5	Period 6	Group	Metal atom configuration
	CaI_2	SrI_2	YbI_2	IIA	$s^2(d^0)$
$MgCl_2/Br_2I_2$	$ZnCl_2/Br_2/I_2$	$CdCl_2Br_2/I_2$	—	IIB	$(d^{10})s^2$
	GeI_2	SnI_2	PbI_2	IV	$(s^2)p^2$
	GaS/Se/Te	InSe		IIIA	$s^2p \times 2$
$SiTe_2$	$GeSe_2$	SnS_2/Se_2	α-PbS_2/Se_2	IVA	s^2p^2
	(As_2S_3/Se_3)	Sb_2Te_3	Bi_2Se_3/Te_3	VB	$(s^2)p^3$
	AsI_3	SbI_3	BiI_3	VB	$(s^2)p^3$

Fig. 23

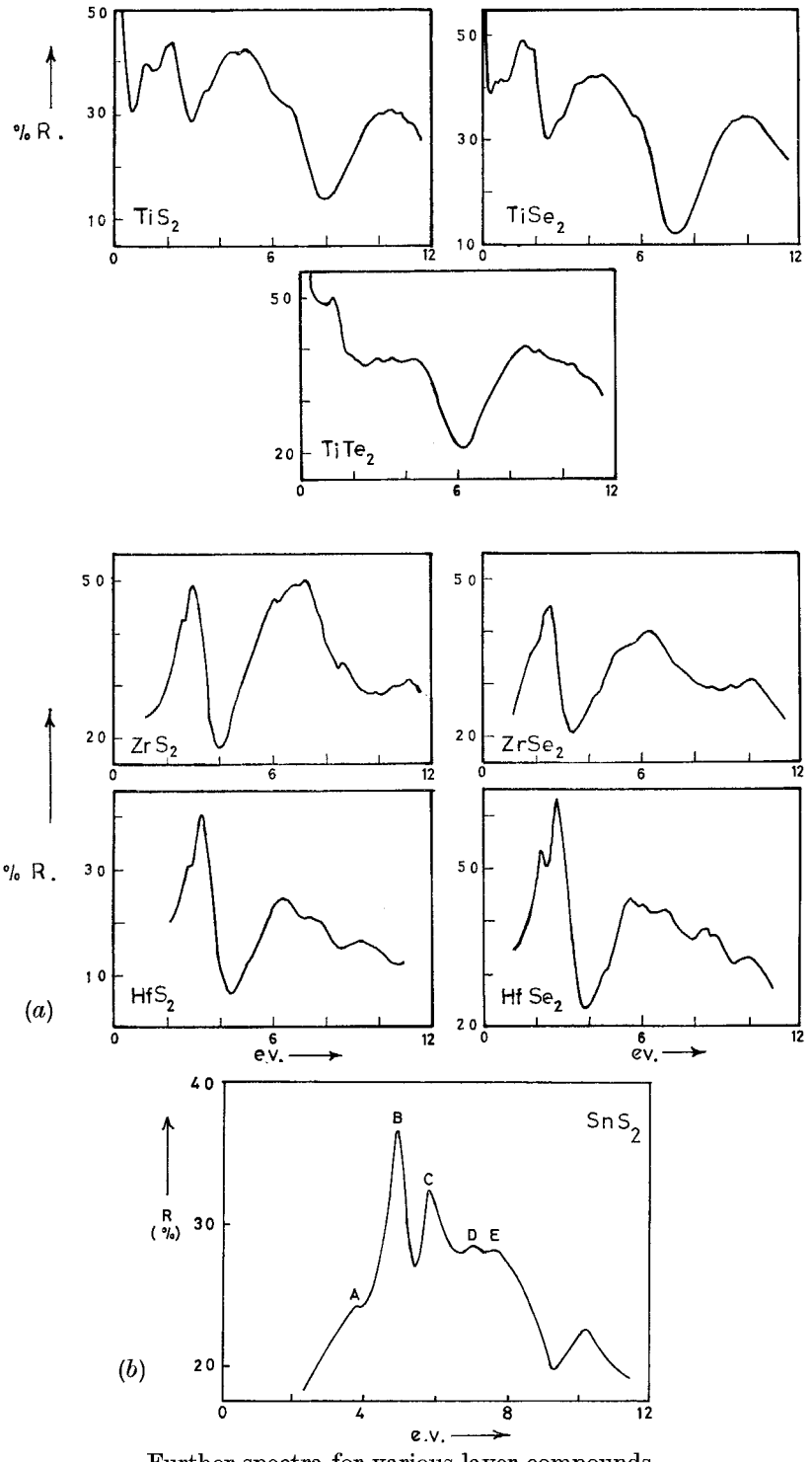

Further spectra for various layer compounds.

Fig. 23 (*continued*)

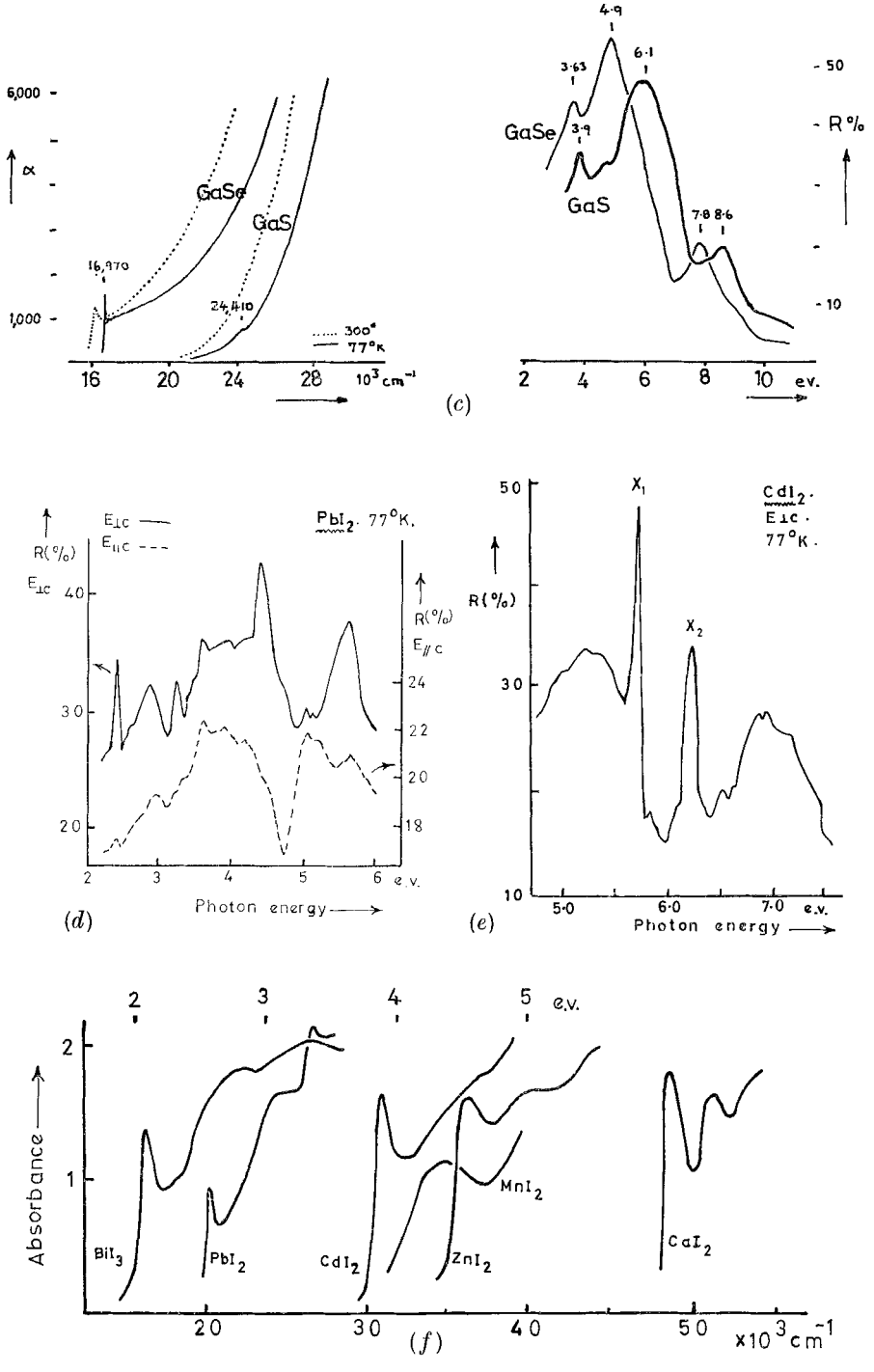

(*a*) and (*b*) from Greenaway and Nitsche 1965, (*c*) Bassani *et al.* 1964, (*d*) and (*e*) from Greenaway and Harbeke 1966, (*f*) Tubbs 1968.

Optical band gaps, 77°K:

	ev								
CaI_2	5·8	(a)	$SiTe_2$	1·85	(d)	AsI_3	~ 2·5	(i)	GaS	3·0	(m)
ZnI_2	4·4	(a)	$GeSe_2$	2·35	(e)	SbI_3	2·0	(a)	GaSe	2·1	(m)
CdI_2	3·3	(a), (b), (c)	SnS_2	2·2	(c), (f)	BiI_3	1·7	(j)	GaTe	1·75	(n)
PbI_2	2·5	(a), (b)	$SnSe_2$	1·1	(f), (g)	Bi_2Se_3	0·16	(k), (l)	InSe	1·3	(o)
			α-PbS_2	~1	(h)	Bi_2Te_3	0·14	(l)	Ag_2F	super-conducting metal	(p)

References: (a) Tubbs (1968); (b) Greenaway and Harbeke (1966); (c) Greenaway and Nitsche (1965); (d) Rau and Kannewuf (1966); (e) Asanabe (1961); (f) Domingo *et al.* (1966); (g) Busch *et al.* (1961); (h) Silverman (1966); (i) Evans, B. L. (private communication); (j) Evans (1966); (k) Gobrecht *et al.* (1966); (l) Greenaway and Harbeke (1965); (m) Bassani *et al.* (1964); (n) Brebner and Fischer (1962); (o) Andriyashik *et al.* (1968); (p) Andres *et al.* (1966).

Mentioned in the above is one of the very few 'anti-structure' CdI_2-type materials, Ag_2F. Hf_2S and Hf_2Se have anti-type MoS_2 structures, and are again metallic (see Franzen *et al.* 1967). Layer structures occasionally occur in the transactinides, e.g. USe_2 (Khodadad 1961), ThI_2 (Guggenberger and Jacobson 1968), and also in the rare earths, e.g. $GdCl_3/Br_3(f^7)$ (Varsanyi *et al.* 1969). In ThI_2 there is an alternating stacking of octahedral and trigonal prism sandwiches, similar to 6H–$TaSe_2$. The uranium systems are complex and resemble those of thorium and group IV, rather than group VI. USe_3 and $ThSe_3$ both have the linear stack structure of $ZrSe_3$, mentioned in § 9.3.

§ 5. The Approach towards a Band Scheme for the Layer-type Transition Metal Dichalcogenides

5.1. *General Discussion of Band Formation in Transition Metal Compounds*

A major problem in discussing transition metal materials is what happens to the metal d states when a compound is formed and a crystal structure built up. The various compounds of nickel or manganese illustrate clearly the gradation from completely localized d states, through various degrees of incipient band formation, to complete delocalization in a wide band. The properties most clearly to show this change are the magnetic susceptibility and the ligand field spectrum. The value of μ_{eff} falls off from the local spin value down through to Pauli-type metallic paramagnetism. At the same time the ligand field intra-atomic d–d transitions lose definition, move to smaller energies and gain rapidly in intensity before being incorporated into stronger inter-band transitions (see § 9.3).

It is not yet clear whether band formation occurs continuously as the relevant conditions are changed (viz. d–d intercore overlap), or whether the process suffers some discontinuous cooperative change. It is thought that inter-site electron correlation interactions may favour the latter process, and

Table 8. Growth of covalency in the divalent compounds of manganese and nickel

(*a*) Magnetic properties of divalent nickel

	$NiCl_2$	$NiBr_2$	NiI_2	NiO	NiS_2	α-NiS	$NiSe_2$	$NiTe_2$	
χ_{Molar}	6150	5600	3900	660	700	240	170	80	$\times 10^{-6}$
Θ_{Para} °K	+70°	−18°	—	~ −2500°	~ −750°	—	—	—	
$T_{Néel}$ °K	50°*	60°*	75°*	520°	—	(263°)	—	—	

*For a discussion of these values see van Uitert, Williams, Sherwood and Rubin, 1965, *J. appl. Phys.*, **36**, 1029.

(*b*) Optical properties of divalent manganese

	MnF_2	$MnSO_4.4H_2O$	$MnCO_3$	MnO	$MnCl_2$	$MnBr_2$	MnI_2	α-MnS	
Position of $^6A_{1g} \rightarrow {}^4A_{1g}$	25200	24880	24540	23920	23360	22980	21900	21500	cm^{-1}
Oscillator strength	Very low	0·6	7·7	—	7·3	9	12·1	230	$\times 10^{-7}$

(See Lohr and McClure 1968 and Huffman 1969.)

that the d band prior to its full establishment is pinched off into a series of non-conducting (i.e. full) sub-bands (see No. 4, **40,** *Rev. mod. Phys.*, October 1968). At present we are studying the high pressure optical properties of several promising layer compounds from this aspect of the Mott 'metal/insulator transition', viz. NiI_2, VI_2, TiI_2, CrI_3 and $TiCl_3$.

Returning to the layer-type transition metal dichalcogenides it is clear that d band formation is there well advanced. The semiconductors of groups IV (e.g. ZrS_2), VI (MoS_2) and VIII (PtS_2) are all *dia*magnetic, whilst the spectra in the 1 ev range are not of the ligand-field type, since the absorption coefficients are in excess of $10^5\,cm^{-1}$. The degree of filling of d bands lying within the basic bonding–antibonding band gap (~ 4 ev in MoS_2) largely determines the electrical character of the various compounds. For example the trigonal prism group V materials (d^3) are medium mobility metals ($\rho \sim 3 \times 10^{-4}\,\Omega$-cm), superconducting, and with the plasma edge at about 1 ev.

Among the *pyrite* dichalcogenides, however, such d bands are not always formed. Thus, although $RhSe_2$ (d^7) and $CuSe_2$ (d^9) are metallic and show Pauli paramagnetism, superconductivity and strong free carrier absorption, the manganese materials (d^5), and NiS_2, still have local spin moments, which in the case of the manganese compounds become cooperatively aligned to yield antiferromagnetic ordering around liquid air temperature. This antiferromagnetism should be distinguished from the band antiferromagnetism shown by the $NbSe_2$ family; the latter is concurrent with free carrier absorption (see § 7.3.1). FeS_2 and CoS_2 have magnetic, electrical and optical properties which indicate that a collective narrow d band is achieved. The non-layered transition metal dichalcogenides are discussed in detail in § 9.1.

Several factors affect this question of d band formation:

(i) internuclear distances, T–X, T–T and X–X (size factor),

(ii) crystal structure (symmetry factor),

(iii) (*a*) ligand electronegativity (energy factor),

(*b*) detailed electronic configuration of metal atom.

These factors are of course inter-related. The extent to which the s and d states of the metal atom can become spatially and energetically distinct is most pronounced for manganese. Compounds like MnI_2, MnO, α-MnS and MnS_2 are all based on the Mn^{2+} *ion* with its contracted d^5 half-shell. They tend to have large interatomic distances in contrast to non-ionic compounds like Ni_2Sn, MnTe and MnSb, where the ligand is not sufficiently electronegative to cause s–d differentiation (collected parameters, Slater 1965, p. 308ff). *Hybridization* of the metal atom s and d states and general

'*covalent*' mixing of these states into the valence bands, is more common for the early groups of the transition periods, and, again, more so for all groups of the second and third periods than for the first period:

thus we find the decrease in ionicity of $TiCl_3$ compared with $CrCl_3$,
and of TiO ,, ,, NiO,
whilst there is an increase in ionicity for $TiCl_2$,, ,, $ZrCl_2$,
for MnS_2 ,, ,, TcS_2,
for NiO ,, ,, PdO.

(many of these compounds are discussed further in § 9).

Orbital hybridization and the resulting covalency means that in the *crystalline* state we are going to have bands of highly mixed 'l' character, which are of greater energy span than for ionic compounds, where the valence bands are very flat. In the *dichalcogenides* of groups IV, V, VI a significant degree of d and p covalent mixing into the valence band along with the metal s state seems feasible. In crystals of the transition *elements* themselves s, d, p mixing is well advanced (e.g. Ti, Altmann and Bradley 1967). When the distance between metal atoms is increased, as in a compound, this direct metal sublattice mixing decreases rapidly, particularly for the elements to the centre right of each series where the atomic radii are small. The metal–metal distances in the above dichalcogenides, with extremes of 3·16 Å for MoS_2 and 3·95 Å for $ZrTe_2$, correspond to 15% to 25% increases on those distances in the pure metals. In all the *dihalides* these percentage increases are much greater, e.g. 42% for TiI_2 ($a = 4{\cdot}11$ Å), 65% for MnI_2 ($a = 4{\cdot}10$ Å). This general size factor difference plus the electronegativity change means that there will be far greater isolation, energetically and spatially, of the d-states in say $ZrCl_2$ than in its isostructural isoelectronic partner MoS_2†. The layer halides are discussed further in § 9.3.

5.2. *The Proposed Banding Arrays for the Layer-type Transition Metal Dichalcogenides*

The effect on the general band scheme for transition metal compounds of the move from ionic to covalent bonding is represented in fig. 24. With covalent bonding the valence band is considerably broader due to T/X state mixing. Au Yang and Cohen's (1969) band diagram for $SnSe_2$ (C6, $E_g = 1$ ev) shows this markedly as compared with the isoelectronic isostructural but ionic case for $CdBr_2$ ($E_g \approx 4$ ev; compare RbBr $E_g \sim 6{\cdot}5$ ev, and AgBr $E_g \sim 3$ ev). In a transition metal compound like ZrS_2 or MoS_2 it is likely that this mixing of metal states into the valence band follows the

† N.B. The above type of orbital differentiation is not completely confined to transition elements; note s/p compounds like TlBr, SnTe and PbI_2, (also the concomitant long bond lengths, cf. $MnCl_2$, CoO, etc.). A recent attempt at assigning percentage ionic character to non-transition metal compounds has been made by Phillips and van Vechten (1969).

pattern $s > d \gg p$. The p states are more likely to be mixed into the energetically closer non-bonding d bands, interposed within the basic $\sigma\sigma^*$ gap†. The averaged value of this latter gap is directly related to the heat of formation of the compound, a measure of the chemical binding energy which is often known (Vijh 1969).

Fig. 24

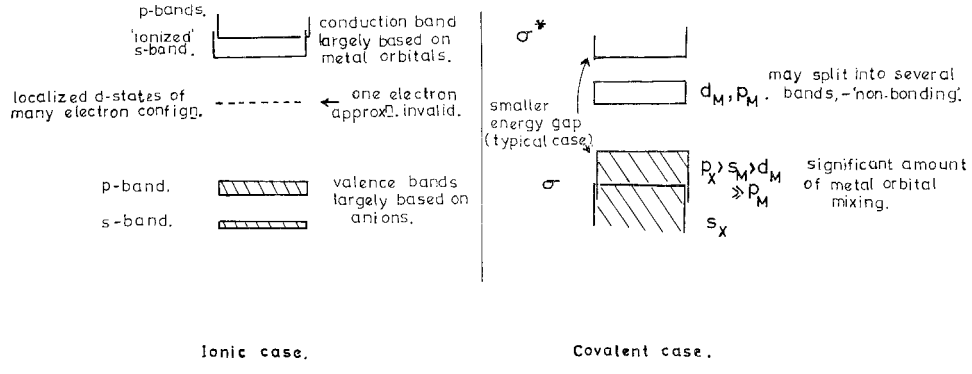

The change in banding character between ' ionic ' and ' covalent ' transition metal compounds.

In an octahedrally coordinated compound (e.g. ZrS_2) it is well known that out of the five d states the two e_g states are more suited geometrically to covalent bonding than are the three t_{2g} states. The latter go to form the basis of a non-bonding band. In a structure with trigonal prism coordination like MoS_2 (point group D_{3h}) the d states split in such a way that the d_{yz} and d_{xz} orbitals are the most likely to mix into the valence band. The $d_{x^2-y^2}$ and d_{xy} orbitals will mix more with the metal p_x and p_y states, and are likely to form a non-bonding band above and detached from a second non-bonding band based on d_{z^2}. This latter orbital gives poor overlap between near-neighbour metal atoms and the band is likely to be rather narrow.

As indicated below in fig. 26 the principal valence band in the TX_2 layer structures is full with 16 electrons (e.g. ZrS_2), and subsequent electron additions as for NbS_2, MoS_2, TcS_2 go into the non-bonding d-based bands. It is the degree of filling of these latter bands that then determines the electrical, magnetic and optical properties of these transition metal

† An attempt is being made in this laboratory to calculate the band structures using the tight-binding method by R. A. Bromley.

dichalcogenides. The details will be discussed shortly in §§ 6 and 7†.

The possible shape and orientation of the non-bonding orbitals for the TX_2 layer structures is shown in fig. 25. If our interpretation of the spectra is correct (see shortly) the widths and location of the non-bonding bands are as marked on fig. 26 (*b*). Interpretation to this end of the optical results is prompted by the very satisfactory viewpoint that the above

Fig. 25

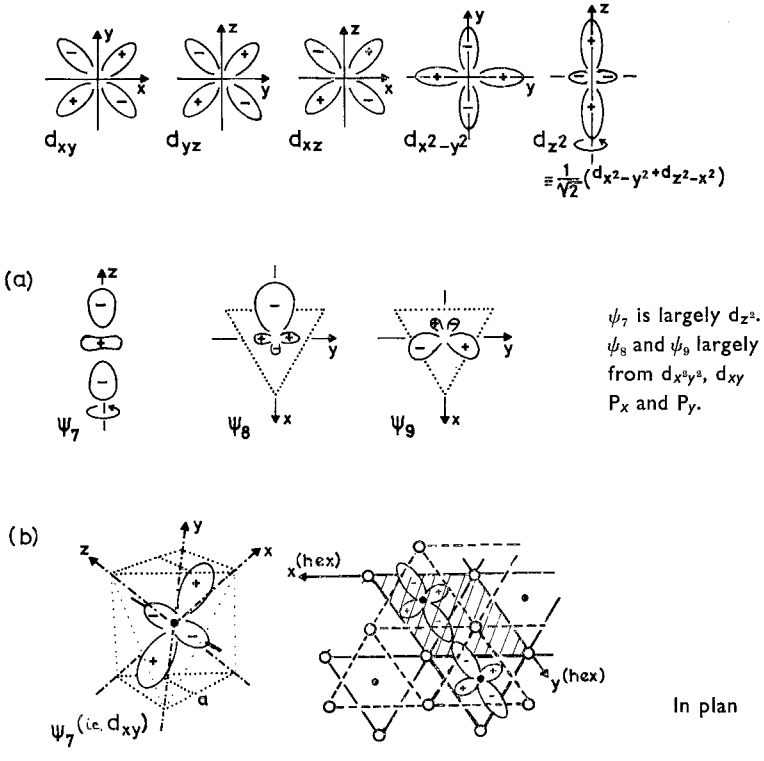

Shape and orientation of the 'non-bonding' orbitals for the TX_2 layer structures (based largely on metal d and p states). (*a*) For trigonal prism, ψ_7 yields poor M–M overlap, ψ_8 and ψ_9 degenerate, (*b*) for octahedron, ψ_7, ψ_8, ψ_9 degenerate. Lobes bisect bond angles. Good overlap in layers.

† It is hoped from the above discussion we have made clear that in, say, $ZrSe_2$, the zirconium 5p states will be virtually confined to the conduction band. Likewise in $SnSe_2$ the tin 5d states will show negligible mixing into the valence band (i.e. as occupied states). The mixing here of p and d states respectively into the valence band is proportionately much less than would be implied from the use of six equivalent metal hybrid bonding functions, of the old octahedral formulation, 'sp^3d^2'. The same goes for trigonal prismatic coordination, for which the formulation 'd^4sp', derived from Hultgren's paper of 1932, is often seen.

banding schemes give of the observed electrical, magnetic and structural properties for the whole TX_2 dichalcogenide family†.

Fig. 26

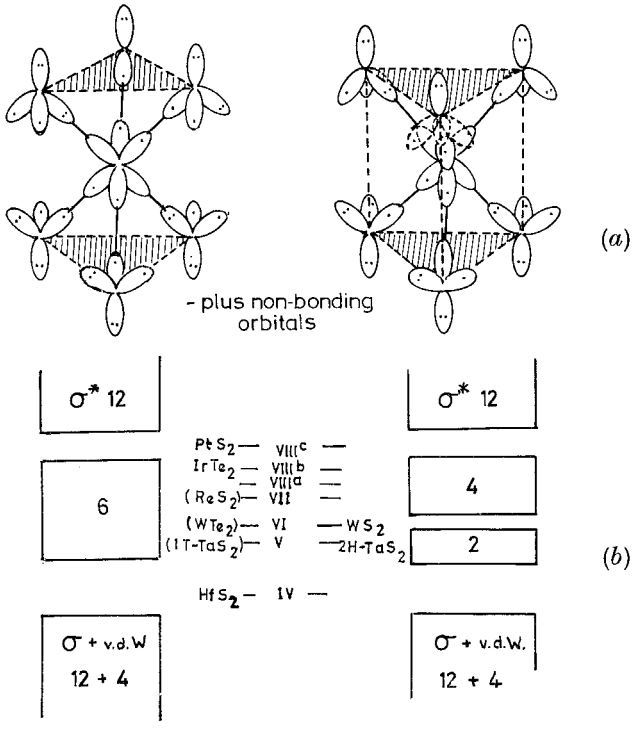

(*a*) Occupation of orbitals in the simple valence bond picture, (*b*) the proposed band positions and their degree of filling for the regular TX_2 dichalcogenides.

Figure 26 (*a*) stylistically represents the arrangement of electrons in the bonded directions for the two types of layer dichalcogenide TX_2 sandwich. As seen, a simple valence bond picture requires not only hybridization but also 'resonance'. Each chalcogenide atom puts a lone pair into the van der Waals region, and each metal atom then needs to supply four electrons for the bonding states to be completely full (e.g. as in ZrS_2 $s^2 d^2$, or SnS_2 $s^2 p^2$). Any further electrons (as in MoS_2, $s^2 d^4$) must enter the non-bonding orbitals which can accommodate up to six electrons (as in PtS_2, $s^2 d^8$). The semiconductivity of octahedral ZrS_2 and PtS_2 follows automatically, whilst that of the MoS_2 family is seen to be a consequence of the adoption of the trigonal prismatic structure. In group V we have metals

† Goodenough has recently published two papers (1968 b, c) discussing the behaviour of the d levels in MoS_2 and WS_2 from the aspect of crystal field theory. However, the model seems to be too ionic in character and fails to match much of the experimental data.

for both coordination types, VSe_2 with the wider octahedral band being a 'better' metal than say $NbSe_2$, where the free carriers lie in the narrow d_{z^2} band of the trigonal prism scheme. We will look at the electrical properties in some detail group by group in § 7.

§ 6. The Optical Spectra of the *Regular* Layered TX_2 Dichalcogenides Related to the above Banding Scheme

6.1. *The Trigonal Prism Materials*

6.1.1. *Band positions and transition assignments*

Because the non-bonding d band system in the MoS_2 family is only partially filled, and again because the materials are semiconductors, the group VI spectra are quite complicated. Figure 27 shows the five basic types of inter-band transition to be expected with the trigonal prism set of bands. Transition V is the basic bonding energy gap. Such transitions commence in MoS_2 with exciton α. Transition III is the one which gives rise to the strong excitons A and B characteristic of the MoS_2 family; transitions IV, of somewhat larger energy, yield the broad band topped by peaks C and D. This ordering is seen to be the correct one from a comparison with the group V spectra. There the D transition is absent due to the d_{z^2} band now being only half full. Furthermore, group V loses the excitons A, B and α which are screened out by the free carriers of the d_{z^2} band. A broad hump remains in the A/B region. In group V there is the opportunity also for transitions of type II. These also show up weakly

Fig. 27

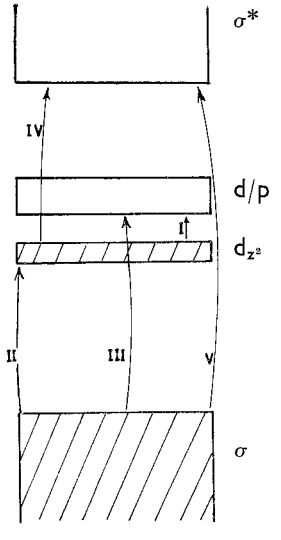

General types of interband transition for the trigonal prism group VI compounds.

($\alpha \sim 5000\,\text{cm}^{-1}$) to the low energy side of III in p-type MoS_2 (Evans and Young 1965). Finally, coming to confirm this pattern of bands a weak I.R. edge ($\alpha \sim 200\,\text{cm}^{-1}$) was discovered in MoS_2 at 0·2 ev. This is the

Fig. 28

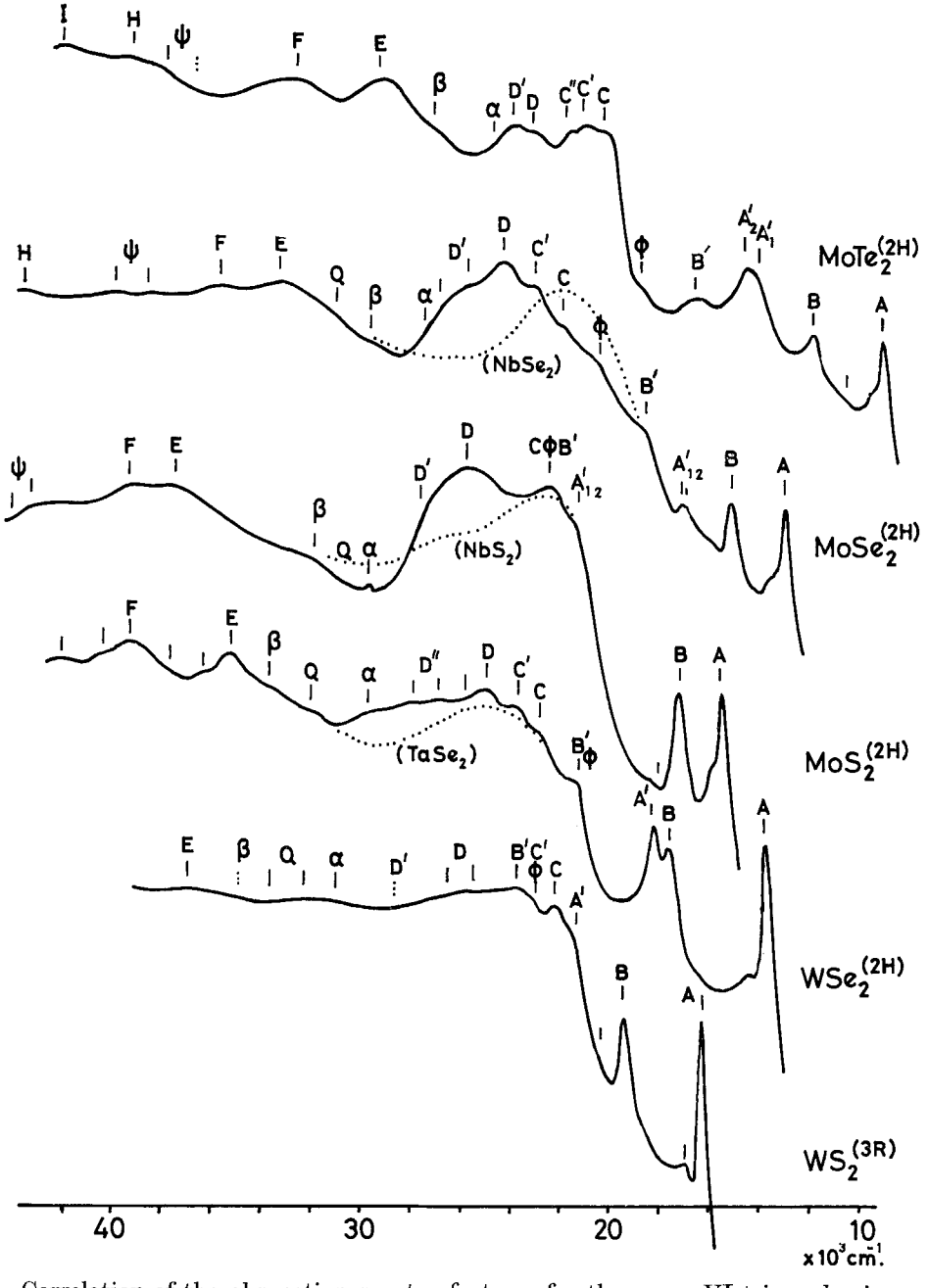

Correlation of the absorption spectra features for the group VI trigonal prism compounds. (Corresponding group V materials also shown in C/D region.)

Fig. 29

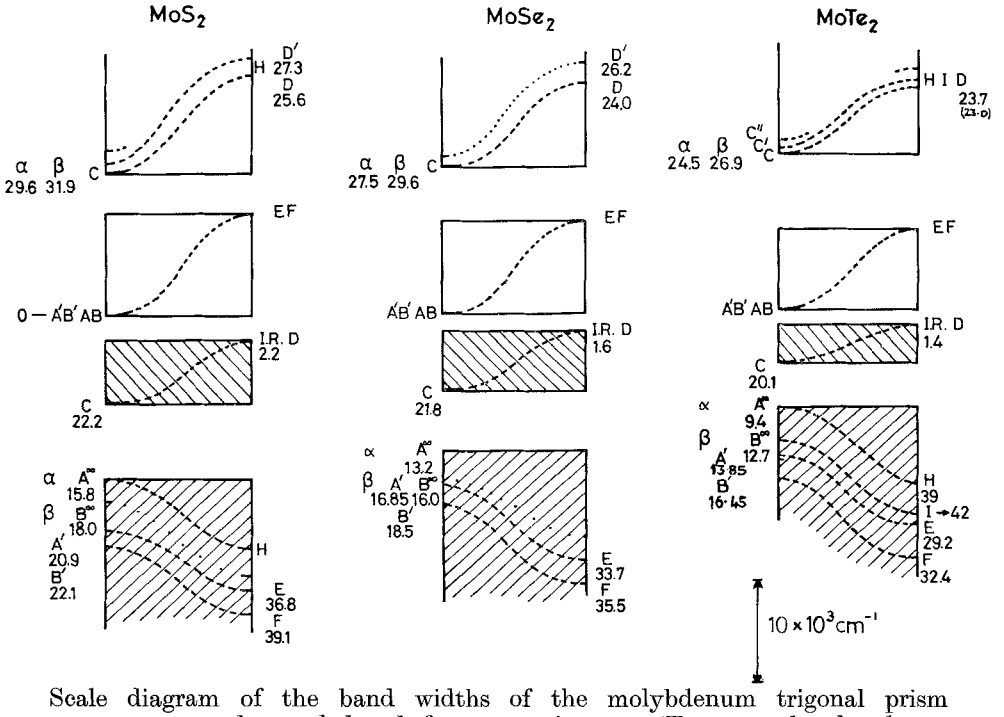

Scale diagram of the band widths of the molybdenum trigonal prism compounds as deduced from experiment. (Tungsten bands almost identical, apart from larger spin–orbit splitting.)

Fig. 30

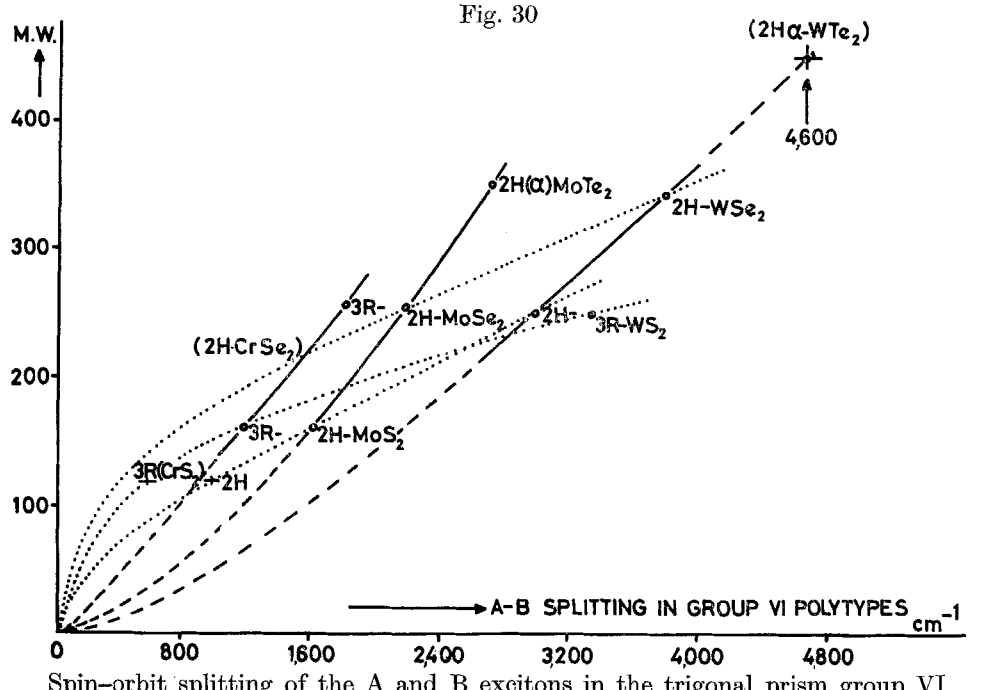

Spin–orbit splitting of the A and B excitons in the trigonal prism group VI compounds for the 2H and 3R stacking polytypes.

Fig. 31

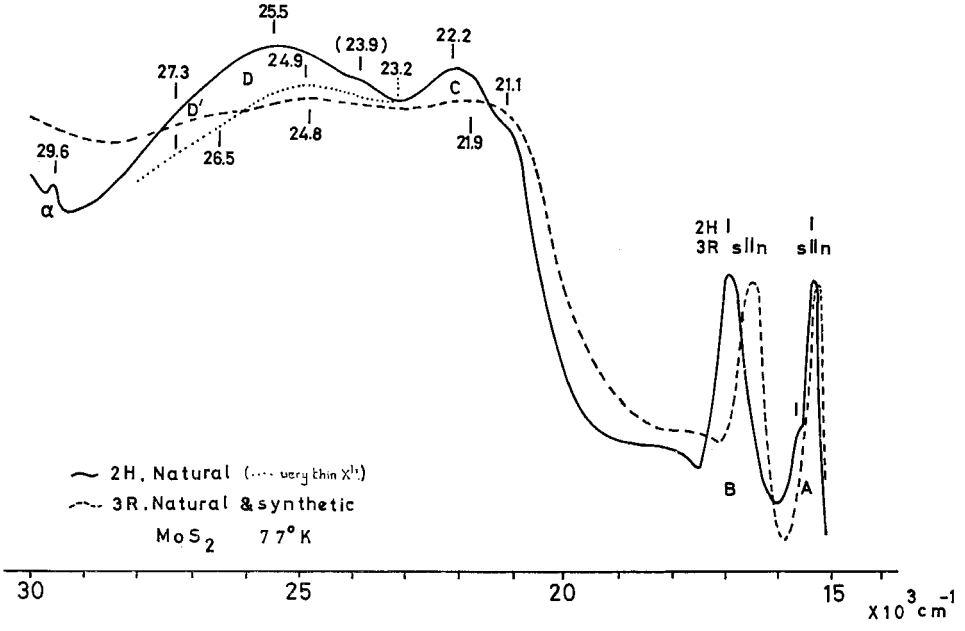

Comparison of optical absorption in 2H and 3R–MoS_2.

Fig. 32

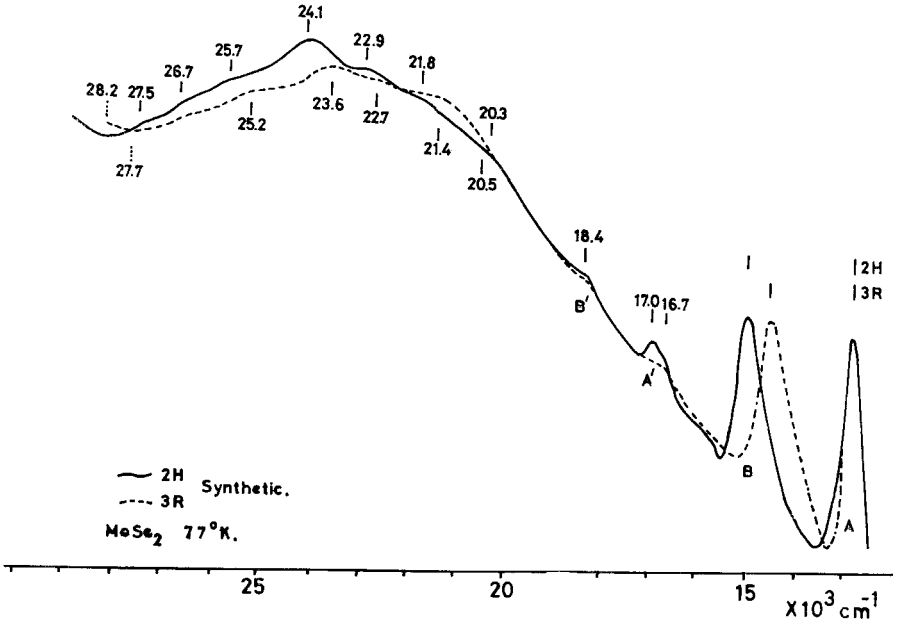

Comparison of optical absorption in 2H and 3R–$MoSe_2$.

transition of type I across the d band gap, which it is now realized determines the whole character of the electrical properties of the group VI semiconductors.

The way in which the details of the group VI spectra have been correlated is shown in fig. 28 (note the WS_2 is 3R type). Figure 29 is a scale drawing of the band widths we derive from this assignment. The sequence of operations by which this latter diagram is constructed is given in the experimental paper (Wilson, J. A. 1969).

One of the most noticeable changes in these spectra is the development of the A′ and B′ exciton peaks in the selenides and tellurides. Exciton α, conversely, is clearly defined only in 2H–MoS_2; such high energy excitons are well known in more ionic materials like CdI_2 and PbI_2 (Greenaway and Harbeke 1966, Kübler 1968).

Fig. 33

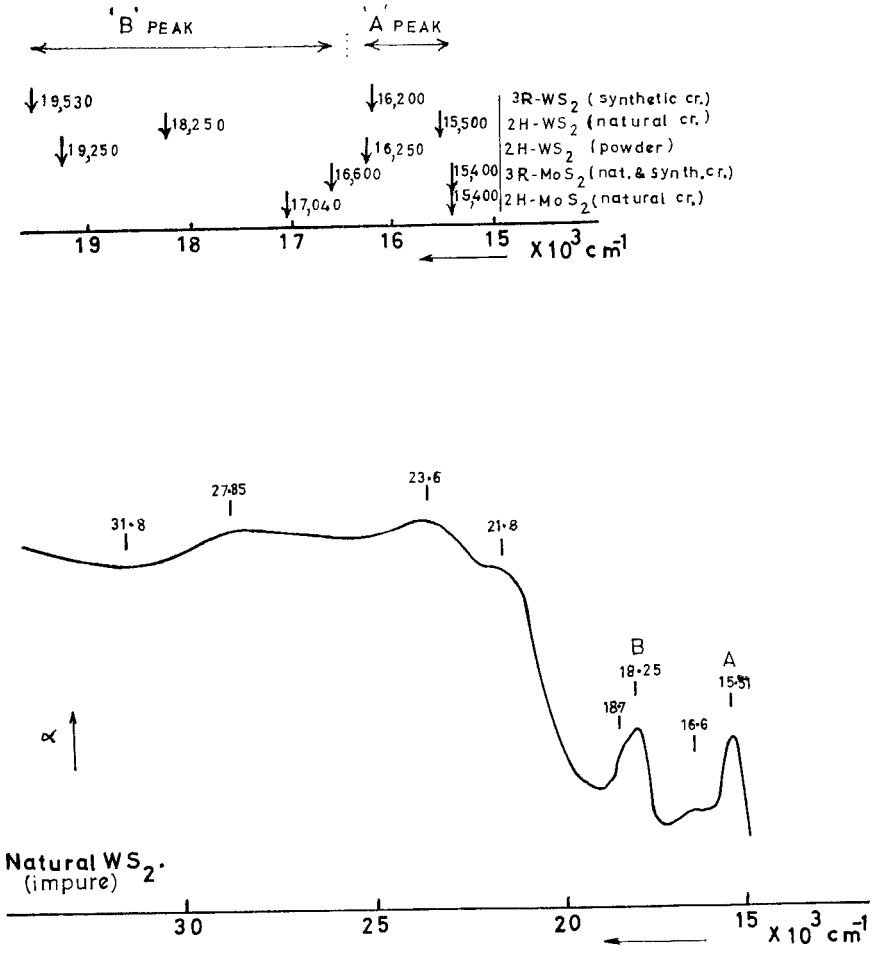

Exciton positions for the various samples of WS_2.

6.1.2 *The excitons A and B of group VI*

The pair of excitons A and B on the leading edge of the strong absorption range are interpreted as resulting from a spin–orbit split valence band. The splitting value of 0·2 ev for MoS_2 (A. W., Mo 96, S 32) is about as expected (compare Cd, same space group, viz. D_{6h}^4, A. W. 112, calculated splitting at H_3 of 0·2 ev (Stark and Falicov 1967)). Given also in fig. 30, a plot of spin–orbit splitting versus molecular weight, are the values found for the 3R stacking polytypes. The exact peak positions were recorded in table 7. As seen, there is a remarkable difference in the 2H and 3R splitting values, though the position of the A peak is virtually the same in each case for both polytypes. Figures 31 and 32 show other minor ways in which the spectra from the 2H and 3R polytypes differ for MoS_2 and $MoSe_2$ respectively. Reflection measurements on WS_2 2H powder (no 2H transport crystals obtained) seem to indicate that in this case the 2H splitting is less than for the 3R form (transport crystals). In fact a *natural* crystal of 2H–WS_2 (kindly given to us by Dr. S. Graeser) showed a splitting of only 2750 cm^{-1}, as against 3000 cm^{-1} for the 2H powder, and 3000 cm^{-1} for the 3R transport crystals. However, to confuse matters, the A peak in this natural crystal actually fell at a considerably lower energy (see fig. 33), although said to contain only 6% molybdenum. It is clear that more work on good WS_2 crystals needs to be done.

In the mixed systems $(Mo/W)Se_2$ and $Mo(S/Se)_2$ it seems (from preliminary experiments) that the two exciton positions move linearly with composition. It has been found possible by these means to 'tune' the exciton position to match the ruby laser photon output. In this way we hope to study the collective behaviour of the excitons at high densities. A Bose–Einstein condensation and excitonic superfluidity are topics being theoretically explored at the moment (see Gergel *et al.* 1968 *a, b*, Trlifaj 1968, Makarov 1968, Keldysh and Koslov 1968). Mixed crystals have also proved useful in establishing the identity of spectral features between materials (e.g. the A′, B′ excitons). A further interesting result is obtained

Fig. 34

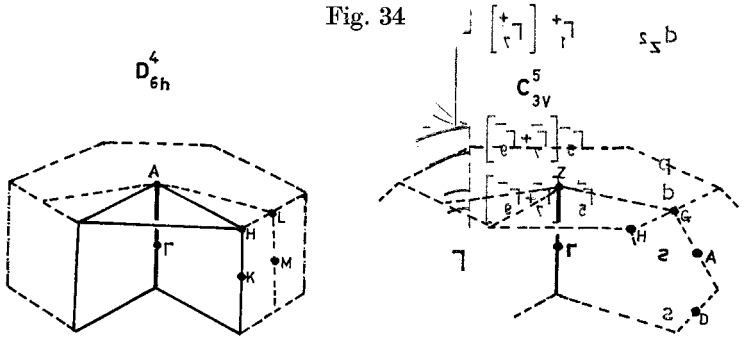

Indication of permissible positions in the Brillouin zone for spin–orbit splitting in space groups D_{6h}^4 and C_{3v}^5 (marked by continuous lines and bounded planes).

from mixed polytype specimens of a *single* compound. Several crystals of $MoSe_2$ seem from the x-ray powder patterns (see p. 219) to have mixed or disordered 2H/3R stacking. The optical spectra of these show an intermediate value for the exciton pair splitting, and, at the temperature (77°K) and resolution used, it did not seem that the B peak was made up to two separate components, as might have been expected.

The position of the A/B exciton pair within the Brillouin zone is fairly well assured. The two polytypes belong to different space groups—2H to $D_{6h}^4(P6_3/mmc)$, 3R to C_{3v}^5 (R3m)—and fig. 34 shows the group theoretical finding that only points on or around the k_z axis can supply the observed spin–orbit split pair common to both polytypes. Assuming that the various bands, following their tight-binding character, are described for states close to Γ in accord with the molecular orbital scheme of § 5.2, the representation assignment for point group D_{6h} can be made. Even though the space group D_{6h}^4 is non-symmorphic these point group rules should suffice at the Γ point (see work of Birman 1962, Zak 1962, and Gay *et al.* 1968 on selection rules in such groups). In the less highly symmetric group C_{3v}^5 (symmorphic) the selection rules of C_{3v} are not so rigid, and in fact appear over-generous. D_{3h}, the symmetry of the centre point for a

Fig. 35

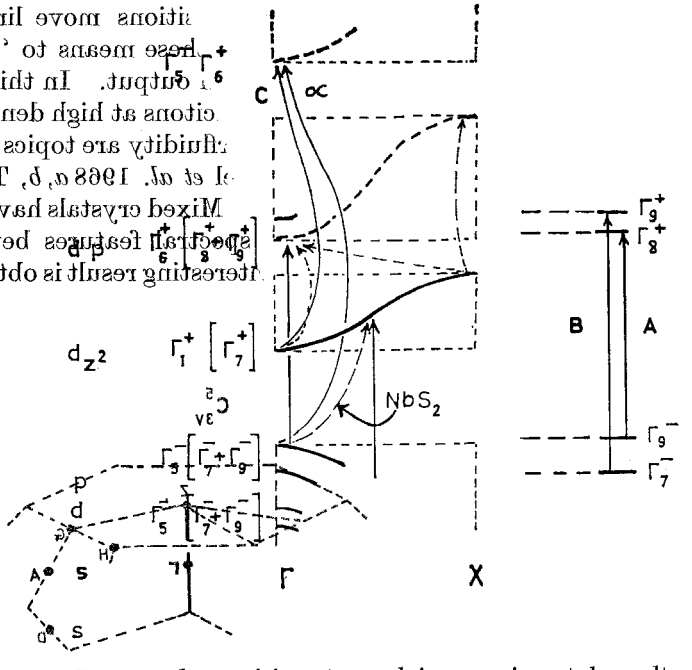

Suggested transitions to explain experimental results.
Weak transitions (dashed) fall below 2 ev.

Possible detailed assignment of transitions in MoS_2.

single sandwich, seems more appropriate. Some relaxation of D_{6h} towards D_{3h} would account for the weak transitions found at 9000 cm^{-1} in MoS_2 (possibly d_{z^2} to $d_{x^2-y^2}$), and also for the weak features that show up between excitons A and B on the leading edge of the B peak (see fig. 22; also Y. Liang 1967, MoS_2 reflection)†. Figure 35 summarizes this discussion.

At one time it was thought that excitons in layer compounds might be confined to a single sandwich (Shinada and Sugano 1965, Ralph 1965). The resulting two-dimensional exciton series would then go as:

$$-\frac{R}{(n+\frac{1}{2})^2}, \quad n=0,1,2,\ldots$$

as against

$$-\frac{R}{n^2}, \quad n=1,2,3,\ldots$$

for the standard three-dimensional case. However, for MoS_2 crystals of thickness greater than 5000 Å Evans and Young (1967 a, b, 1968) find that the latter expression fits their optical data very well (at least to $n=4$).

Fig. 36

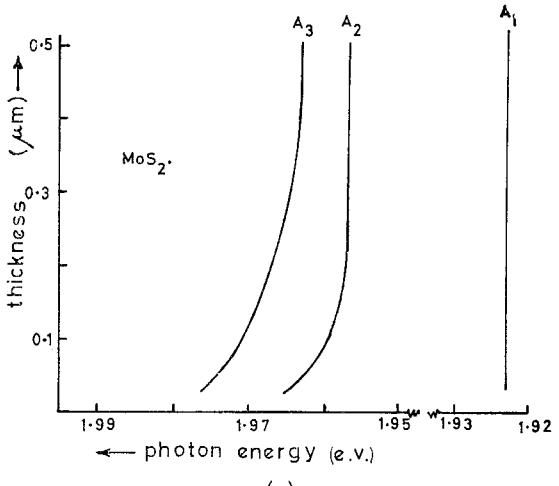

(*a*)

(*a*) Behaviour of A exciton peak positions in MoS_2 as function of crystal thickness. (Evans and Young 1967 a.)

† Reflection measurements which have just been made by Liang on crystals of 3R–WS_2 throw some doubt on the details of the above assignment. The crystals used were of sufficient thickness to allow reflection measurements to be taken from the side faces with the light polarized perpendicular and parallel to the *c* axis. In the latter polarization the exciton transitions A and B appear to be completely absent. Previously surface polished specimens had failed to reveal this marked polarization effect because the layers were folded over at the edge during polishing.

Fig. 36 (*continued*)

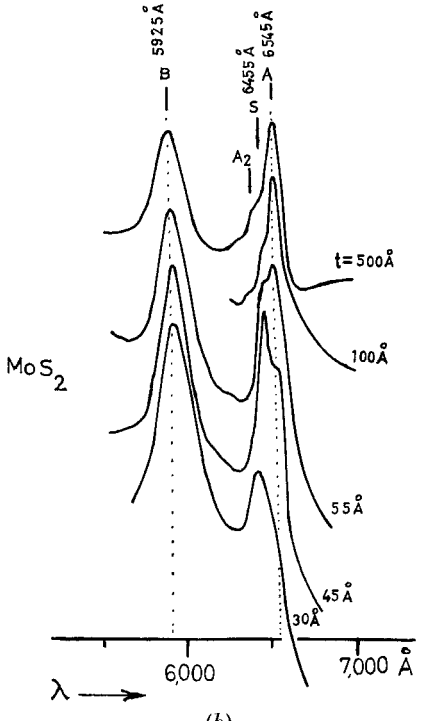

(*b*)

(*b*) Behaviour of the A $n=1$ exciton peak in ultra thin crystals of MoS_2. (Frindt 1965.)

Fig. 37

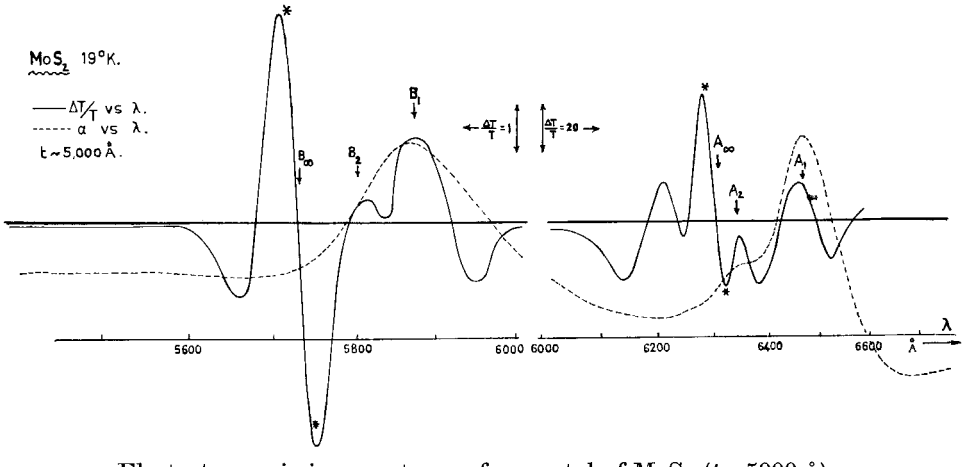

Electrotransmission spectrum of a crystal of MoS_2 ($t \sim 5000$ Å). (G. A. N. Connell, paper to be published.)

Harper and Hilder (1968) have now shown theoretically how the $1/n^2$ relation can hold up to very high degrees of band mass anisotropy. They have also demonstrated how spatial confinement of exciton bound states in crystals of thickness less than 5000 Å should lead to Evans and Young's observation (fig. 36 (*a*)) that the high-order exciton states ($n > 1$) are pushed to energies higher than are given by the $1/n^2$ expression as the crystal thickness is reduced (i.e. decreased binding). The radii derived by Evans and Young (1967 a) for the A exciton states in thick crystals are :

$$r_{\perp c}{}^{A} = 38{\cdot}5\, n^2, \quad r_{\parallel c}{}^{A} = 24{\cdot}5\, n^2 \text{ Å},$$

so that for $n = 3$,

$$r_{\parallel c}{}^{A} \sim 200 \text{ Å}.$$

The $n = 1$ peak is stable in position for crystals as thin as 100 Å (see fig. 36(*b*)), though below this the A peak does show a companion to higher energies, (Frindt 1965). Another striking thickness effect, noted in fig. 31, is the marked weakening and red shift of the D transition for $t < 500$ Å. This suggests that the D transition occurs away from the Γ point, possibly along the k_z axis. Again referring back to fig. 31 for MoS_2, it is not clear why the transmission well following peak D ($\sim 3\frac{1}{2}$ ev) shows so much more strongly in 2H–MoS_2 than in 3R–MoS_2, natural or synthetic, or in 3R–WS_2. The crystal quality seems no poorer ; indeed the excitons in these 3R materials are even sharper than for the 2H form. By contrast to this latter point, however, the $n = 2$ hump is not seen in direct transmission on the 3R excitons (77°K). Electro-transmission and electro-reflection measurements are currently being carried out in our laboratory to assess the binding energies of all these group VI excitons (G. A. N. Connell, E. A. Davis and J. Bordas). Separate signals of characteristic form are obtained from the exciton states ($n = 1$, $n = 2$) and from the band edge. The various features in these modulation spectra can be brought out by a suitable choice of field strength. Figure 37 shows a trace obtained for 2H–MoS_2 at 20°K. The binding energy of the A exciton is found to be $0{\cdot}050 \pm 0{\cdot}004$ ev, or 400 ± 30 cm^{-1}. For 3R–WS_2 this is increased slightly.

Evans and Young's value for MoS_2 from direct transmission of 350 cm^{-1} compares reasonably with the above modulation value. However, their value for the B exciton of just over 1000 cm^{-1} is quite different from the present finding of 360 ± 30 cm^{-1}. Indeed it would seem that the measurements of Evans and Young have been made on the fairly strong 'anti-resonance' feature that follows the B exciton. Features of this latter type have found several explanations (see Phillips 1966, §§ 27 and 28, Shinada and Sugano 1965, Halpern 1966). The fine detail observed on such post-excitonic humps (cf. Liang and Yoffe 1968) has lead to the exciton–phonon complex (E.P.C.) interpretation. Coupling occurs between the lattice and the internal field of the exciton (Toyazawa and Hermanson 1968), and is strongest in crystals of medium ionicity where the exciton

binding energy is comparable to longitudinal optic phonon energies (i.e. $\sim 0{\cdot}03$ to $0{\cdot}05$ ev). Features of this type are particularly apparent in the spectra of fig. 22 following the A peaks in WS_2, WSe_2 and α-$MoTe_2$. GaSe shows such behaviour following the indirect exciton at 2 ev (Halpern 1966) and GaS shows a very strong hump of this type following the direct exciton at 4 ev (see fig. 20 (*o*)). This hump in GaS extends over 2000 cm^{-1}, with its peak at a similar separation from the exciton $n = 1$ peak. Several of the very strong post-excitonic features observed by Tubbs (1968) in layer halides like PbI_2, ZnI_2, CaI_2, BiI_3 may also be of this E.P.C. origin. The E.P.C. complex gives signals in the electromodulation experiments and one is apparent in the above diagram following the A exciton.

Electro-reflection measurements on the excitons in PbI_2 at 2·5, 3·3, 3·9 and 4·4 ev have been made by Gahwiller and Harbeke (1968). They failed to obtain clear band edge signals at the field strength employed, although there is a considerable amount of other detail. The exciton on the leading edge in PbI_2 is very strong and sharp ($W_{1/2} \sim 150$ cm^{-1}) at 77°K, but has virtually disappeared at 300°K. This is similar to the behaviour of the excitons in ZnO, etc. ($W_{1/2} \sim 100$ cm^{-1} at 77°K; $E_b = 0{\cdot}065$ ev). From direct optical absorption on PbI_2 (Nikitine *et al.* 1964) it was suggested that the binding energy is *ca.* 0·14 ev, but the poor temperature stability of the PbI_2 exciton contrasts strongly with that of the MoS_2 doublet. In MoS_2 etc., the A peak is still to be seen at 200°C ($W_{1/2}$, 400 cm^{-1} at 77°K; 500 cm^{-1}, 300°K). The B peak is, however, more temperature sensitive (particularly in WS_2/Se_2 and α-$MoTe_2$), presumably because of auto-ionization into the degenerate bands. Excitons beyond the absorption edge are not in fact uncommon in more ionic compounds (e.g. the very stable pair in CdI_2 at 6 ev, Greenaway and Nitsche 1965; also see GaS/Se). The high energy peaks found in PbI_2 show considerable fine structure (Greenaway and Harbeke 1966), which has again been attributed to phonon interaction. Fine structure on the exciton peaks can also arise from polytype effects, as Brebner and Mooser (1967) have noted for GaSe. There the indirect exciton at 2 ev suffers splittings of up to 0·004 ev from this cause. This is somewhat smaller than the shift already noted in the position of the A peak for MoS_2 between the 2H and 3R polytypes ($\sim 0{\cdot}010$ ev – see fig. 31.)

In the MoS_2 family the excitons are not only broadened by phonon collisions at raised temperatures, but also suffer screening of the coulombic binding interaction via the quite appreciable number of free carriers produced by thermal excitation out of the d_{z^2} band into the d/p conduction band (see § 7.3). Optical experiments at very high pressures ($\lesssim 60$ kB, Connell, Wilson and Yoffe 1968) suggest that this latter band gap decreases (the peak C reddens), and that the exciton binding energy (i.e. stability) is accordingly reduced through enhanced screening. A factor of this type contributes at all but the very lowest temperatures to the observed *blue* shift of the excitons (300°K, $2{\cdot}0 \times 10^{-3}$ ev/kB; 77°K, $1{\cdot}4 \times 10^{-3}$ ev/kB). The d band gap closure rate is estimated to be $2{\cdot}5 \times 10^{-3}$ ev/kB, so that a pressure

of 200 kB should close completely the d band gap. Indeed Minomura and Drickamer (1963) find a fall of almost three orders of magnitude in ρ for MoS_2 between 0 and 200 kB, with then no further change to 500 kB. It was not reported whether under these conditions any phase change occurred. $MoTe_2$ is known to convert to the β phase (see § 8.1) at high pressures and temperatures. This distorted octahedral layer material is a superconducting semi-metal, ($\rho_{300°K} \sim 10^{-3}$ Ω-cm), lacking the d band gap of the α form. In α-$MoTe_2$ this gap under room conditions is $\sim 0{\cdot}1$ ev. If this interpretation of the pressure experiments is correct α-$MoTe_2$ should be an ideal

Fig. 38

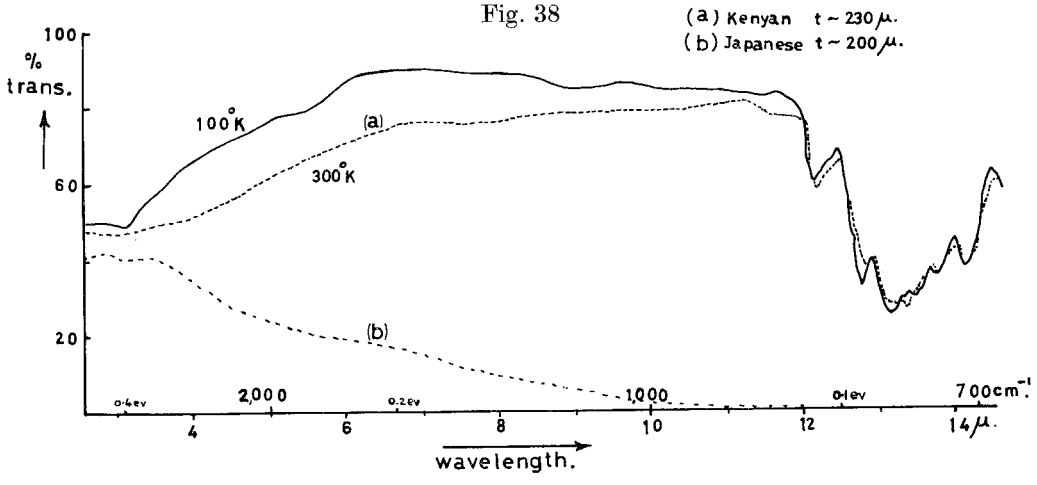

Indirect absorption edge in MoS_2.

Fig. 39

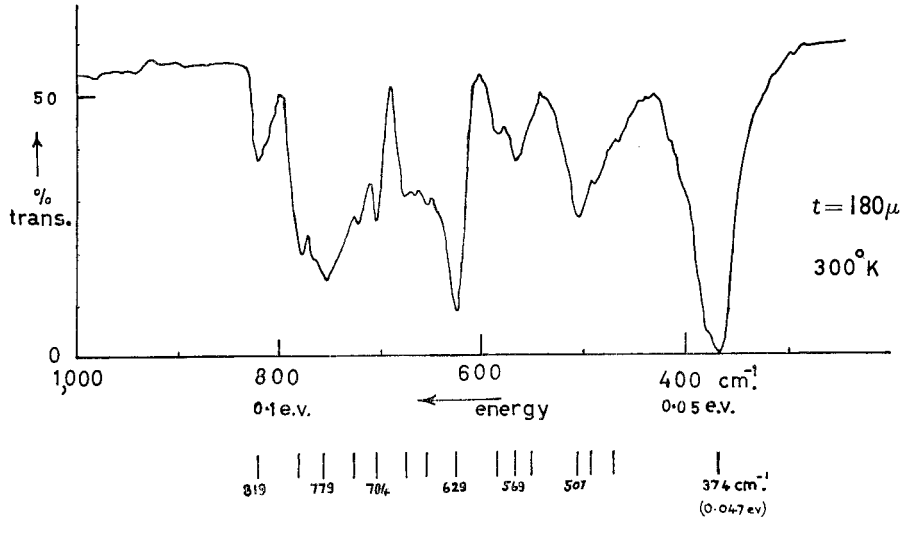

Phonon spectrum of MoS_2 out to 40 μ.

material on which to test the theory of the 'excitonic insulator' (discussed in § 8.2). It is intended to attempt optical experiments under pressure at 4°K on α-$MoTe_2$ to see if new phases of the excitonic insulator type are produced when the d band gap is reduced to the order of the excitonic binding energy (i.e. $\sim 0{\cdot}03$ ev).

6.1.3 *Phonon spectra and the indirect edge*

Direct infra-red spectroscopic evidence of the above indirect band gap has been secured using large natural MoS_2 crystals $\sim \frac{1}{4}$ mm thick. Figure 38 shows the weak absorption edge at 0·25 ev. Also evident on this diagram is the start of the phonon spectrum, which is shown in full in fig. 39. The line at 27 μ still shows up for crystal thicknesses $\sim 1\,\mu$ in classical oscillator form, and is interpreted as the T.O. phonon. The phonon spectra in ZrS_2, SnS_2 and GaS all appear to have slightly lower energies. As yet similar results on the other members of the MoS_2 family have not been obtained, due to lack of large thick crystals. Measurements on 3R–MoS_2 would be particularly interesting as they would indicate through comparison with the 2H results the degree of inter-sandwich coupling.

Phonon spectra cannot of course be obtained for the group V materials because metallic free-carrier absorption occurs throughout the I.R. In VSe_2 (octahedral) this extends well into the visible, obscuring any direct absorption edge. However, for the trigonal prism materials, like $NbSe_2$, the thinned crystals are strongly coloured. Here the free-carrier rise below *ca.* 1 ev is well separated from the direct absorption edge above *ca.* 2 ev. The position of this free-carrier rise so far into the I.R. demonstrates the small width of the band (d_{z^2}), in which the metallic carriers lie. This was estimated above from the group VI spectra to be of about 0·5 ev (see fig. 29). Such a value is thought to be very close to the lower limit for

Fig. 40

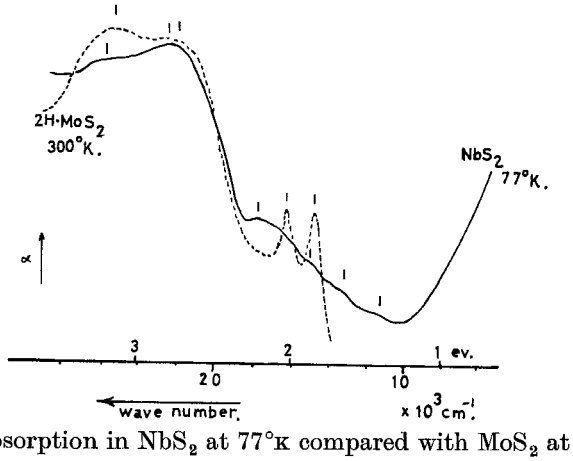

Optical absorption in NbS_2 at 77°K compared with MoS_2 at 300°K.

simple band formation†. Despite the fact that the direct interband transitions are not overlaid by the free carrier absorption, all spectral detail is lost from these group V materials as compared with their group VI counterparts (see fig. 40). The free carriers lead to a general broadening through collision processes, and also to loss of excitonic features through the coulomb screening (see § 7.3).

6.2. *The Group IV materials*

In contrast to groups VI and V, the 3d dichalcogenides of group IV (Ti) have the same structure type as do its 4d and 5d members (viz. CdI_2). The transmission spectra show that the 4d (Zr) and 5d (Hf) compounds are energetically very similar (a reflection of the lanthanide contraction), whilst the titanium compound transitions are to considerably lower energies. All are semiconductors but the titanium compounds, and particularly the sulphide, because of the very poor stoichiometry ($n \gtrsim 10^{20}/cm^3$—e.g. Bernard and Jeannin 1962), differ in that free-carrier absorption encroaches

Fig. 41

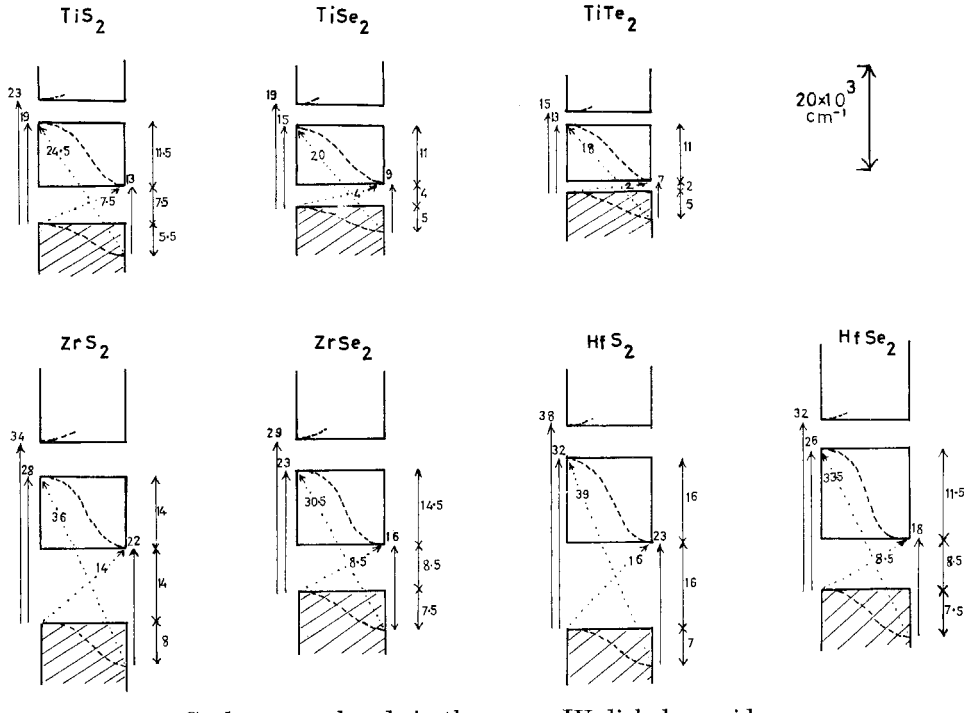

Scale energy bands in the group IV dichalcogenides, constructed from optical data.

† Contrast even the position for the plasma edge in the metallic oxides CrO_2 and ReO_3, of 1·4 and 2·0 ev respectively.

almost to 1 ev. Stoichiometry is shown to be better in ZrS_2 and $HfSe_2$, and in HfS_2 there is no trace of free-carrier absorption to 15 μ (Greenaway and Nitsche 1965). This finding matches the changes in resistivity, etc. for these compounds, as normally prepared (see § 7.1).

It has been found that the group IV materials also possess an indirect edge, but this shows to considerably higher energies than for the group VI case, and with greater oscillator strength. It is the stoichiometry difference which explains why MoS_2, etc. are invariably *in*trinsic at room temperature, whilst the group IV materials are always *ex*trinsic. The optically determined indirect edge positions are:

$$ZrS_2\ 1{\cdot}75,\quad HfS_2\ 1{\cdot}95,\quad HfSe_2\ 1{\cdot}15\,\text{ev},$$

(Greenaway and Nitsche 1965) and these values have been used in constructing the block banding of fig. 41. The construction details are again given in the experimental paper (Wilson 1969 a). As is seen the d band here may be up to 2 ev wide. The width of the top valence band seems to be $\sim 0{\cdot}6$ to 1 ev, a value similar to that obtained by calculation for the non-transition metal layer compounds GaS (Bassani and Parravicini 1967), SnS_2 (Au Yang and Cohen 1969) and Bi_2Te_3 (Borghese and Donato 1968).

An unusual feature common to all the group IV spectra is the sharp peak topping the leading absorption edge of direct transitions. Though this feature sharpens considerably on cooling, it undergoes no appreciable temperature shift and shows no fine structure. It is not clear then whether it is excitonic in character and measurements at liquid helium temperature together with modulation experiments need to be made. Also sharpening strongly is the peak of maximum absorption, and it may be that this peak, together with the leading feature, form a spin–orbit split pair. If the features are excitons, it is a little strange that in the most stoichiometric compound, HfS_2, the peak has not the sharpness shown by ZrS_2 and $HfSe_2$ (see also fig. 23 (*a*)).

6.3. *The Group VIII Layer Dichalcogenides*

In group VIIIc the d band is completely full and the semiconductivity of PtS_2 and $PtSe_2$ follows. However, because of the relatively low heat of formation (< 30 kcal/mole; Westrum *et al.* 1961), the band gap, $d \rightarrow \sigma^*$, accordingly, is small. This is confirmed by electrical measurements (E_g^{el}, PtS_2 0·7 ev; $PtSe_2$ 0·1 ev—Hulliger 1965). All the spectra are disappointingly bare. For the tellurides $NiTe_2$, $PdTe_2$ and $PtTe_2$ it seems that the σ^* band dips into the d band, as these materials are all metallic, and highly opaque ($PdTe_2$ is a superconductor, $T_s = 1{\cdot}5°\text{K}$). They resemble more the tellurides of group VIIIb, β-$CoTe_2$, β-$RhTe_2$ and $IrTe_2$, which are expected in any case to be metallic. Again these compounds are extremely opaque. Poor stoichiometry, particularly for $CoTe_2$, seems to contribute to this and the crystals available tended to crack badly during cleaving. For all these group VIII materials c/a is small, with large a values and a contracted van der Waals gap (see table 2, and compare Bi_2Te_3). The cause of this structural deformation is discussed in § 9.2.

Fig. 42

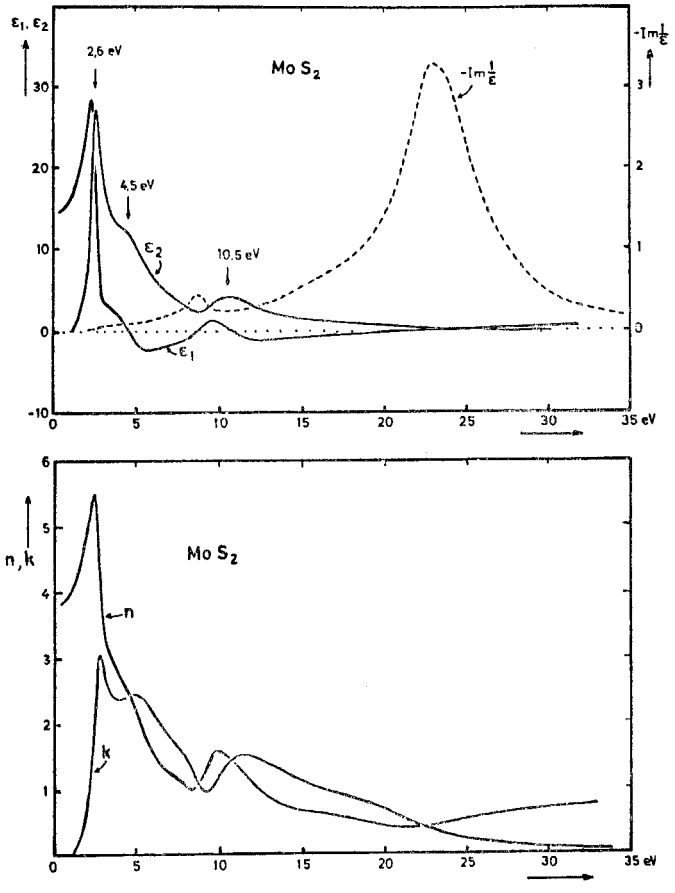

(*a*)

(*b*)

(*a*) Plots of ϵ_1, ϵ_2 and Im $(1/\epsilon)$ for MoS_2. (Zeppenfeld, private communication 1969.) (*b*) n and k plots for MoS_2. (Zeppenfeld, private communication 1969.)

Fig. 43

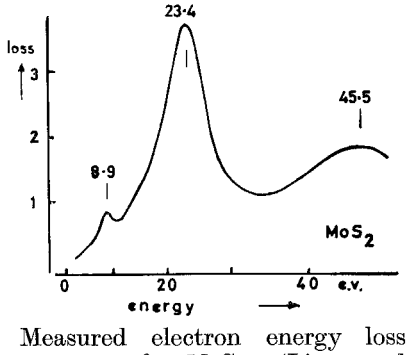

Measured electron energy loss spectrum for MoS_2. (Liang and Cundy 1969.)

Fig. 44

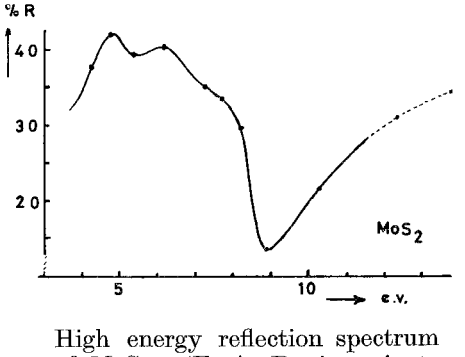

High energy reflection spectrum of MoS_2. (E. A. Davis, private communication 1968.)

6.4. *U.V. and Electron Energy Loss Spectra*

The above transmission spectra are supplemented by some U.V. reflection work on MoS_2 (Davis 1968, private communication), and on the group IV materials (Greenaway and Nitsche 1965) out to 12 ev, and also by electron energy loss spectra on the materials of groups IV, V and VI (Liang and Cundy 1969). The latter type of spectra are known to show peaks in regions where both ϵ_1 and ϵ_2 move close to zero. This often occurs following one strong absorption band and before the commencement of another.

Fig. 45

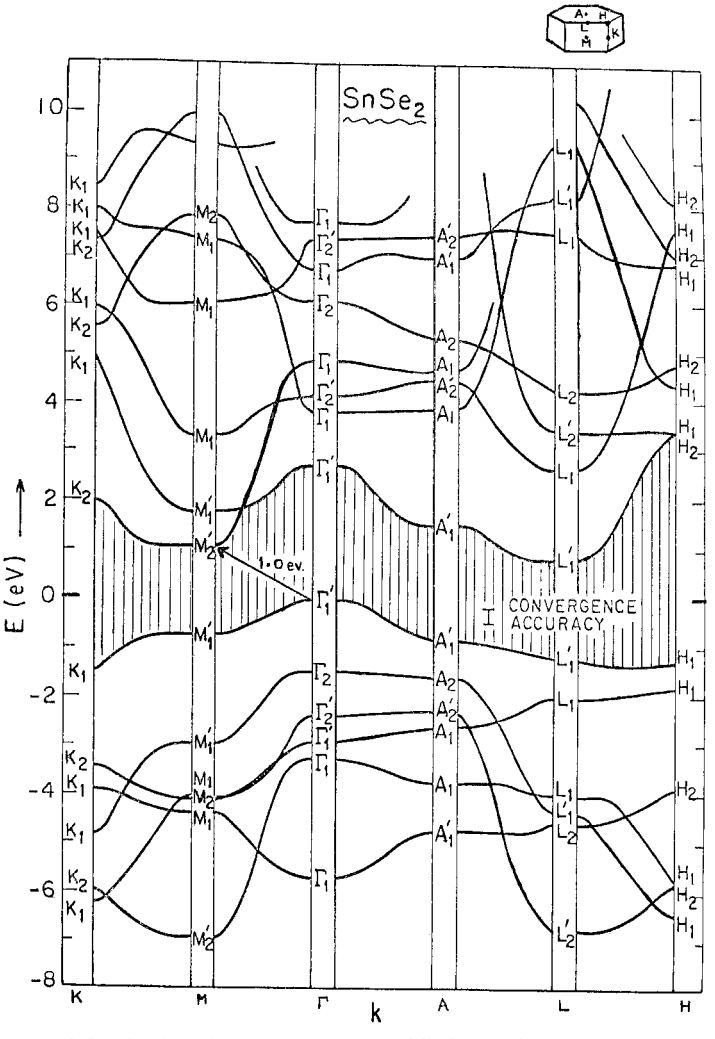

Pseudo-potential calculated band structure of $SnSe_2$. (Au Yang and Cohen 1969.)

An example of this is shown in fig. 42, where ϵ_1, ϵ_2, and the imaginary part of $1/\epsilon$ (proportional to the 'energy loss') are plotted together for MoS_2. These plots follow a Kramers–Kronig analysis. The corresponding n and k plots are shown also. The observed electron energy loss spectrum is shown in fig. 43. A direct U.V. reflectivity plot for MoS_2 is given in fig. 44. The deep absorption well at 9 ev is clearly picked up by the energy loss spectrum. The loss peak at 23·4 ev is that of the plasma resonance response for the 18 valence electrons of MoS_2. In NbS_2 and ZrS_2 this energy falls to 22·3 ev and to 20·3 ev, as the number of valence electrons falls to 17 and 16 respectively. The 8·9 ev peak for MoS_2 occurs in NbS_2 at almost the same energy (8·7 ev), as it should if indeed the band structures are closely similar. In the 5d materials, like WSe_2 and $TaSe_2$, this peak is not so well defined. Conversely, in group IV the low energy peak which occurs just short of 4 ev is better defined for the hafnium compounds than for the 4d zirconium compounds. Again this is in good agreement with the wells found in both absorption and reflection at this energy. The group IV reflection spectra obtained by Greenaway and Nitsche (1965) were shown in fig. 23.

It is interesting to note that despite the common number of valence electrons the plasma resonance occurs in SnS_2 at a considerably lower energy than in ZrS_2, viz. 18·2 ev as against 20·2 ev. The reflection spectrum for SnS_2 has been given in fig. 23. The electron energy loss spectrum of SnS_2 picks out the well at 9·1 ev clearly. These spectra for the group IVA layer dichalcogenides are then quite different from those of the IVB layer compounds, which is not surprising in view of the different character of the states mixed into the valence band.

SnS_2 is the only AX_2 layer compound for which a complete band structure has been published (Au Yang and Cohen 1969). This is shown in fig. 45. It was obtained by the semi-empirical pseudo-potential method. If the results are to be trusted on this point, it indicates that many of the bands in the ΓA direction (i.e. for electron waves propagating in the c direction perpendicular to the sandwiches) are not as flat as might have been expected from the low conductivity in this direction. The same feature is found in the published band structures of Bi_2Te_3 (Borghese and Donato 1968, Katsuki 1969).

The similarity between MoS_2 and GaS—which might well be written as $(Ga_2)S_2$ to indicate the common 18 electrons per 'unit' (see § 4)—is again rather superficial, as is revealed by the energy loss measurements. The main plasma resonance occurs in GaS at only 17·2 ev, compared with 23·4 ev in MoS_2. A small energy loss peak in GaS at 7·5 ev marks the sharp dip in reflectivity at this energy; to be seen in fig. 23. The two non-bonding d_{z^2} electrons of MoS_2, which lie within the $\sigma\sigma^*$ gap, are in GaS replaced by the electrons of the metal–metal Ga_2 bond, and these are mixed into the top of the principal valence band. Various preliminary attempts towards elucidating the band structures of these III–V compounds are now available (see Kamimura and Nakao 1968, Bassani and Parravicini 1967, Andriyashik *et al.* 1968).

Fig. 46

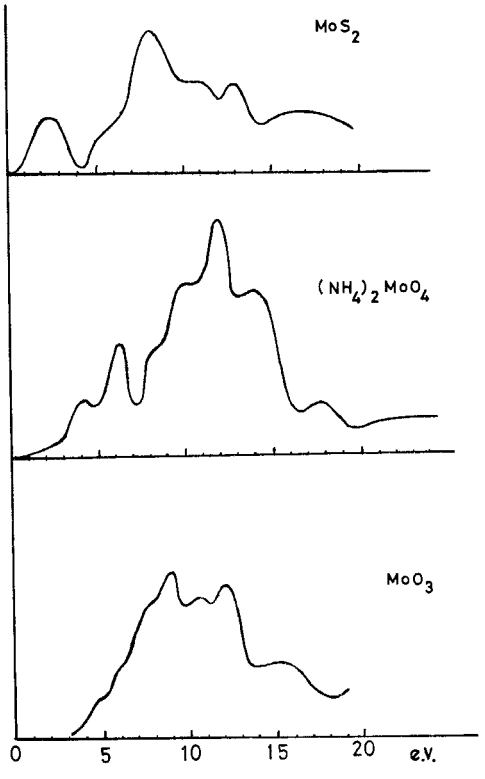

Soft X-ray absorption spectra (L III) of MoS_2, $(NH_4)_2MoO_4$ and MoO_3. (Experimentally, points placed every electron volt with accuracy 0·15 ev—Barinskii and Vainshtein 1957.)

Another high energy technique which can yield useful information on band structures is soft x-ray absorption. The LIII absorption spectra (x-rays generated by 5 kv electrons) involve excitation of the 2p electrons. Accordingly transitions to high energy unoccupied s and d states will show up most strongly. The LIII x-ray spectra of MoS_2, MoO_3 and $(NH_4)_2$ MoO_4 are shown in fig. 46. Transitions into the upper empty non-bonding d band of MoS_2 appear strongly. Since the points are spaced only every electron volt, and then have an uncertainty of about 0·15 ev, the fine structure must be viewed with some suspicion. However, the leading pair of sharp peaks in $(NH_4)_2$ MoO_4 represent typically 'salt-like' d states. The $\sigma\sigma^*$ gap is known to be about 7 ev (see Muller *et al.* 1967). The edge in MoO_3 also corresponds with the optical absorption edge of 3 ev (see Dickens and Neild 1968). A very interesting experiment of this type would be with NbS_2. Now that experimental techniques have improved somewhat it may

Fig. 47

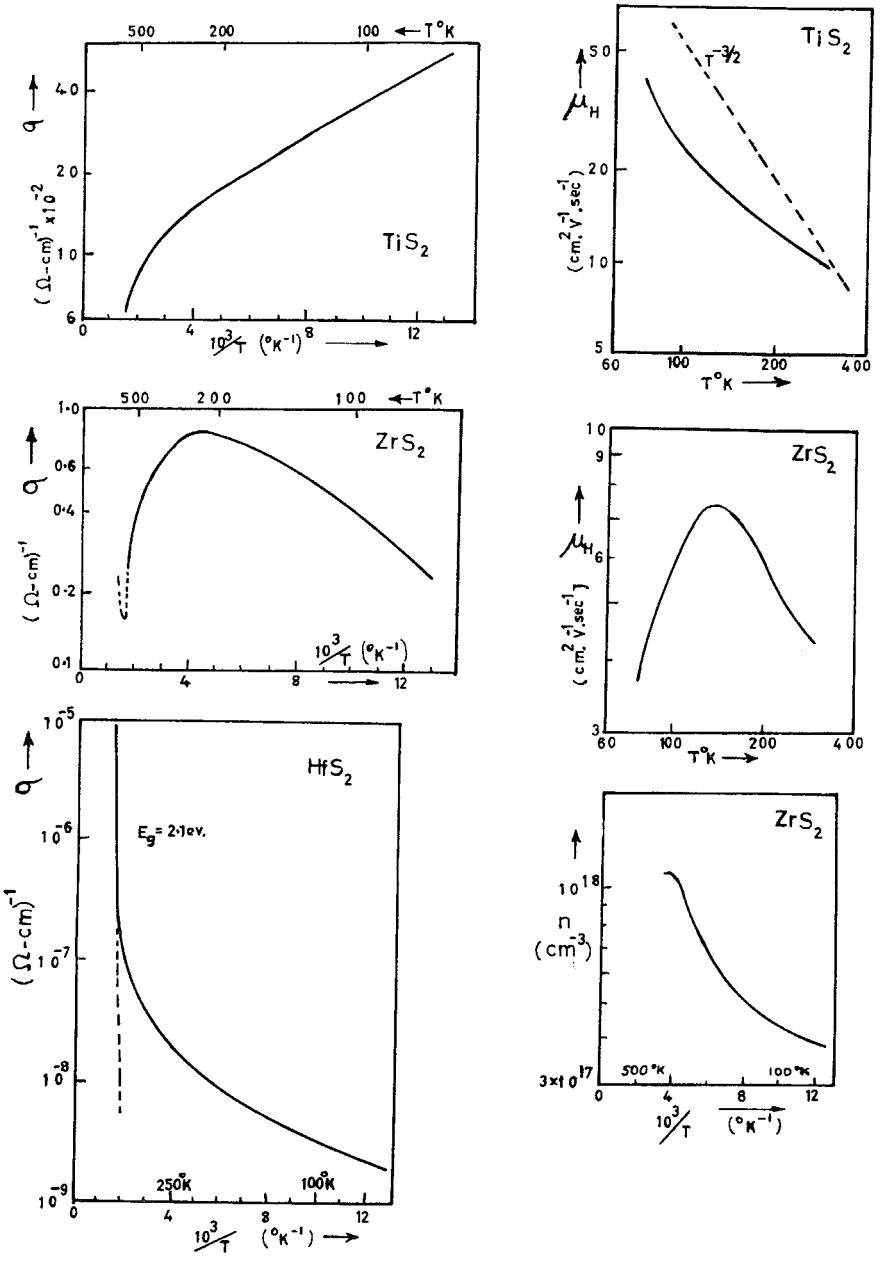

Electrical data on the group IV TX_2 layer dichalcogenides.
(From Conroy and Park 1968.)

be possible to pick up a narrow line preceding the first hump of MoS_2, corresponding to transitions into the now half empty d_{z^2} band. A recent example of soft x-ray absorption made on the various oxides of titanium is that by Fischer and Baun (1968).

§ 7. The Electrical and Magnetic Properties of the *Regular* Layered TX_2 Dichalcogenides

7.1. *The Group IV Dichalcogenides*

The observed electrical properties of this group of materials are readily understood in terms of the band diagrams of fig. 41, plus a knowledge that they persistently form in non-stoichiometric proportions. This latter tendency is much worse for titanium (cf. TiO_2) than for zirconium or hafnium, (see pp. 213 and 253), and again for the tellurides than for the sulphides. The d band in these compounds must be much better established than in TiO_2 since the latter, in non-stoichiometric condition, shows the much investigated low-mobility small polaron transport behaviour†. For dichalcogenide specimens on the other hand, the conductivity can quickly rise to 1 Ω-cm^{-1} or higher. The electrical character of the dichalcogenides is likely to be determined by the known excess of metal atoms, sited in the van der Waals gap sites, donating electrons through into the otherwise empty d band. n-type behaviour is indeed always observed. Of the whole group only HfS_2 has been prepared stoichiometrically enough to allow an electrical determination to be made of the intrinsic energy gap. The value obtained by Conroy and Park (1968) (2·1 ev) is close to the value deduced by Greenaway and Nitsche from an analysis of the indirect absorption edge ($\sigma \rightarrow$d, see p. 254. For $TiTe_2$ this gap has shrunk to close to zero, and indeed $TiTe_2$ may just be a semi-metal.

The following data drawn from McTaggart and Wadsley 1958), Grimmeis *et al.* (1961) and Conroy and Park (1968) show some typical results, as also does fig. 47.

	TiS_2	ZrS_2	HfS_2	$TiTe_2$
n	9×10^{20}	10^{18}	$< 10^{17}$	$\sim 10^{21}$ cm^{-3}
ρ	5×10^{-3}	1	$> 10^5$	2×10^{-5} Ω-cm
S	-200	-700	-1000	-20 μv/°c

† The conduction mechanism in TiO_2 is again being queried—see *Sol. Stat. Comm.*, **7**, 245 (1969). Electrical switching effects similar to those reported in amorphous materials are currently being found in several semiconducting layer crystals, e.g. ZrS_2, SnS_2, $AsSe_3$, Sb_2Se_3, etc. by a number of investigators.

7.2. *The Trigonal Prism Group VI Materials*

7.2.1. *General electrical results*

These compounds are diamagnetic and are quite unlike the localized spin paramagnetic layer salts, such as $FeCl_2$ or VCl_2. All the properties of layer materials are very anisotropic, and for MoS_2 the molar susceptibility values are:

$$\chi_\perp = -50 \times 10^{-6}, \quad \chi_\parallel = -115 \times 10^{-6} \text{ c.g.s. e.m.u. at } 300^\circ\text{K},$$

see fig. 48. The actual measurements by Paul (née Das, 1968) were of $\chi_\perp$ and $\chi_\perp - \chi_\parallel$.

Fig. 48

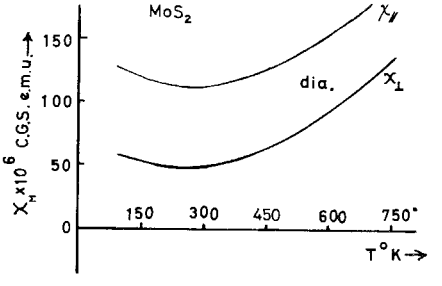

Magnetic susceptibility of MoS_2 crystals. (From Das 1968.)

The conductivity values parallel and perpendicular to the layers indicate a ratio possibly even in excess of 10^3. The two values show similar temperature behaviour, the mobilities carrying the 10^3 factor and the carrier number changing exponentially with temperature. A majority of group VI samples appear intrinsic in the temperature range 250 °K to 500 °K with respect to the indirect d–d gap mentioned earlier. In MoS_2 this band gap is of approximately 0·25 ev, and typical self-consistent values at 300 °K are:

$$E_g \approx 0{\cdot}2 \text{ ev}, \quad R_H \approx 100 \text{ cm}^3/\text{coul}, \quad n = 10^{16}\text{–}10^{17}/\text{cm}^3, \quad S \sim 500\,\mu\text{v}/^\circ\text{K}$$

$$\sigma_{(\perp c)} = 0{\cdot}1 - 1 \text{ (ohm-cm)}^{-1}, \quad (\mu_H)_e \approx (\mu_H)_h \sim 100 \text{ cm}^2/\text{v-sec. } (\perp c).$$

Electrical measurements on single crystals of MoS_2, etc. have proved very difficult to obtain satisfactorily, due to the layered character of these materials. The crystal edges are exceedingly soft and any damage on a microscopic level must lead to extensive 'shorting out' of the high crystalline anisotropy of the sandwiches. Preliminary measurements of a.c. conductivity parallel to c in which a guard ring technique was used show that the conductivity is proportional to frequency in the range 10^5 to 10^7 c/s. This is consistent with a hopping mechanism across the layers particularly at low temperatures (Shaw 1969). Several d.c. measurements on the

Table 9. Collected electrical data on the

Worker	Date	Substance	Specimen preparation	Carrier type	Resistivities (Ω-cm) and activation energies (ev)	Hall coefficient R_H (cm^3/cb)
Lagrenaudie	1954	MoS_2	Natural crystal	p	E_a < 300°K, 0·03 to 0·06 ev > 700°K, 0·72 ev	—
Evans and Young	1965	MoS_2	Natural crystal	—	290°K, $\rho \parallel c = 2 \times 10^3$ $\rho \perp c = 12$ E_a < 400°K = 0·87 ; > 400°K = 0·08 ev	—
Mansfield and Salaam	1953	MoS_2	Natural crystal	Mainly p	$\rho^{300°K}$ between 3 and 100 Ω-cm E_a(< 600°K) 0·03 to 0·14ev E_a(> 600°K) ~ 1 ev	~ 50 at 300°K (two samples with 3000) (see fig. 50)
Regnault	1952	MoS_2	Natural crystal	n + p p	E_d = 0·14, E_h = 0·14 ev $E_h^{(1)}$ = 0·05, $E_h^{(2)}$ = 0·12 ev	—
Brixner with Teufer	(*a*) 1962	$MoSe_2$ WSe_2 α-$MoTe_2$	Compacts Powder synth. 1100°C, I_2/Br_2 transport 700°C,	n p n	300°K, 3·4 77°K, 480 0·5 15 8·5 1350	—
	(*b*) 1963	WSe_2	sintered 600–800°C	p	300°K, 0·72 77°K, 120	—
	(*c*) 1963	WSe_2 $MoSe_2$	after cold pressing at 7 kB	p n		—
Hicks	1964	$MoSe_2$ WSe_2 α-$MoTe_2$	Compacts Reacted at 550°C, sintered at 1000°C, pressed to 92% theoret.	 n p n	100°C 600°C 0·6 0·8 20 1 25 0·1	300°K −110 +80 −85
Revolinsky and Beerntsen	(*a*) 1964	$MoSe_2$ WSe_2 α-$MoTe_2$	Compacts Powder synth. 750°C, pressed 5 kB and 300°C to ~ 85% theoret.	p p p	ρ ~ 10^3 at 300°K ~ 10 at 550°K E_a $MoSe_2$ 0·1 ev WSe_2 0·09 ev well-defined	—
	(*b*) 1966	α-$MoTe_2$	pressed 5 kB and 300°C to ~ 85% theoret.	p	E_a ~ 0·18 ev ; $\rho^{300°K}$ = 2000 Ω-cm	—
Champion	1965	$MoSe_2$ WSe_2 α-$MoTe_2$	650°C products rather loosely compacted	p p p	300°K, ρ 10^6 400 14000 Ω-cm	—
Lepetit	1965	α-$MoTe_2$	Transport crystals 720°C ; Br_2	n p by Nb doping	ρ peaks at 600°K, ~ 1 Ω-cm E_a(> 650°K) 0·50 ev. n type (T < 300°K) 0·08 ev p type (T < 100°K) 0·005 ev	Gradient break at 600°K. E_a > 600°K = 1·23 ev, others as for ρ. n type R_H (300°K) ~ 5 p type R_H (300°K) ~ 1
Kershaw *et al.*	1967	WSe_2	Transport crystal 750°C ; I_2	p	$\rho^{300°K}$ ~ 5, $\rho^{100°K}$ ~ 30 Ω-cm	—
Fivaz	1967	MoS_2 $MoSe_2$ WSe_2	Transport crystals Br_2 growth temperature MoS_2 and WSe_2 > 900°K	All n including WSe_2	$\rho^{300°K}$ ~ 10 Ω-cm ~ 1·5 ~ 1	300°K > 300°K 1000 E_a 100 0·16 to 100 0·07 ev (see figs. 51 and 53)

trigonal prism group VI dichalcogenides

Carrier concentration n cm^{-3}	Hall mobility μ_H (cm^2/v-sec)	Seebeck coefficient S (μv/°c)	Further comments
—	—	—	WS_2 powder also reported to be p type ; E_a 0·04, 0·11, 0·18 ev. Optical absorption above 1·1 ev in both compounds
—	—	—	Resistivity plot (see fig. 49). Evans and Young find weak optical absorption at 1·5 ev
10^{16} at 100°K 2×10^{17} at 300°K 5×10^{17} at 700°K (two samples with 3×10^{15} at 300°K)	$\mu^{300°K}\sim150$ varies as $T^{-1.4}$ steepening above 500°K	600, sharp rise below 180°K	Low mobility temperature exponent similar to Lepetit's on p type α-$MoTe_2$ in this temperature range
'Centre' numbers (i) 10^{19}n, 5×10^{14}p. (ii) $1{\cdot}4\times10^{16}p^{(1)}$, $1{\cdot}7\times10^{18}p^{(2)}$.	—	—	—
—	—	300°K −900 +990 −780 +700	Compacts did not achieve densities of much more than 90% theoretical (see Hicks also) Thermal conductivities : $\sim2\times10^{-2}$ w/cm-°c
300°K $5{\cdot}6\times10^{16}$ $8{\cdot}0\times10^{16}$ (see fig. 68 (*a*)) $7{\cdot}3\times10^{16}$	300°K 15 99 12	100°c 600°c −900 +190 +560 +530 −360 −100	p type WSe_2 may signify that tungsten compounds less likely to be metal-rich than are molybdenum products
—	—	300°K ~+400 +600 +400	Find disorder peak in ρ for mixed system (Mo/W)Se_2 (all p type)
—	—	300°K +450	ρ (300°K) ~10 composition $Mo_{1\cdot05}Te_2$
—	—	300°K +300 +600 +400	These resistivities are very high. Prepared in presence of excess chalcogen and at very low temperature
n ~ 10^{18}, falling in n type sample to 10^{14} at 77°K	300°K n type ~50 ⎫ below 10 p type ~35 ⎭ by 650°K n : $\propto T^{-1.5}$ (80°K)– 330°K $T^{-2.5}$ 330°K –(600°K) p : $\propto T^{-1.4}$ (250°K)– 570°K T^{-3} 570°K–(630°K)	At 300°K ~ 600 for both n and p type, falling above 600°K to small positive value at 1000°K	ρ and R_H (see fig. 55) μ_H (see fig. 56) S (see fig. 57)
—	—	—	—
500°K 300°K 80°K 10^{17} 6×10^{15} 10^{15} 10^{17} 5×10^{16} 10^{15} 10^{17} 5×10^{16} 10^{12}	μ (300°K) ~ 100 $\propto T^{-2.6}$ (or greater) > 300°K $T^{-2.5}$ > 250°K $T^{-2.4}$ > 120°K (see figs. 52 and 54)	—	This sample of WSe_2 appears almost compensated. It is the only case of n type behaviour reported for WSe_2, and is possibly due to the high growth temperature

Fig. 49

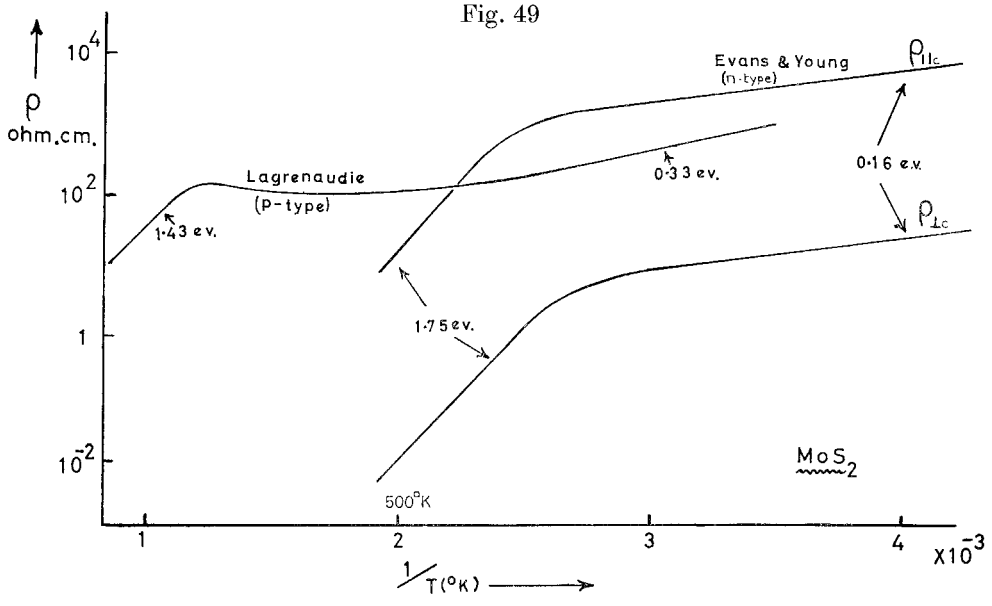

Temperature behaviour of resistivity in MoS_2 crystals.
(Lagrenaudie 1954, Evans and Young 1965.)

Fig. 50

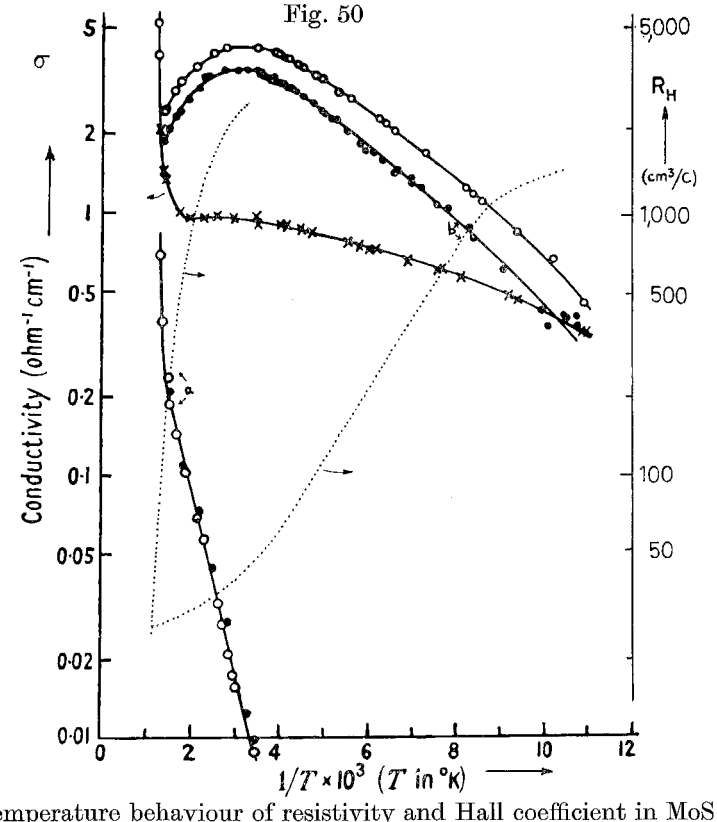

Temperature behaviour of resistivity and Hall coefficient in MoS_2 transport crystals. (p type ; Mansfield and Salaam 1953.)

Fig. 51

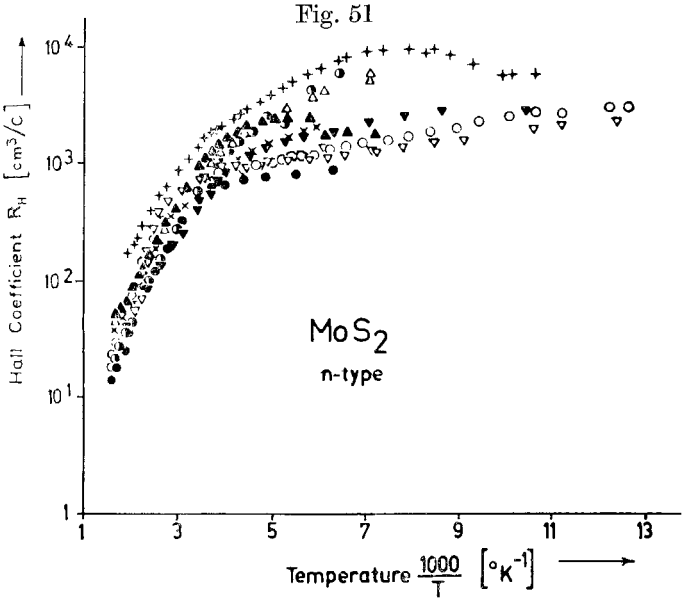

Hall coefficient for MoS_2 transport crystals. (n type ; Fivaz and Mooser 1967.)

Fig. 52

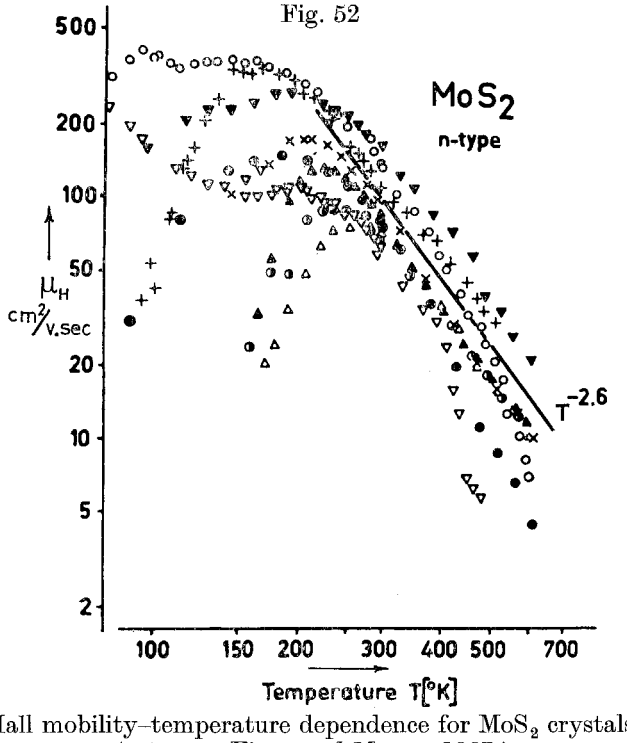

Hall mobility–temperature dependence for MoS_2 crystals.
(n type ; Fivaz and Mooser 1967.)

Fig. 53

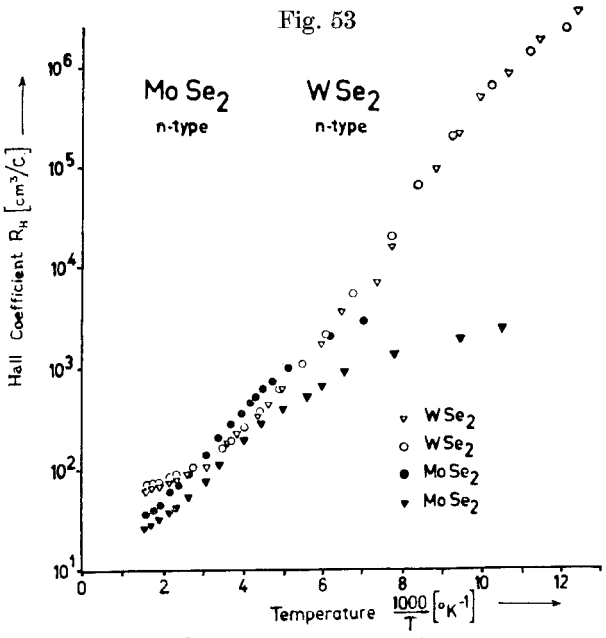

Hall coefficient results for n type $MoSe_2$ and WSe_2 transport crystals. (Fivaz and Mooser 1967.)

Fig. 54

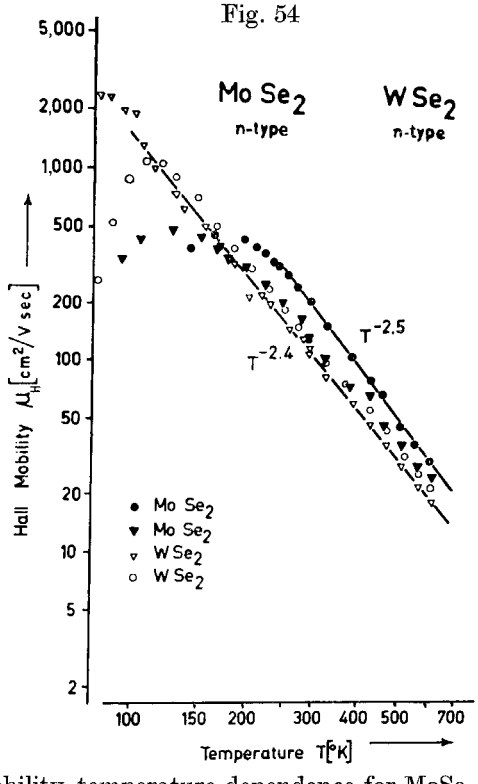

Hall mobility–temperature dependence for $MoSe_2$ and WSe_2 transport crystals. (Fivaz and Mooser 1967.)

Fig. 55

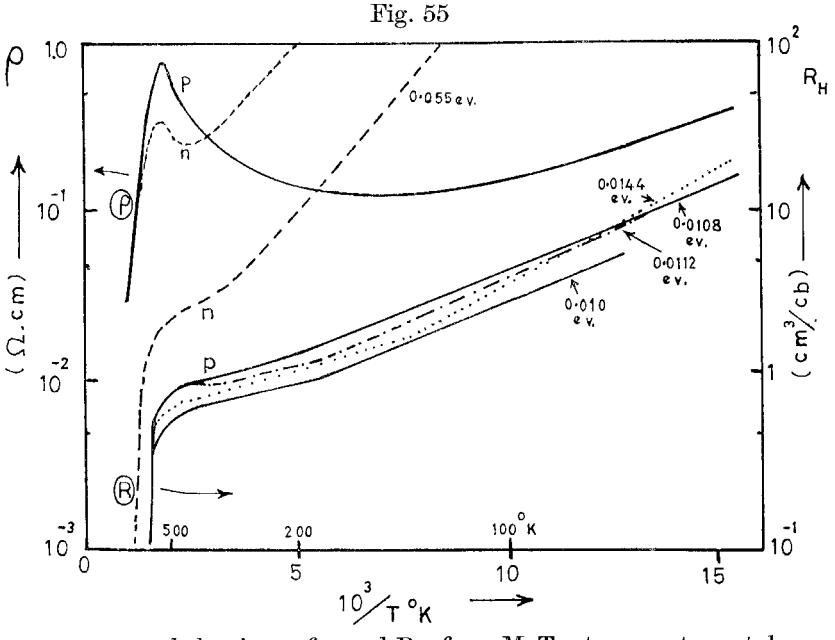

Temperature behaviour of ρ and R_H for α-$MoTe_2$ transport crystals. (p type crystals obtained by Nb doping; Lepetit 1965.)

Fig. 56

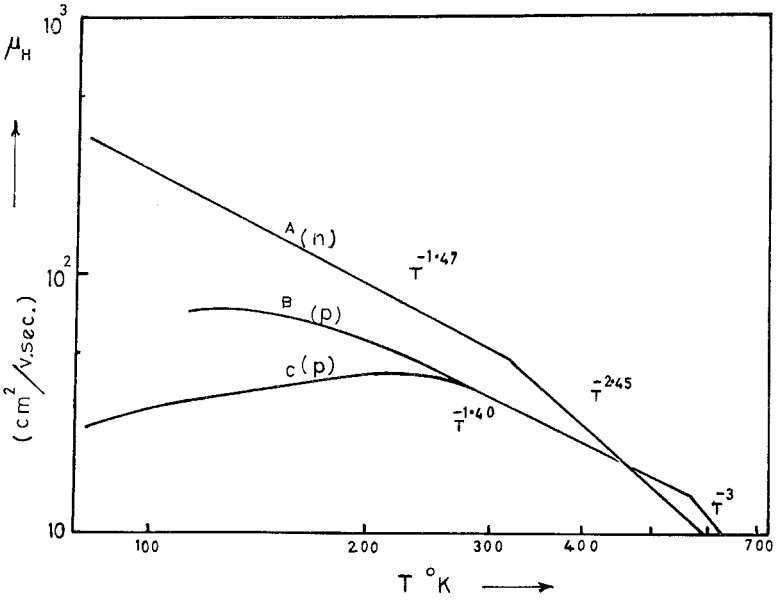

Hall mobility–temperature dependence for α-$MoTe_2$ transport crystals. (Lepetit 1965. Note differences between n and p type specimens.)

selenides and tellurides have been undertaken using sintered compacts, but here again a considerable scatter results. Crystals and compacts of both carrier types have been reported. Table 9 records some of these details.

Fig. 57

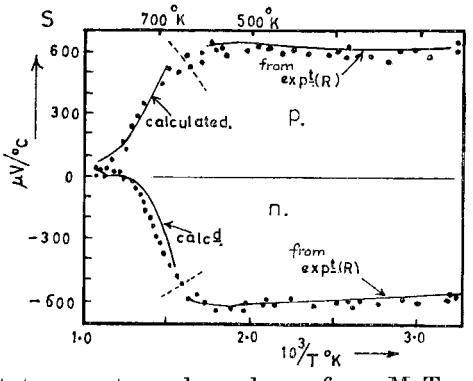

Seebeck coefficient–temperature dependence for α-$MoTe_2$ transport crystals

Three important points may be abstracted from this collection of data. (*a*) That a good case can be made for the intrinsic condition detailed above, which would match our small band gap model for the MoS_2 family. Even in crystals close to being compensated (e.g. Fivaz and Mooser's WSe_2 1967—fig. 53), the resistivity does not reach very high values at room temperature (contrast HfS_2, SnS_2 and PbI_2, $E_g \sim 2{\cdot}0$ ev). (*b*) That the hole and electron band masses associated with the d_{z^2} and d/p bands respectively are approximately equal, the room temperature mobility values ($\perp c$) being close to 100 cm^2/v-sec. Such values are compatible with band widths $\sim 0{\cdot}5$ ev (compare SnS_2, $\mu_H \approx 300$ cm^2/v-sec—Busch *et al.* 1961), and are considerably greater than for compounds like VO_2, NiS or $SrTiO_3$ ($\mu \lesssim 10$). (*c*) That the occurrence of mobility temperature exponents greater than 2 is evidence in favour of Fivaz's theory of carrier–phonon interaction in layer compounds. Fivaz (1966, 1967), Fivaz and Mooser (1964, 1967) argue that, because of the sandwich nature of the crystal, homopolar vibration of the sandwiches due to optic phonons travelling in the layers polarized $\|c$ will be strong, and that scattering of the carriers by these phonons leads to an exponent n, in the relation

$$\mu_{\perp c} \propto \left(\frac{T}{T_0}\right)^{-n},$$

which is dependent on the phonon energy, and always numerically greater than 1·5. (The *acoustic* phonon scattering exponent is deduced to be constant at unity—compare 1·5 in the three-dimensional case.) The predicted homopolar phonon energies for GaSe and MoS_2 (fig. 58) fall at similar positions within the full phonon spectrum of these compounds, but

are difficult to spot exactly as the transition is optically forbidden [GaSe 345 cm^{-1} (Leung *et al.* 1966); MoS_2 490 cm^{-1} (see fig. 39)]. The high temperature exponents obtained on α-$MoTe_2$ by Lepetit (1965) would, however, suggest a phonon energy there greater than for MoS_2. Preliminary infra-red measurements do not support this unlikely eventuality†, and as both Lepetit, and Hicks (1964), point out (see also Champness and Kipling (1965), working on Bi_2Te_3, where the exponent can rise to almost 4), these high exponents can arise when $\mu_e \approx \mu_h$. This does not seem too unlikely for the MoS_2 family, as the following room temperature results on heavily doped n and p type $MoSe_2$ suggest:

From Hicks (1964)	R_H (cm^3/cb)	n (cm^{-3})	ρ (Ω-cm)	μ (cm^2/v-sec)	Free carriers/ substitute atom
$Mo_{0\cdot99}Ta_{0\cdot01}Se_2$	$+0\cdot11$	6×10^{19}	$2\cdot5\times10^{-2}$	4	0·4
$Mo_{0\cdot98}Re_{0\cdot02}Se_2$	$-0\cdot14$	$4\cdot5\times10^{19}$	$4\cdot3\times10^{-2}$	4	0·15
$MoSe_2$	-100	6×10^{16}	5	50	—

At temperatures where 'standard' samples of the group VI materials have moved into the intrinsic region (with respect to the d band gap) we will have for the *mixed* carrier situation:

$$\sigma = n_1 e\mu_1 + n_2 e\mu_2 \quad \text{and} \quad R_H = \frac{3\pi}{8e}\left(\frac{n_h\mu_h^2 - n_e\mu_e^2}{(n_h\mu_h + n_e\mu_e)^2}\right)$$

and if $n_e \Rightarrow n_h$, then with $\mu_e \sim \mu_h$, $R_H \to 0$. If such a decrease in R_H when the temperature is raised were to be associated with a *single* free-carrier type via equations $\sigma = ne\mu$ and $R_H = 1/ne$, one would then interpret the carrier mobility as falling rapidly. Fivaz's interpretation of the experimental data may well be faulted over this point. Further details of Lepetit's conclusions concerning the electrical data are given in table 9, and of Hick's work on p. 281.

As mentioned, R_H for α-$MoTe_2$ has been observed to fall very rapidly with increasing temperature above 400°C (Lepetit 1965). This fall is also accompanied by one in resistivity, but the gradient energies do not agree (see fig. 55). The resistivity gradient gives *ca.* 1·0 ev—fairly close to the expected position of the $\sigma \to$ d/p absorption edge—whilst the gradient for R_H gives $\sim 2\cdot5$ ev. A similar finding was made by Mansfield and Salaam (1953) on p type MoS_2. Lagrenaudie (1954) and Evans and Young (1965) have also reached a region of rapid fall-off in ρ for MoS_2 (fig. 49). The

† Abdullaev *et al.* (1967) report also the same mobility temperature coefficient for InS, InSe and GaSe (Moscow Conf., p. 1237 (1968)).

latters' resistivity gradient of 1·75 ev is again close to the extrapolated position of the edge A, for a working temperature of 200°C. It is not clear by what mechanism excitations of this energy from the σ band should take apparent preference over those from the d_{z^2} band in the processes of thermal excitation, though internal radiation and re-absorption may play a part (cf. thermal conductivity in GaSe above 150°C—Guseinov and Rasulov 1966). The materials certainly have very low absorption coefficients at energies up to the direct edge.

Fig. 58

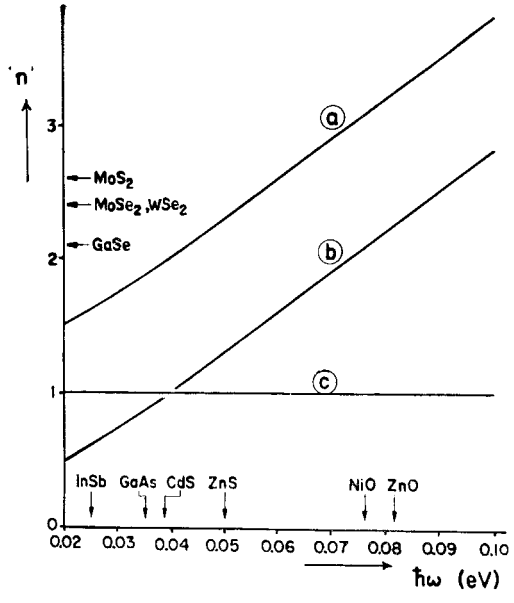

Plots of the mobility temperature exponent to be expected as a function of phonon frequency for various scattering modes according to Fivaz's theory. (Fivaz and Mooser 1967.) The exponent n in $\mu=\mu_0(T/T_0)^{-n}$, where $T_0=300$°K, for interaction with (*a*) homopolar optical modes; (*b*) polar optical modes; (*c*) acoustic optical modes.

7.2.2. *Electromagnetic work on the A and B excitons*

A photoconductive response has been obtained from this region of the spectrum (Wieting 1968) which closely matches the optical absorption results (see fig. 59). However, in several specimens the photoconduction peaks are observed in positions slightly shifted towards the blue, and additional small features are observed on the sides of the peaks, some of which were field dependent. The quantum yield was fairly independent of light intensity, but decreased with decreasing temperature. However, sizeable signals were still obtained at 30°K. Conduction band lifetimes were relatively long at 10^{-2} sec.

Fig. 59

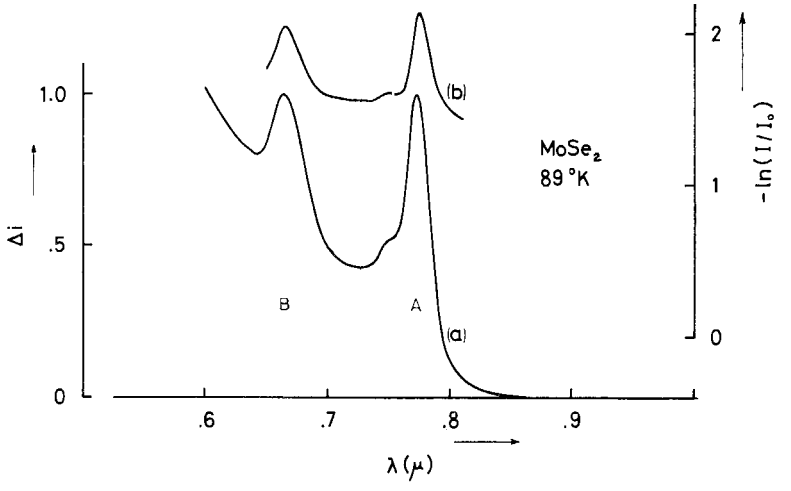

Photoconduction in $MoSe_2$. (Wieting 1968.) (*a*) Photoconductive response, (*b*) optical absorption in same specimen.

Some magneto-optical work on the MoS_2 excitons has been undertaken which leads to interesting exciton and band mass data, complementing that from zero-field measurements. Harper and Hilder (1968) have shown that in anisotropic crystals the exciton Ryberg constant is given by:

$$R_e = f(\gamma) \cdot \frac{\mu}{m_0 \epsilon^2} \cdot R_{\mathrm{Hyd}},$$

where

$$\frac{1}{\mu} = \frac{1}{3\mu_\perp} \cdot \left(2 + \frac{\epsilon_\perp \mu_\perp}{\epsilon_\parallel \mu_\parallel}\right), \quad \text{with} \quad \frac{1}{\mu_{\perp\parallel}} = \left(\frac{1}{m_e} + \frac{1}{m_h}\right)_{\perp\parallel},$$

$$\epsilon^2 = \epsilon_\perp \epsilon_\parallel,$$

and the scaling parameter

$$\gamma = 3\left(\frac{1-q}{2+q}\right), \quad \text{with} \quad q = \frac{\epsilon_\perp \mu_\perp}{\epsilon_\parallel \mu_\parallel}.$$

The function $f(\gamma)$ is dependent on the quantum numbers of the bound excitonic state in question. γ ranges from zero to 1·5 (for $q = 0$ in the case of extreme anisotropy) and in MoS_2 is found to be $\sim 0{\cdot}8$. Harper and Hilder show that for such a value of $\gamma f(\gamma) \approx 1$ for the exciton S states. This allows the simple hydrogenic-like formula to be used to evaluate μ (for MoS_2, $\epsilon_\perp = 6{\cdot}76$, $\epsilon_\parallel = 2{\cdot}74$, Evans and Young 1965). It should be noted here that γ is kept below 1, by the partial compensation in q of the ratios $\epsilon_\perp/\epsilon_\parallel$ and $\mu_\perp/\mu_\parallel$. The value of μ obtained for the A exciton is $0{\cdot}06 m_0$.

Diamagnetic shift measurements on the excitons (Evans and Young 1968) allow a value of $\mu_{\parallel}{}^{A}$ to be assessed, giving the exciton mass anisotropy as

$$\mu_{\perp}{}^{A}=0{\cdot}065\,m_0,\quad \mu_{\parallel}{}^{A}=0{\cdot}46\,m_0\quad\text{and}\quad \frac{\mu_{\parallel}}{\mu_{\perp}}\approx 7.$$

Magneto-oscillation measurements carried out on the 2 ev exciton in GaSe (see Halpern 1966, Aoyagi *et al* 1966) at helium temperatures yielded there the values:

$$\mu_{\perp}=0{\cdot}14\,m_0,\quad \mu_{\parallel}=0{\cdot}7\,m_0\quad\text{and}\quad \frac{\mu_{\parallel}}{\mu_{\perp}}\approx 5.$$

If the mobility ratio deduced by Fivaz and Mooser (1967) $\perp c$ in n and p type GaSe is valid at 5 to 1, then $(m_e/m_h)_{\perp}=1/\sqrt{5}$, and one obtains there

$$m_e{}^{\perp}=0{\cdot}2m_0,\quad m_h{}^{\perp}=0{\cdot}44m_0.$$

This value of $m_h{}^{\perp}$ means that the limit deduced by Fivaz (1967) for self-trapping of the exciton is closely approached.

7.3. *The Regular Group V and Mixed V/VI Materials*

7.3.1. *Group V materials as antiferromagnetic metals*

The layer compounds of group V divide into four classes. The ditellurides have distorted octahedral coordination. These and the unusual octahedral 1T forms of TaS_2 and $TaSe_2$ are considered separately in § 8. The remaining two classes are undistorted layer structures having octahedral (VSe_2), or trigonal prism coordination (NbS_2, $NbSe_2$, TaS_2, $TaSe_2$—2H, 3R or 4Ha polytypes—see fig. 3). The band models given above indicate that the materials in each of these latter two classes are d band metals. VSe_2 seems a somewhat better metal than the trigonal prism materials, where the single free-carrier half fills the narrow d_{z^2} band. The room temperature resistivity of VSe_2 is $\sim 10^{-4}\,\Omega$-cm, whilst that of $NbSe_2$, etc. is $\sim 4\times 10^{-4}\,\Omega$-cm. The free-carrier absorption for VSe_2 goes right through into the visible range (cf. the metallic oxide ReO_3—Feinleib *et al.* (1968)), whilst that for the NbS_2 family dies away in the near I.R. around $10\,000\,cm^{-1}$. In NbS_2, etc., since the plasma limit occurs at an energy less than that of the direct absorption edge (cf. CoS_2 fig. 84) an exact location of ω_p can be made. A calculation of the effective mass from the simple expression† $\omega_p=(4\pi ne^2/m^*)^{1/2}$ yields $m^*=2{\cdot}6m_e$. The high effective mass here is in sympathy with the fact that NbS_2, etc., are superconductors whilst VSe_2 (and ReO_2) are not (see p. 309).

† It has recently been confirmed by Hall coefficient measurements that $NbSe_2$ has indeed one free electron per formula unit (Lee *et al.* 1969). The sign of the Hall coefficient is positive, whilst that of the Seebeck coefficient is negative (see table 18.)